Faculté des Sciences
Département de Géographie
Laboratoire de Climatologie et Topoclimatologie

High resolution present and future climate and surface mass balance of Svalbard modelled by the regional climate model MAR

A thesis submitted in partial fulfilment
of the requirements for the academic degree of

Doctor of Philosophy in Sciences
at the University of Liège (Doctoral college of Geography)
by

Charlotte LANG

Academic year 2015–2016

Jury members:

Louis François	President	Professor, University of Liège
Michel Erpicum	Promoter	Professor, University of Liège
Xavier Fettweis	Co-promoter	Research Associate FRS-FNRS, University of Liège
Cécile Agosta		Postdoctoral Researcher, University of Liège
Willem Jan van de Berg		Assistant Professor, University of Utrecht
Johannes Fürst		Postdoctoral Researcher, University of Erlangen-Nürnberg
Hubert Gallée		Senior Researcher CNRS, University of Grenoble

Abstract

We modelled the climate and surface mass balance (SMB) of Svalbard with the regional climate model MAR.

First, we simulated the climate and SMB at a spatial resolution of 10 km over the ERA-Interim era (1979–2013), that we used to force the boundaries of our integration domain. Despite the presence of a cold bias, MAR is in agreement with SMB measurements. The SMB integrated over the permanent ice area is negative on average ($-1.6\,\mathrm{Gt\,yr^{-1}}$) with a large interannual variability (7.1 Gt) but no acceleration of the melt has been simulated over the last 35 years, unlike over the Greenland ice sheet where melt has broken several records since 2005. This stability of SMB, in agreement with observations, is due to a recent change in summer atmospheric circulation bringing north-westerly flows in summer over Svalbard, contrasting the recent observed Arctic warming. However, in 2013, the atmospheric circulation changed to a south–southwesterly flow over Svalbard causing record melt, SMB ($-20.4\,\mathrm{Gt\,yr^{-1}}$) and summer temperature.

We also evaluated the global model MIROC5 and MAR forced by this model over the period 1980–2005, in order to do a future projection. MIROC5 is significantly colder than ERA-Interim but the near-surface biases are reduced in MAR forced by MIROC5 and the SMB difference with MAR forced by ERA-Interim is not significant. MIROC5 is however not able to simulate the recent change in atmospheric circulation and induces in MAR forced by MIROC5 a significant trend of decreasing SMB ($-0.6\,\mathrm{Gt\,yr^{-2}}$) over 1980–2005.

We then performed a future projection and forced MAR with MIROC5 until 2100, following the RCP8.5 scenario. MAR predicts a similar evolution of increasing surface melt everywhere in Svalbard followed by a sudden acceleration of the melt around 2050–2060, with a larger melt increase in the south compared to the north of the archipelago. This melt acceleration around 2050 is mainly driven by the albedo-melt feedback associated with the expansion of the ablation/bare ice

zone. This effect is dampened in part as the solar radiation itself is projected to decrease due to cloudiness increase. The near-surface temperature is projected to increase more in winter than in summer, as the temperature is already close to 0 °C in summer. The model also projects a stronger winter west-to-east temperature gradient, related to the large decrease of sea ice cover around Svalbard. By 2085, SMB is projected to become negative over all of Svalbard's glaciated regions, leading to rapid degradation of the firn layer.

Finally, we implemented in MAR a subroutine allowing the surface module SISVAT to run at a resolution twice as high as the atmospheric module. We ran 2 simulations: the first at a spatial resolution of 7.5 km and the second with the atmospheric module running at 7.5 km and SISVAT at 3.75 km. We also extended the simulation period and covered the ERA-40 (1960–1978) as well as ERA-interim (1979–2014) eras. First, at 7.5 km, the cold bias present at 10 km is strongly reduced, due to a better representation of the topography. On Spitsbergen, where the topography is very hilly, the agreement between SMB measurements and MAR outputs is better at 7.5 km than at 10 km and our subroutine correcting SMB improves the results furthermore. A resolution of 3.75 km is however still not enough to represent the very complex SMB pattern on Spitsbergen. On the Austfonna ice cap, a resolution of 7.5 km is enough, given the much gentle slopes and the 3.75 km simulation does not improve the results. Over the period 1960–2014, the surface mass balance simulated by MAR at 3.75 km decreases significantly. However, given the very close values of the trend and its uncertainty range and the large interannual variability of SMB, the significance of the trend is debatable. Over the ERA-40 period, cloudiness increases significantly, causing a significant increase in precipitation, itself causing a significant SMB increase ($+0.63 \pm 0.59\,\mathrm{Gt\,yr^{-2}}$). Finally, in 2014, the summer atmospheric circulation was again a north-westerly flow and, as a result, the amount of runoff was close to the average value and SMB did not break any record ($-3.1\,\mathrm{Gt\,yr^{-1}}$).

Résumé

Nous avons modélisé le climat et le bilan de masse en surface (SMB) du Svalbard à l'aide du modèle climatique régional MAR.

Dans un premier temps, nous avons réalisé des simulations à une résolution spatiale de 10 km sur la période couverte par la réanalyse ERA-Interim (1979–2013), utilisée pour forcer les bornes du domaine. MAR présente un biais froid mais montre néanmoins un accord avec des mesures de bilan de masse en surface. Le SMB intégré sur toutes les régions englacées est négatif ($-1.6\,\mathrm{Gt\,an^{-1}}$) et sa variabilité interannuelle est grande (7.1 Gt) mais aucune accélération de la fonte n'a été modélisée sur les 35 dernières années, au contraire du Groenland qui a connu plusieurs records de fonte estivale depuis 2005. Cette stabilité du bilan de masse en surface, en accord avec les observations, est due à un changement de circulation atmosphérique en été amenant des masses d'air froides du nord-ouest sur le Svalbard et contrecarrant le réchauffement climatique observé dans l'Arctique. En 2013, la circulation atmosphérique estivale était un flux de sud-sud-ouest et ne pouvait plus s'opposer au réchauffement, causant un record de fonte, de SMB ($-20.4\,\mathrm{Gt\,an^{-1}}$) et de température estivale au Svalbard.

Nous avons également évalué le modèle global MIROC5 et MAR forcé par celui-ci sur la période 1980–2005, dans le but de réaliser une projection future. MIROC5 est significativement plus froid qu'ERA-Interim mais les différences en surface sont réduites lorsque MAR est forcé par MIROC5, de sorte que le SMB n'est pas significativement différent lorsque MAR est forcé par MIROC5 ou ERA. MIROC5 ne simule cependant pas le récent changement de circulation atmosphérique et MAR forcé par MIROC5 simule un SMB qui décroît de manière significative ($-0.6\,\mathrm{Gt\,an^{-2}}$) sur la période 1980–2005.

Nous avons ensuite réalisé une projection future en forçant MAR avec MIROC5 et le scénario RCP8.5 jusqu'en 2100. Durant la première moitié du 21ème siècle, MAR prévoit la même évolution d'augmentation de la fonte partout

sur le Svalbard, suivie d'une augmentation soudaine plus forte de la fonte vers 2050–2060, avec une plus forte augmentation dans le sud de l'archipel que dans le nord. Cette augmentation de la fonte est liée à la rétroaction fonte-albédo de surface associée à l'expansion de la zone d'ablation. L'effet de l'albédo sur la fonte est en partie compensé par la diminution du rayonnement solaire atteignant la surface et résultant d'une augmentation de l'épaisseur optique des nuages. MAR prévoit une plus forte augmentation de la température en hiver qu'en été, étant donné que la température est déjà proche de 0 °C en été, ainsi qu'un plus large gradient spatial dans l'augmentation de la température hivernale lié à la disparition de la glace de mer. MAR prévoit également que, selon le scénario RCP8.5, d'ici 2085, la totalité de la zone d'accumulation aura disparu.

Enfin, nous avons implémenté dans MAR une sous-routine permettant au module de surface SISVAT de tourner à une résolution 2 fois plus élevée que le module atmosphérique. Nous avons réalisé une simulation à 7.5 km de résolution spatiale et une autre dans laquelle le module atmosphérique tournait à une résolution de 7.5 km et SISVAT à une résolution de 3.75 km. Nous avons également étendu la période de nos simulations et forcé MAR avec les réanalyses ERA-40 (1960 –1978) et ERA-Interim (1979–2014). Tout d'abord, à 7.5 km, le biais froid est fortement réduit, grâce à une meilleure représentation de la topographie. Sur Spitzberg, où la topographie est très marquée, l'accord entre des mesures de SMB et le SMB modélisé par MAR est meilleur à 7.5 km qu'à 10 km et notre sous-routine corrigeant le SMB améliore encore les résultats de MAR. Une résolution de 3.75 km n'est cependant pas encore assez haute pour représenter la complexité spatiale du SMB sur Spitzberg. Sur la calotte Austfonna, comme les pentes sont plus douces, une résolution de 7.5 km est suffisante et la simulation à 3.75 km n'améliore pas les résultats. Sur la période 1960–2014, le bilan de masse en surface simulé par MAR à 3.75 km de résolution décroît de manière significative. Cependant, vu les valeurs proches de la tendance et de son intervalle d'incertitude et la grande variabilité interannuelle du SMB, la significativité de la tendance est discutable. Sur la période ERA-40, la couverture nuageuse augmente de manière significative, entraînant une augmentation significative des précipitations, elle-même causant une augmentation significative du SMB ($+0.63 \pm 0.59\,\mathrm{Gt\,an^{-2}}$). Finalement, en 2014, la circulation atmosphérique estivale venait de nouveau du nord-ouest et la fonte avait une valeur proche de la moyenne. Aucun record de SMB n'a donc été battu en 2014 ($-3.1\,\mathrm{Gt\,an^{-1}}$).

Remerciements

Tout d'abord, je souhaite adresser mes plus vifs remerciements à mes promoteurs, le Professeur Michel Erpicum et le Dr. Xavier Fettweis, pour leur encadrement sans faille et leurs précieux conseils tout au long de ma thèse et de mes études.

Ensuite, je remercie le Professeur Louis François, qui m'a donné l'envie d'étudier la climatologie, d'avoir accepté de présider ce jury.

I also wish to thank Cécile Agosta, Willem Jan van de Berg, Johannes Fürst and Hubert Gallée for accepting to be in this jury.

Merci également à tous mes collègues du Département de Géographie; à ceux du Laboratoire de Climatologie, M. Erpicum, Xavier, Sébastien, Alexandre, Julien et les deux autres "C de climato", Cécile et Coraline; ainsi qu'à Laura et Arnaud pour avoir joué les Maman-Gâteau et Papa-Poule ces derniers jours.

Finalement, je tiens à remercier ma bande, Kalinka, Papa, Maman, Marie et Pierre et tous ceux qui ont contribué à faire de ces quatre dernières années une formidable aventure. En attendant la prochaine ...

List of Figures

List of Tables

List of abbreviations

a	albedo
ASR	Arctic System Reanalysis
AV	Austfonna and Vestfonna
BE	Barentsøya and Edgeøya
CC	Cloud cover
COD	Cloud optical depth
DJF	December – January – February
GCM	General circulation model
JJA	June – July – August
LHF	Latent heat flux
LWD	Downward long-wave radiation
LWU	Upward long-wave radiation
LWnet	Net long-wave radiation
MAE	Mean absolute error
MAR	Modèle atmosphérique régional
$\mathbf{MAR_{ERA}}$	MAR forced by ERA-Interim
$\mathbf{MAR_{MIROC5}}$	MAR forced by MIROC5 (present)
$\mathbf{MAR_{RCP8.5}}$	MAR forced by MIROC5 with RCP8.5 scenario (future)
$\mathbf{MAR_{3.75km}}$	MAR forced by ERA-Interim at 3.75 km
$\mathbf{MAR_{7.5km}}$	MAR forced by ERA-Interim at 7.5 km
$\mathbf{MAR_{10km}}$	MAR forced by ERA-Interim at 10km
	= $\mathrm{MAR_{ERA}}$ in Chapter 4
MB	Mass balance
ME	Mean error
MIROC5	Model for interdisciplinary research on climate
NET	NET energy at the surface
NPI	Norsk Polarinstituut

PDD	Positive degree day
RCM	Regional climate model
RMSE	Root mean square error
RMSEc	Centred RMSE
SISVAT	Soil ice snow vegetation atmosphere transfer
SHF	Sensible heat flux
SIC	Sea-ice cover
SLR	Sea level rise
SMB	Surface mass balance
SST	Sea surface temperature
SU (SU/EV)	Sublimation and evaporation
SWalb	Net shortwave radiation computed with constant SWD and varying albedo
SWD	Downward shortwave radiation at the surface
SWswd	Net shortwave radiation computed with constant albedo and varying SWD
SWnet	Net shortwave radiation
TAS	Near-surface temperature
$\mathbf{TAS_{JJA}}$	Summer near-surface temperature
T850	Temperature at the 850hPa level
$\mathbf{T850_{JJA}}$	Summer temperature at the 850hPa level
Z700	Geopotential height at the 700hPa level
$\mathbf{Z700_{JJA}}$	Summer geopotential height at the 700hPa level

Contents

CHAPTER 1

General introduction

1.1 Svalbard

Svalbard is a Norwegian archipelago located between 74 and 81 ° lat N and 10 and 35 ° lon E, halfway between the North Pole and mainland Norway (Fig. 1.1). It is bordered by the Arctic Ocean to the North, the Greenland Sea to the West, the Norwegian Sea to the South and the Barents Sea to the East. The archipelago, which has a total area of 62 248 km^2 (Liestøl, 1993), is covered by more than 2000 glaciers and ice caps on 59 % of its surface. The main islands are Spitsbergen, Nordaustlandet, Edgeøya and Barentsøya (Fig. 1.1a).

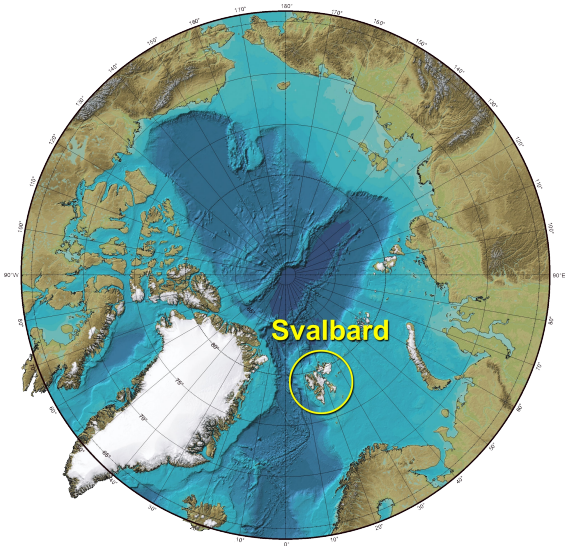

Figure 1.1: Localisation of Svalbard. Source: http://geology.com/world/arctic-ocean-bathymetry-map.shtml

The name Svalbard is first mentioned in 1194 in the Sagas of Icelanders, which tell the story of the discovery by Norwegian Vikings of a land they literally called "cold shores". The first irrefutable discovery happened June 10th 1596 when the Dutch navigator Willem Barentsz, searching for the Northeast passage, discovered Bear Island (Bjørnøya), the Southernmost island of the archipelago. On June 17th, the crew reached a new part of the archipelago that Barentsz named Spitsbergen, "pointed mountains", referring to the numerous tops he could see. In 1920, the Treaty relating to Spitsbergen gave Norway sovereignty and delimited the boundaries of the archipelago. It took effect through the Act of 17 July 1925 relating to Svalbard, which changed the name Spitsbergen into Svalbard and set the first Governor of Svalbard.

Svalbard's climate is polar-type but is by far warmer than other regions at the same latitude, thanks to the North Atlantic Drift, a branch of the Gulfstream

bringing oceanic heat to the west coast of the archipelago. Precipitation is quite low on the west coast of Svalbard (often less than 400 mm) but can be twice as low further inland (Liestøl, 1993). The highest amount of precipitation (more than 1000 mm, Liestøl, 1993) is found in the eastern and southern parts of the archipelago because of frequent depressions in the Barents Sea bringing humid air on the east coast of Svalbard (Winther et al., 1998; Hisdal, 1976). The weather conditions are very variable in time as Svalbard's weather is alternately influenced by dry and cold polar air masses coming from the north and more humid and warm air masses from the south. Snow can fall at any time in summer and temperatures can be positive even during the winter.

Spitsbergen is the most alpine of the Svalbard islands, with a very marked topography going up to 1717 m on Newtontoppen (Fig. 1.2b). As a result, a lot of small cirque and valley glaciers are found on Spitsbergen, especially in the west (Fig. 1.2a). Large ice masses divided into streams by mountain ridges are also found (Hagen et al., 2003b). The largest one of those ice fields is Olav V Land, located on the northeastern side of Spitsbergen, with an area of about 3000 km^2 (Liestøl, 1993).

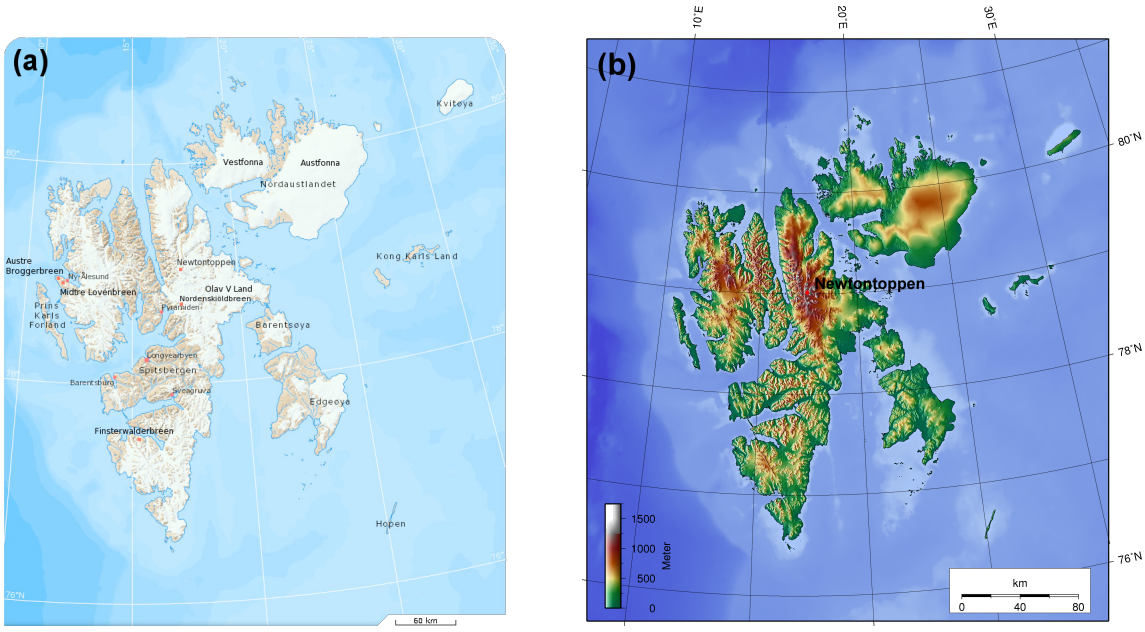

Figure 1.2: **(a)** Svalbard glaciers and ice caps and main settlements. Source: http://toposvalbard.npolar.no/ **(b)** Svalbard topography. Source: https://commons.wikimedia.org/wiki/File:Svalbard-topo.png

Nordaustlandet, Edgeøya and Barentsøya, on the other hand, have a quite smooth topography with gentle slopes and ice caps rather than small glaciers therefore prevail. The largest two ice caps are Austfonna (8105 km^2) and Vestfonna (2510 km^2)

(Dowdeswell, 1986) and are located respectively on the eastern and western parts of Nordaustlandet. Austfonna has an ice thickness ranging from less than 100 m on the southeastern coast to 500 m at Austdomen, the top of the island (791 m), while Vestfonna peaks at 630 m.

Most of Svalbard glaciers are polythermal glaciers, i.e. glaciers that share both the characteristics of temperate and cold glaciers. In most cases, the temperature of the glacier is close to the melting point in the accumulation area whereas the part of the glacier in the ablation area is frozen to the bed (Liestøl, 1993). However, some very small glaciers (area smaller than 10 km^2) can be considered as polar or cold as their entire mass is far below 0 °C (Hagen et al., 2003b). As a result of their low temperatures, Svalbard glaciers velocities are inferior to 10 $m\,yr^{-1}$ (Hagen et al., 2003a) and lower than those of temperate glaciers. Indeed, because of their basal temperature, a thin film of water forms at the base of temperate glaciers. This layer acts as a lubricant and helps the glaciers sliding on the bedrock. Cold glaciers, for their part, are frozen to their bed and their velocities are thus lower. Surging type glaciers are also very common in Svalbard. A surge is a cyclic sudden acceleration of the ice flow, 10 to 1000 times faster than usual, caused by increased water storage at the bed resulting in rapid basal motion. Svalbard glaciers surges are particular for two reasons. First of all, the proportion of surging glaciers in Svalbard is huge compared to the world average. Based on glacier registration, Lefauconnier and Hagen (1991) claim that up to 90 % of Svalbard glaciers are of the surging type whereas less than 1 % of the world's glaciers are (Jiskoot et al., 2000). Secondly, the surge mechanism is of a different type in Svalbard. For temperate glaciers, the switch is hydrological: the increased water storage is caused by the transition from a system of conduits with efficient drainage and low storage to a system of linked cavities with inefficient drainage (Kamb et al., 1985). For polythermal glaciers, such as those found in Svalbard, the switch is thermal: the ice build-up causes the ice pressure to increase until the cold ice at the bed reaches the melting point and produces meltwater at the bed that is kept from escaping by the cold tongue of the glacier (Fowler et al., 2001; Murray et al., 2003). As a result, during surge episodes, the flow of Svalbard glaciers is much slower than for other glaciers and a single episode also lasts longer (Murray et al., 2003).

1.2 Surface mass balance

1.2.1 Definition

The mass balance (MB) of (part of) a glacier, ice cap or ice sheet is the water balance expressing, over a given period of time, the difference between the mass that is gained (snowfall, deposition, etc) and the mass that is lost (surface melt, iceberg discharge, sublimation, etc). Surface mass balance (SMB) is the water balance that takes into account surface processes only and leaves out basal melting and dynamical processes. The area of the glacier with mass gain is called the accumulation zone whereas the area with surface mass loss is the ablation zone. The boundary between the ablation and accumulation zone, where the surface mass balance is equal to zero, is called the equilibrium line. The SMB and its components (precipitation contributing to accumulation and meltwater runoff and evaporation and sublimation contributing to ablation) can be calculated by a regional climate model coupled with a snow model as the one used in this study (see Sect. 1.4). The erosion/deposition of the snow by the wind will not be taken into account in our study. Dynamical processes such as iceberg calving, however, require coupling the climate model with an ice sheet model and will not be addressed in this work.

Nevertheless, studying surface mass balance only rather than mass balance has its advantages. Indeed, surface mass balance is also called climatic mass balance, due to the fact that its components are driven by climate: precipitation and melt due to positive temperature mainly. As a result, the response of SMB to a climate perturbation is immediate whereas the dynamic of a glacier has a certain response time. Moreover, two different glaciers can have a very different response to a climate perturbation (due to their different size, shape, nature of the bed, etc) whereas the SMB will mostly react the same way to the same perturbation.

1.2.2 Surface mass balance in Svalbard

Surface mass balance measurements were first carried out in 1950 when the Norsk Polarinstitutt started to measure winter accumulation and summer ablation every other year on Finsterwalderbreen (Fig. 1.2a), a small glacier in the South of Spitsbergen. In 1966 and 1967, observations started at Austre Brøggerbreen and Midtre Lovénbreen, two glaciers a few kilometres away from

Ny-Ålesund weather station. Since then, the Svalbard (surface) mass balance has been intensively studied. On a local scale (i.e. on one or a few glaciers), various types of mass balance reconstructions using different tools have been performed: Lefauconnier and Hagen (1990) used correlations between the measured SMB and climatic parameters measured at Ny-Ålesund weather station (northwestern coast of Spitsbergen), Rasmussen and Kohler (2007) used a model running with meteorological data from NCEP/NCAR reanalysis, de Woul and Hock (2005) used a Positive Degree-Day (PDD) model and temperature and precipitation data from Ny-Ålesund. Energy balance models have also been used: van Pelt et al. (2012) used an energy balance model coupled to a snow model forced by the regional climate model (RCM) RACMO on Nordenskiöldbreen and Rye et al. (2010, 2012) used a coupled surface–subsurface energy balance model forced by the ERA-40 reanalysis to reconstruct the SMB of Midtre Lovénbreen. On a larger scale, Schuler et al. (2007) have modelled the surface mass balance of the Austfonna ice cap with a model based on weather data and SMB measurements. Førland et al. (2011) used the 25 km outputs of the NorACIA-RCM (Førland et al., 2009) to statistically downscale temperature and precipitation at the location of several weather stations and Benestad et al. (2002) empirically downscaled temperature using principal component analysis. Day et al. (2012) compared precipitation from the HadRM3 RCM (25 km) to the SMB measurements from Pinglot et al. (1999) and performed future projections of the Svalbard climate. Finally, Bamber et al. (2004, 2005) estimated elevation changes of glaciers and ice caps between 1996 and 2002 using airborne lasers and, more recently, Moholdt et al. (2010) computed elevation changes from 2003 to 2008 based on measurements made by the ICESat satellite. Measurements made on individual glaciers show that their SMB has been stable from the 1960s to the late 1990s (Hagen et al. (2003b) and references therein). Some glaciers later experienced increased melting that stabilised in the second half of the 2000s (Nuth et al., 2012). Moholdt et al. (2010) also showed that the SMB of Svalbard was very negative in 2003 – 2004 but more balanced between 2004 and 2007, indicating a stability of the SMB in Svalbard, that is opposite to what has recently been observed in Greenland, where several melt records have been broken since 2005 (Fettweis et al., 2013b). Future projections of the Svalbard climate have been made by Førland et al. (2011), Day et al. (2012) have studied the impact of the future sea ice decline on the temperature, precipitation and SMB of Svalbard while Radić and Hock (2011), Marzeion et al. (2012) and Radić et al. (2014) have evaluated the contribution of Svalbard glaciers to future sea level rise.

1.3 Motivation

Worldwide, glaciers and ice caps are observed to retreat and, in this context, it is important to evaluate the impact of climate change on high latitude zones, as they are known to be very sensitive to a rise in temperature (IPCC AR5, 2013). Over 1961–2004, the Arctic has been the second largest contribution (excluding the Antarctic and Greenland ice sheets) to sea level rise (Kaser et al., 2006). According to Gardner et al. (2013) and Shepherd et al. (2012), between 2003 and 2009, glaciers and ice caps (including peripheral glaciers in Greenland and Antarctica) have contributed to sea level rise as much as the Greenland and Antarctic ice sheets, contributing together to 61 % of the total sea level rise. Arctic ice loss represents almost 50 % of the total glacier and ice caps loss but Svalbard contributed to only 4 % of the total Arctic contribution (Gardner et al., 2013). Svalbard seems to be the ice cap least sensitive to the recent Arctic warming in summer (Serreze et al., 2009) and while melt records have been broken several times in Greenland in the second half of the 2000s (Fettweis et al., 2013b), the surface mass balance of Svalbard has been closer to balance after 2004 (Moholdt et al., 2010). Fettweis et al. (2013b) attributed it to atmospheric circulation changes in summer damping the Arctic warming over Svalbard. The Svalbard (surface) mass balance has already been intensively studied but previously published studies mostly involved either long time series but on only a few glaciers or over extended areas but on shorter time scales. Moreover, for logistic reasons, the long SMB time series are often available for small glaciers near the coast, whose SMB is not representative of inner regions of Svalbard. The recent stabilisation of the Svalbard SMB, in full opposition to the other Arctic ice caps, therefore needs to be seen from a larger perspective, that can be provided by the outputs of a model able to run over the entirety of Svalbard, at a high resolution and over longer periods of time.

In the next decades, contrary to what was previously estimated (Meier et al., 2007; Meehl et al., 2007), glaciers and ice caps as found over Svalbard are no longer believed to be the dominant contributors to sea level rise, as the melt of the Antarctic and Greenland ice sheets has been accelerating (Rignot et al., 2011, 2014). Yet, the vanishing of Svalbard glaciers in the future could have huge impacts on the fauna and flora, permafrost (Isaksen et al., 2007; Etzelmüller et al., 2011), tourism and even possibly the development of agriculture. Moreover, surface mass balance is the component of mass balance most sensitive to climate

change but the future evolution of the glaciers of Svalbard themselves have been little studied and most studies focussed on past and present surface mass balance, showing the need for climate and surface mass balance future projections over Svalbard, which can only be achieved with modelling tools.

Regional climate models (RCM) fully coupled with energy balance models are ideal tools for the study of surface mass balance over recent decades as well as for future projections. General circulation models (GCM, also called global climate models) are among the most complex numerical models, as their governing equations are physically based, but they cover the entire Earth and are therefore time consuming and require coarse resolutions. Regional climate models, on the other hand, are also physically based but run over limited areas, allowing much higher spatial resolution simulations. The topography is therefore better represented in RCMs and more local effects can be modelled. Moreover, the physics of RCMs can be calibrated for a particular region whereas GCMs are mostly tuned to produce the best results under our latitudes and neglect polar regions. However, RCMs boundaries need to be forced, either by global models or reanalysis, and their outputs depend on the model used to force them. In addition, they explicitly solve the energy and mass balance of glaciated regions, allowing to simulate the surface albedo positive feedback, which is not possible with forced energy balance models. Empirical energy balance models are also rarely forced by outputs from high resolution atmospheric models but rather by global ones. RCMs such as the regional MAR model, developed specifically for the study of polar climates at the University of Liège and LGGE (Laboratoire de Glaciologie et Géophysique de l'Environement), therefore give us the opportunity to perform more reliable future projections. Indeed, as we will see in Chapter 3, the surface albedo-melt feedback is projected to be a very important factor in the future evolution of the SMB of Svalbard. Finally, this study is the first one to use such a regional model over Svalbard as, until now, SMB calculations in Svalbard were often based on statistical or empirical surface models.

1.4 MAR

MAR (Modèle Atmosphérique Régional) is a regional atmospheric climate model specifically developed for the study of polar regions (Gallée and Schayes, 1994) and consists of an atmospheric model coupled with the surface model SISVAT (Soil Ice Snow Vegetation Atmosphere Transfer) (de Ridder and Gallée,

1998; Gallée et al., 2001) through the exchange of energy fluxes, momentum, precipitation, etc. The SISVAT model is a vertical 1-D multi-layered model consisting of a soil/vegetation module and a snow/ice energy balance module resolving most of the processes occurring at the surface of the snow/ice pack and is based on the CROCUS model (Brun, 1989) from the CEN (Centre d'Études de la Neige). The soil/vegetation module simulates the exchanges of heat and moisture with the atmosphere above the land without snow or ice while the snow/ice module deals with the exchanges between the atmosphere and the sea ice, the glaciers and ice sheets and the snow covering the land. Snow layers are characterised by their temperature, density, height, age, liquid water content, dendricity and sphericity of the crystals and grain size. These snow properties evolve with time in the snow metamorphism module according to Brun (1989). The energy balance between the soil and the snow is computed in the thermodynamic module through the absorbed shortwave flux, the longwave fluxes (upward and downward), the sensible and latent heat fluxes at the surface, the melting and sublimation of snow/ice and evaporation and refreezing of the meltwater heat fluxes, the heat fluxes due to precipitation (solid and liquid), condensation and deposition and the heat flux from the ground. MAR has been extensively evaluated over Greenland and is able to accurately simulate the SMB of the Greenland ice sheet (e.g. Fettweis et al. (2013a) and Franco et al. (2013) and references therein). The model is not coupled with a 3-D ice sheet model, which prevents us from modelling dynamical processes and constrains us to use a fixed topography and ice extent throughout the entire simulation and force us to focus only on the surface mass balance. The MAR version used here is 3.5 and the configuration is the one used in Fettweis et al. (2013a). Finally, the blowing snow module parametrising the snow erosion by the wind is switched off, as a lot of uncertainties still remain in the development of this module that has been validated only over Antarctica. (Gallée et al., 2013).

1.5 Structure of the thesis

Chapter 2 of this thesis deals with the present (1979 – 2013) climate and SMB, insisting on the recent stabilisation of the SMB. In Chapter 3, we present our future projection (1980 – 2100) of the Svalbard climate and surface mass balance. Finally, in Chapter 4, we present an online downscaling tool developed to allow the SISVAT module to run at a resolution twice as high as the atmospheric

module without highly time consuming runs and compare the results to a “classic” MAR simulation.

CHAPTER 2

Present climate and surface mass balance of Svalbard

This chapter focuses on the present climate and surface mass balance of Svalbard modelled at a spatial resolution of 10 km by MAR forced by ERA-interim over the period 1979–2013. After discussing the possible SMB biases caused by the use of a 10 km resolution topography (Sect. 2.2), we evaluate MAR by comparing its results to near-surface measurements from weather stations and SMB measurements (Sect. 2.3). We discuss its results over the current climate in Sect. 2.4. In Sect. 2.5, we compare ERA-Interim with MIROC5 over Svalbard as well as MAR forced by both of those in Sect. 2.6, with the aim of performing a future projection in Chapter 3.

The content of this chapter has been published in *The Cryosphere*, 9, 83–101, 2015 (Lang et al., 2015a).

2.1 Model forcings

We have run MAR over the period 1979–2013 at a spatial resolution of 10 km. The lateral and oceanic boundaries were forced every 6 h (temperature, wind and humidity at each vertical level as well as sea surface temperature and sea-ice cover over the ocean) by the ERA-Interim (MAR_{ERA}) reanalysis (0.75 ° resolution) and the MIROC5 (MAR_{MIROC5}) general circulation model (1.4 ° resolution). The reanalysis and the GCM fields were also used to initialise the simulations at the beginning (1 September 1974). Five years of spin-up are required to reduce the impact of the snowpack initialisation (in particular the snow density) on our results.

2.2 Errors in the 10 km interpolated topography

The fractional permanent ice mask and topography used in MAR over Svalbard (Fig. 2.1b and d) have been interpolated at 10 km from the glacier inventory of Nuth et al. (2013) (Fig. 2.1a) and from the topography from the Norsk Polarinstitutt (NPI) respectively (Fig. 2.1c). Both shapefile data sets had previously been interpolated on a 250 m grid to produce files that can be read by MAR. The total area (Kvitøya excluded) of the ice mask is 33 264 km^2, which

is about 55 % of the total land surface. With the 10 km interpolated ice mask, the total permanent ice area is 30 042 km^2 and corresponds to 49 % of the 10 km interpolated land surface.

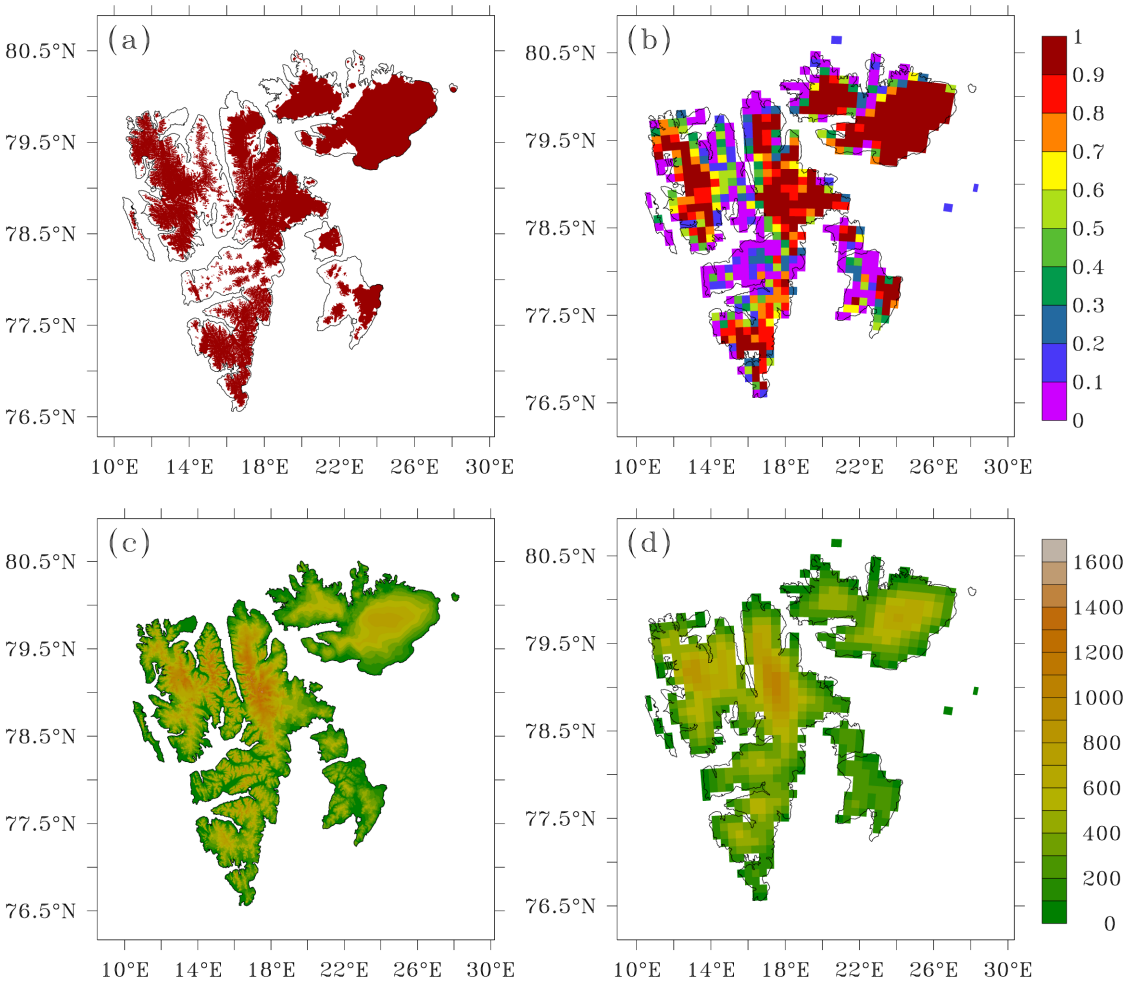

Figure 2.1: **(a)** Permanent ice mask from Nuth et al. (2013) interpolated on a 250 m grid. **(b)** Permanent 10 km fractional ice mask as used in MAR. **(c)** Svalbard topography (m a.s.l.) from the Norsk Polarinstitutt interpolated on a 250 m grid. **(d)** 10 km topography as used in MAR (m a.s.l.).

In version 3 of MAR, the ice mask is fractional, i.e. each pixel is associated with a proportion of its area that is covered with permanent ice (Fig. 2.1b). In our analysis, the ice sheet area corresponds to the pixels covered with at least 50 % of permanent ice. If not, we consider these pixels to be the tundra zone. In all calculations showing integrated values over the entire ice sheet, we have computed weighted averages according to the percentage of ice covering each ice pixel (i.e. having a permanent ice area higher than 50 %)

Figure 2.2 shows that using a resolution of 10 km underestimates the elevation, especially on both sides of Wijdefjorden (northern Spitsbergen) where the

difference is greater than 500 m due to a very steep topography.

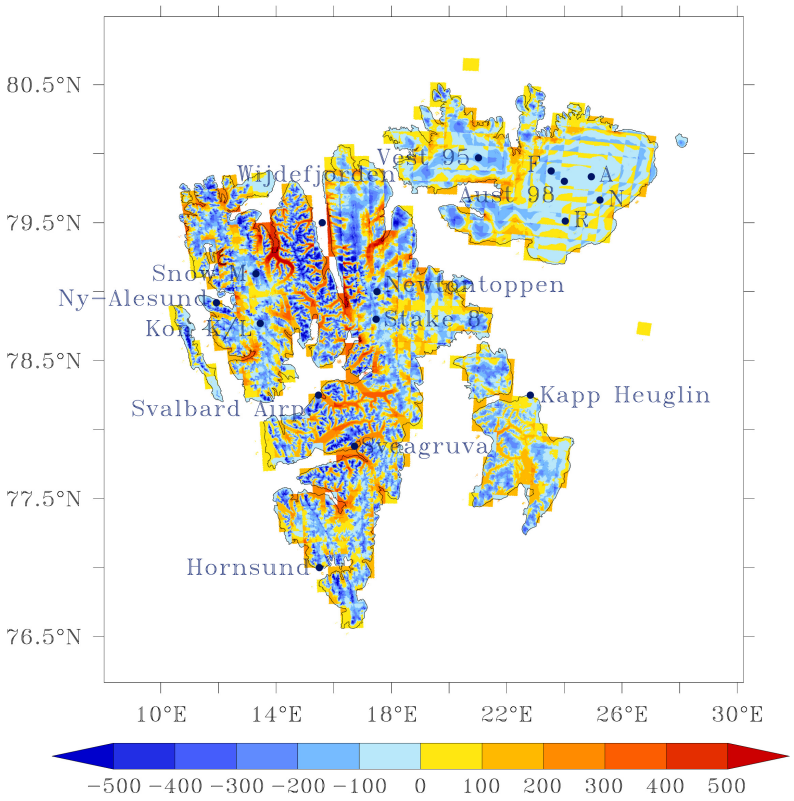

Figure 2.2: Elevation difference (m) between the 10 km MAR topography (based on the topography of the Norsk Polarinstitutt – NPI) and the topography of the NPI interpolated on a 250 m grid. The black X show the location of the weather stations used in the validation and the red ones show the location of the stakes from Pinglot et al. (1999, 2001).

We have divided the elevation range into 16 classes (Table 2.1) and computed the mean elevation error between the interpolated 10 km elevation (as used in MAR) and the 250 m topography, as well as the mean absolute error. The mean error gives an indication of whether a certain elevation range is underestimated (negative value) or overestimated (positive value) in the MAR topography, and the absolute error gives the mean value of the elevation bias, regardless of its sign. Due to the smoothing of the topography at a resolution of 10 km, the topography used in our MAR simulations underestimates all the elevations above 1000 m (classes 11 to 16) whereas for classes 3 to 10 (200–1000 m), the elevation is mostly underestimated but there are also areas where it is overestimated in the MAR topography. Finally, close to the coastline, where the elevation is lower than 200 m, the MAR topography slightly overestimates the elevation for most of the pixels.

As a consequence of the elevation underestimation at a resolution of 10 km, a lot of glaciers are too low in altitude in MAR than in reality, which could impact

Table 2.1: Elevation classes. ME = mean error, MAE = mean absolute error. The last two columns give the percentage of the area that over- and underestimates the elevation in the 10-km topography (used in MAR) for each elevation class.

Class	Alt range (m)	ME	MAE	% overestimated	% underestimated
1	]0,100]	96.4	115.0	69	31
2	]100,200]	42.5	104.0	60	40
3	]200,300]	-9.2	99.4	45	55
4	]300,400]	-62.4	115.2	31	69
5	]400,500]	-96.3	128.9	22	78
6	]500,600]	-116.9	139.6	17	83
7	]600,700]	-129.4	150.8	16	84
8	]700,800]	-163.9	182.7	11	89
9	]800,900]	-205.0	220.0	11	89
10	]900,1000]	-216.3	223.5	8	92
11	]1000,1100]	-257.8	258.2	2	98
12	]1100,1200]	-318.7	318.7	0	100
13	]1200,1300]	-377.9	377.9	0	100
14	]1300,1400]	-404.4	404.4	0	100
15	]1400,1500]	-478.9	478.9	0	100
16	>1500	-585.8	585.8	0	100

their simulated surface mass balance as shown by Lenaerts et al. (2013), who found that the bias increases when the SMB is increasingly negative.

In extreme cases, some glaciers at a resolution of 10 km could be at such low elevations that they should not even exist under the present climate in the 10 km grid. As a result, the accumulation zone is missing and the melt is overestimated and could introduce a bias when considering the integrated surface mass balance of Svalbard. However, the interannual variability of the surface mass balance should not significantly be affected by the smoothing of the topography at a resolution of 10 km. Based on the histogram (Fig. 2.3), corrections of the SMB integrated over the entirety of Svalbard will be given in Section 2.4. Finally, as we consider only the pixels covered with more than 50 % of ice to be ice pixels, a lot of small glaciers (corresponding to 10 % of the permanent ice area) are left out of our analysis.

2.3 Evaluation of MAR forced by ERA-Interim

In order to evaluate our model over the present climate, we have compared the MAR results (called $\mathrm{MAR_{ERA}}$ hereafter) forced by ERA-Interim from ECMWF

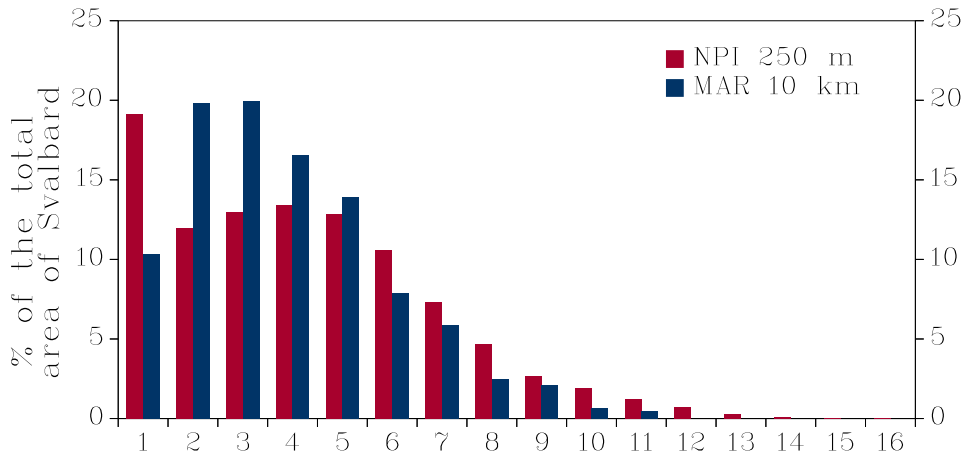

Figure 2.3: Histogram of the area of the 16 elevation classes defined in Table 2.1 in percentage of the total area of Svalbard for the Norsk Polarinstitutt topography interpolated on a 250 m grid and the 10 km-topography as used in MAR.

(Dee et al., 2011) over 1979–2013 to near-surface measurements of temperature and precipitation from weather stations as well as surface mass balance measurements. For comparison, these weather measurements have also been compared to the ASR (Wilson et al., 2011) and the ERA-Interim reanalysis, knowing that no observation is assimilated into the MAR model.

2.3.1 Comparison of MAR with weather stations

First, we have compared the daily near-surface temperature (TAS) of the stations listed in Table 2.2 and shown in Fig. 2.2 to the daily MAR_{ERA} TAS (corresponding to the 2–3 m level) of the pixel that is the closest to each station. As 1979 is the first year of ERA-Interim reanalysis, the comparison has been made over 1979–2013 when data were available.

Table 2.2: Stations used for validation. Period over which data are available, coordinates and elevation of the stations (m), elevation of the corresponding model pixel used in the validation (m) and distance between the station and the pixel (km).

Station	Period observation		Coordinates		Elev	Pixel elev (m)			Dist station-pixel (km)		
	Temperature	Precipitation			(m)	MAR	ERA	ASR	MAR	ERA	ASR
Hornsund	2005–2013	1996–2013	77.00° N	15.50° E	10	178	22	227	6.0	57.0	36.8
Kapp Heuglin	2006–2013	–	78.25° N	22.82° E	14	54	87	166	6.7	28.7	21.9
Ny-Ålesund	1979–2013	1979–2013	78.92° N	11.93° E	8	137	215	361	3.3	64.5	52.3
Svalbard Lufthavn	1979–2013	1979–2013	78.25° N	14.47° E	28	188	214	242	4.2	30.3	13.4
Sveagruva	1979–2013	1979–2002	77.88° N	16.72° E	9	284	234	247	1.1	54.1	57.9

While MAR is too cold compared to the observations, the daily variability of the temperature is very well simulated by MAR (Table 2.3). Part of these

biases are however caused by the overestimation of the stations' elevation in MAR induced by the used 10 km resolution and the very steep topography near the coast. However, given the values of both temperature and elevation biases, MAR is anyway too cold even if no elevation bias was present as the temperature vertical gradient is $1\,°C\,100\,m^{-1}$ at its maximum. As summer temperature has more impact on the surface mass balance (through the melt) than the annual mean temperature, we have separately evaluated the JJA (June, July and August) temperatures. In summer, the MAR cold bias is smaller than the annual bias at Hornsund and Kapp Heuglin and comparable at Svalbard Lufthavn and Sveagruva and the RMSE is smaller at every station except Ny-Ålesund. The daily observed variability is however less well reproduced by MAR in summer.

Table 2.3: 1979–2013 mean annual and summer correlation (R^2), RMSE and bias (°C) between MAR_{ERA} and the observed daily temperature and percentage of missing observations (% MO).

Station	Annual				Summer			
	R^2	RMSE (°C)	Bias (°C)	% MO	R^2	RMSE (°C)	Bias (°C)	% MO
Hornsund	0.94	3.79	−3.25	21	0.48	2.81	−2.45	21
Kapp Heuglin	0.93	3.66	−2.48	32	0.78	1.35	−0.68	38
Ny-Ålesund	0.94	2.49	−1.31	3	0.74	2.60	−2.27	1
Svalbard Lufthavn	0.93	3.66	−2.77	1	0.72	3.30	−2.91	0
Sveagruva	0.92	4.92	−4.00	3	0.65	4.39	−4.08	5

The main effect of this MAR cold bias on the modelled SMB is a likely underestimation of the amount of melt in summer. Colder air can also contain less moisture and therefore a cold bias should imply an underestimation of snowfall. However, it is the temperature in altitude that influences the moisture content rather than TAS, and a negative TAS bias does not necessarily mean that the free atmosphere temperature bias will also be cold. It is therefore difficult to interpret the TAS cold bias in terms of snowfall underestimation. Moreover, the weather stations used in the validation are all located at the coast and most of them in fjords. As the resolution of ERA-Interim is too low to represent these fjords, we interpolated the ERA-Interim sea-ice cover (SIC) and sea surface temperature (SST) on the 10 km grid, then extrapolated SIC and SST in the fjords using the values of the nearest pixels. But this extrapolated SIC/SST may not be representative of the SIC/SST of the fjords and therefore could cause a temperature bias that would not be present further inland, as the ocean conditions influences the coastal regions a lot. However, we have no observations far inland and in the free atmosphere to confirm this.

It is well known that the outputs of regional climate models are strongly

dependent on the reanalysis or global model used to force their boundaries. However, as the MAR and ERA-Interim reanalysis biases (Table 2.4) are different and of opposite signs for some of the stations (MAR is too cold while ERA-Interim is too warm), this shows well that MAR is totally free in the boundary layer and that the MAR cold bias does not come from the lateral boundaries. Moreover, in Ny-Ålesund, the MAR bias averaged over 2000–2010 (Table 2.5) is smaller than the ASR bias (Table 2.6), both on the annual timescale and during summer. This suggests that MAR compares well with other model outputs using data assimilation. On the annual timescale, MAR is better than ASR at reproducing the daily variability of the temperature for every station and comparable to ERA whereas in summer, the three products are comparable.

Table 2.4: 1979–2013 mean annual and summer correlation (R^2), RMSE and bias (°C) between the ERA-Interim reanalysis and the observed temperature.

Station	Annual			Summer		
	R^2	RMSE (°C)	Bias (°C)	R^2	RMSE (°C)	Bias (°C)
Hornsund	0.94	3.01	2.24	0.57	1.31	0.63
Kapp Heuglin	0.95	2.18	1.14	0.66	1.54	0.55
Ny-Ålesund	0.93	3.03	−1.95	0.78	2.33	−2.00
Svalbard Lufthavn	0.96	2.31	−1.40	0.79	2.12	−1.66
Sveagruva	0.93	2.75	−1.07	0.72	2.40	−1.98

Table 2.5: 2000–2010 mean annual and JJA correlation (R^2), RMSE and bias (°C) between the MAR_{ERA} and observed daily temperature.

Station	Annual			Summer		
	R^2	RMSE (°C)	Bias (°C)	R^2	RMSE (°C)	Bias (°C)
Horsund	0.94	4.03	-3.49	0.45	2.92	-2.57
Kapp Heuglin	0.92	4.19	-3.07	0.57	1.58	-0.80
Ny-Ålesund	0.95	2.65	-1.99	0.70	2.95	-2.61
Svalbard Lufthavn	0.94	4.08	-3.51	0.71	3.81	-3.51
Sveagruva	0.92	4.89	-4.08	0.64	4.40	-4.10

MAR underestimates the annual mean amount of precipitation at Ny-Ålesund and overestimates it at the other three stations (Table 2.7). It is obvious that we can not resolve the complex spatial variability of precipitation along the coast at a resolution of 10 km but it is also difficult to gauge the snowfall amount in this windy region. Moreover, a lot of data are missing for all the stations. Therefore, we can not draw any conclusion about a likely overestimation of the MAR precipitation by using only precipitation measurements from coastal weather stations.

Table 2.6: 2000–2010 mean annual and JJA correlation (R^2), RMSE and bias (°C) between the ASR reanalysis and the observed daily temperature.

Station	Annual			Summer		
	R^2	RMSE (°C)	Bias (°C)	R^2	RMSE (°C)	Bias (°C)
Horsund	0.89	2.43	-1.40	0.63	1.90	-1.63
Kapp Heuglin	0.85	3.33	-0.63	0.43	1.89	0.65
Ny-Ålesund	0.88	3.86	-2.82	0.74	4.04	-3.84
Svalbard Lufthavn	0.92	2.74	-1.20	0.79	1.77	-1.29
Sveagruva	0.87	3.45	-0.70	0.64	2.24	-1.54

Table 2.7: 1979–2013 mean annual measured precipitation ($mm\,yr^{-1}$), proportion of that precipitation that is simulated by MAR_{ERA} and percentage of missing observations (% MO).

Station	Pobs ($mm\,yr^{-1}$)	Pmod/Pobs	% MO
Hornsund	378	1.16	50
Kapp Heuglin	–	–	100
Ny-Ålesund	409	0.77	47
Svalbard Lufthavn	187	1.52	39
Sveagruva	252	1.52	42

2.3.2 Comparison of MAR with SMB measurements

As validation of the SMB, we have compared MAR to SMB measurements from Pinglot et al. (1999) and Pinglot et al. (2001), as indicated in Tables 2.8 and 2.9 and Fig. 2.2.

The MAR model underestimates the SMB for 5 of the 10 sites and overestimates it for the remaining 5 (Table 2.9) so there is no systematic bias. The mean error is $-0.20\,m\,w.e.\,yr^{-1}$, corresponding to $-2\,\%$, and the absolute error is $0.10\,m\,w.e.\,yr^{-1}$ (i.e. $25\,\%$), but none of the differences are significant with respect to the MAR interannual variability (the difference is significant at the 95 % confidence level if it is higher than twice the interannual variability of the MAR SMB).

On the Austfonna and Vestfonna ice caps, where the slopes are gentle and a resolution of 10 km is enough to represent the main variations of the topography, the SMB is generally well modelled, except for stake N where the difference is a bit larger ($0.14\,m\,w.e.\,yr^{-1}$, corresponding to a difference of $+70\,\%$). On Spitsbergen, on the contrary, the topography is so steep that a 10 km resolution is not enough to represent it and elevation biases are huge. The precipitation pattern is more complex than on the ice caps because of the "barrier effect" induced by the

Table 2.8: Sites of Pinglot et al. (1999, 2001) used in the comparison.

Stake	Coordinates		Elevation stake (m)	Elevation MAR (m)	Distance pixel-stake (km)	Period
Stake 8	78°48′ N	17°28′ E	1173	895	3.66	1986–1996
Kon K	78°47′ N	13°17′ E	639	586	4.77	1986–1988
Kon L	78°46′ N	13°27′ E	726	586	4.63	1986–1991
Snow M	79°08′ N	13°18′ E	1170	849	4.62	1986–1991
Vest 95	79°58′ N	21°01′ E	600	478	4.78	1986–1994
F	79°52′ N	23°32′ E	727	651	3.09	1986–1999
Aust 98	79°48′ N	24°00′ E	740	710	2.26	1986–1997
A	79°50′ N	24°56′ E	729	623	3.72	1986–1998
N	79°40′ N	25°14′ E	491	518	3.76	1986–1999
R	79°31′ N	24°02′ E	511	469	1.82	1986–1999

Table 2.9: Annual measured SMB ($\mathrm{m\,w.e.\,yr^{-1}}$) from Pinglot et al. (1999, 2001) and simulated by $\mathrm{MAR_{ERA}}$, SMB difference (% and $\mathrm{m\,w.e.\,yr^{-1}}$) between the MAR outputs and the measurements, MAR interannual variability of the SMB ($\mathrm{m\,w.e.\,yr^{-1}}$). MAE = Mean absolute error.

Stake	Mean annual SMB ($\mathrm{m\,w.e.\,yr^{-1}}$)		SMB difference (%)	SMB difference ($\mathrm{m\,w.e.\,yr^{-1}}$)	MAR interannual variability ($\mathrm{m\,w.e.\,yr^{-1}}$)
	Pinglot	MAR			
Stake 8	0.75	0.74	−1.3	−0.01	0.18
Kon K	0.48	0.28	−41.7	−0.20	0.28
Kon L	0.62	0.31	−50.0	−0.31	0.19
Snow M	0.57	0.67	17.5	0.10	0.18
Vest 95	0.41	0.30	−26.8	−0.11	0.18
F	0.37	0.37	0.0	0.00	0.26
Aust 98	0.52	0.46	−11.5	−0.06	0.17
A	0.42	0.43	2.4	0.01	0.24
N	0.20	0.34	70.0	0.14	0.26
R	0.23	0.29	26.1	0.06	0.27
MAE			24.7	0.10	

topography and, therefore, as a result of the elevation underestimation discussed in the previous section, there could be local precipitation biases influencing the modelled surface mass balance. For example, between Kongsvegen (Kon K and Kon L) and the ocean lies an area where the elevation is highly underestimated. At Ny-Ålesund weather station, located in that area, the modelled precipitation is underestimated by 25 %. In our topography, the "barrier effect" of the elevated

topography is not present and orographic precipitation may occur in another region. As a consequence, the SMB modelled at Kongsvegen is underestimated quite a lot (-0.2 and $-0.31\,\mathrm{m\,w.e.\,yr^{-1}}$, corresponding to -42 and $-50\,\%$). Using the WRF model (Weather Research and Forecasting), Claremar et al. (2012) investigated the effect of model resolution on wind speed in Svalbard, which strongly depends on the topography as does precipitation. They also conclude that, over very hilly topography, wind speed biases are large and a very high resolution is needed. From this comparison, we can conclude that MAR simulates well the surface mass balance but a resolution of 10 km is likely too coarse to model correctly the SMB and its components over Spitsbergen, where the topography is more complex.

Day et al. (2012) have compared some of the measurements from Pinglot et al. (1999) to the precipitation from the HadRM3 RCM (as the ice cores of Pinglot et al. (1999) were retrieved in the accumulation zone). Their biases are similar for the Aust 98 stake, but we have better results at Vest 95 ($-0.11\,\mathrm{m\,w.e.\,yr^{-1}}$ vs. -0.24). However, Day et al. (2012) results do not show a huge bias on Kongsvegen like ours do.

Finally, we can compare the $\mathrm{MAR_{ERA}}$ mean elevation change rate (dh/dt in $\mathrm{m\,yr^{-1}}$) over 2003–2008 to Moholdt et al. (2010) (Fig. 2.4, to be compared to Fig. 1 of Moholdt et al. (2010)). In northwestern Spitsbergen, $\mathrm{MAR_{ERA}}$ simulates

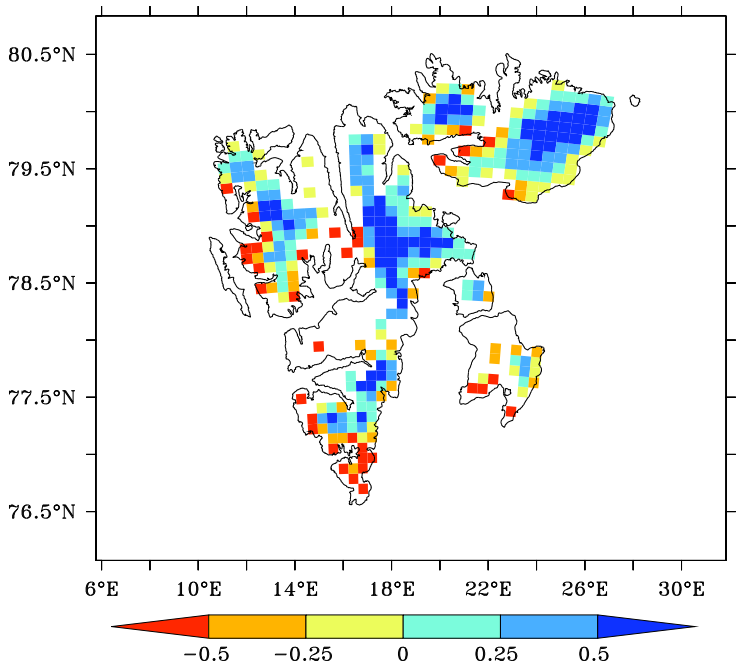

Figure 2.4: 2003–2008 $\mathrm{MAR_{ERA}}$ mean elevation changes ($dh/dt, \mathrm{m\,yr^{-1}}$).

a thickening of the interior whereas the entirety of northwestern Spitsbergen is thinning in Moholdt et al. (2010) and in south Spitsbergen, $\mathrm{MAR_{ERA}}$ barely simulates the thickening on the east coast. As a result, the regionaly averaged thinning of northwestern Spitsbergen is underestimated and the averaged thinning of south Spitsbergen is overestimated (Table 2.10).

Table 2.10: 2003–2008 mean elevation changes ($dh/dt, \mathrm{m\,yr^{-1}}$) from $\mathrm{MAR_{ERA}}$ and Moholdt et al. (2010) for different regions.

Region	dh/dt ($\mathrm{m\,yr^{-1}}$)	
	$\mathrm{MAR_{ERA}}$	Moholdt et al. (2010)
Austfonna	0.00	0.11 ± 0.04
Vestfonna	-0.14	-0.16 ± 0.08
Northwest Spitsbergen	-0.22	-0.54 ± 0.10
Northeast Spitsbergen	0.02	0.06 ± 0.06
South Spitsbergen	-0.45	-0.15 ± 0.16
Barentsøya/Edgeøya	-0.38	-0.17 ± 0.11
Total	-0.13	-0.12 ± 0.04

On Austfonna and in northeastern Spitsbergen, on the other hand, the pattern of the mean elevation change rate compares well with Moholdt et al. (2010). $\mathrm{MAR_{ERA}}$ represents well the thickening of the interior of Austfonna and northeastern Spitsbergen but slightly overestimates the margins thinning in northeastern Spitsbergen and slightly overestimates it on Austfonna. Regionally averaged, dh/dt of northeastern Spitsbergen and Austfonna also compares well with Moholdt et al. (2010). Integrated over Svalbard, the $\mathrm{MAR_{ERA}}$ mean elevation change is the same as Moholdt et al. (2010) ($-0.13\,\mathrm{m\,yr^{-1}}$ vs. -0.12 ± 0.04). $\mathrm{MAR_{ERA}}$ therefore compares well with Moholdt et al. (2010), considering the biases associated to the 10km topography and the fact that only the first $\sim 10\,\mathrm{m}$ of ice and snow are modelled in MAR and that the compaction of the deep snow/ice layers is therefore not taken into account.

2.4 Results of MAR over the present climate

The mean annual total SMB integrated over Svalbard (Fig. 2.5a, black curve) simulated by $\mathrm{MAR_{ERA}}$ between 1979 and 2013 is $-1.6 \pm 7.1\,\mathrm{Gt\,yr^{-1}}$, corresponding to $-54 \pm 236\,\mathrm{mm\,w.e.\,yr^{-1}}$ with our ice sheet mask.

The bias resulting from the use of a 10 km topography can be corrected based on the elevation classes histogram in Fig. 2.3 and gives an estimated mean

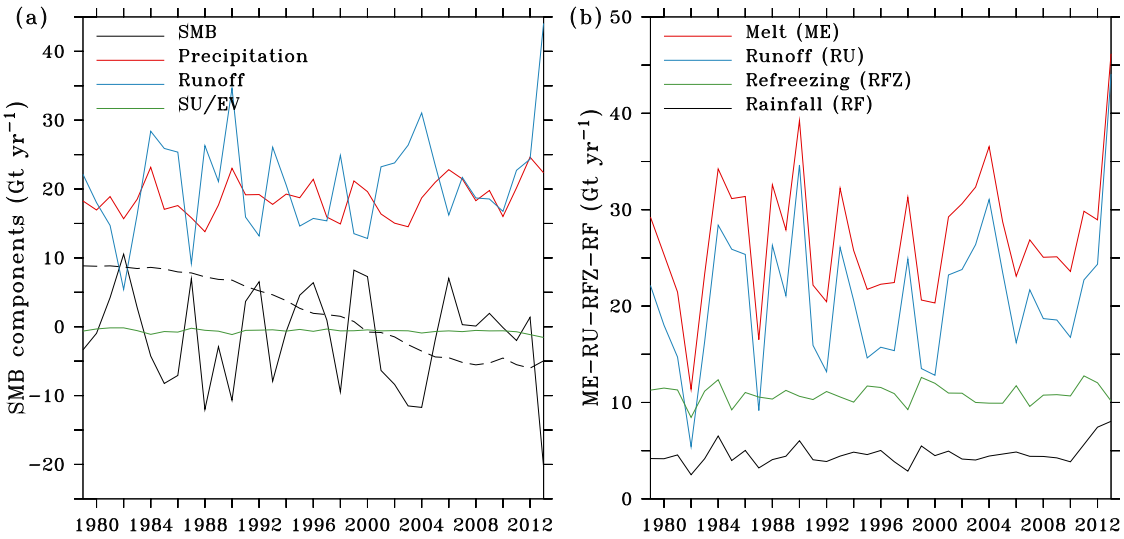

Figure 2.5: **(a)** Evolution of the $\mathrm{MAR}_{\mathrm{ERA}}$-based SMB integrated over the permanent ice mask ($\mathrm{Gt\,yr^{-1}}$) and its components: (solid plus liquid) precipitation, meltwater runoff and sublimation and evaporation (SU/EV) over 1979–2013. The dashed black curve represents the $\mathrm{MAR}_{\mathrm{MIROC5}}$-based SMB (after having applied a 10 yr running mean). **(b)** Same as **(a)** but for the liquid water (melt, runoff and liquid precipitation) and refreezing ($\mathrm{Gt\,yr^{-1}}$).

annual value of $0.4\,\mathrm{Gt\,yr^{-1}}$ (corresponding to $12\,\mathrm{mm\,w.e.\,yr^{-1}}$), fully included in the uncertainty range given here by the 1979–2013 interannual variability (standard deviation of 7.1 Gt). The high interannual variability is mainly a result of the variability of the meltwater runoff ($R^2 = 0.85$ between the SMB and runoff), itself mainly due to the interannual variability of the JJA mean TAS. Based on measurements made in the 1960s–1990s, Hagen et al. (2003b) estimated the SMB integrated over Svalbard to be $-14 \pm 3\,\mathrm{mm\,w.e.\,yr^{-1}}$ or $-0.5 \pm 0.1\,\mathrm{Gt\,yr^{-1}}$. Our mean value of $-54\,\mathrm{mm\,w.e.\,yr^{-1}}$ over 1979–2013 therefore aligns with the values of Hagen et al. (2003b), considering the large interannual variability of our SMB and the fact that the time period over which the simulations were performed are not the same (e.g. our mean value would have been $-36\,\mathrm{mm\,w.e.\,yr^{-1}}$ if we had not considered the year 2013). Calving has been estimated by Hagen et al. (2003b) to be $4.5\,\mathrm{Gt\,yr^{-1}}$ ($\sim 110\,\mathrm{mm\,w.e.\,yr^{-1}}$) and is therefore a very important component of the net mass balance compared to their estimation of SMB. However, it is small compared to the contribution of surface runoff to the total mass loss ($680\,\mathrm{mm\,w.e.\,yr^{-1}}$ in Hagen et al. (2003b) and $695\,\mathrm{mm\,w.e.\,yr^{-1}}$ simulated by $\mathrm{MAR}_{\mathrm{ERA}}$). Błaszczyk et al. (2009) estimated a calving flux of $6.75 \pm 1.75\,\mathrm{km^3\,yr^{-1}}$ over 2000–2006 from ASTER imagery and we used this value to estimate SMB values from different mass balance (MB) estimates (Table 2.11). Considering again the large interannual variability of the SMB, our $\mathrm{MAR}_{\mathrm{ERA}}$ estimates compares well with Wouters et al. (2008) and the low value of Mémin

Table 2.11: Comparison between SMB simulated by MAR ($\mathrm{mm\,w.e.\,yr^{-1}}$) and different studies. (1) The SMB estimate has been calculated as the net mass balance ($\mathrm{km^3\,yr^{-1}}$) minus the estimated calving flux from Błaszczyk et al. (2009) ($6.75\,\mathrm{km^3\,yr^{-1}}$), then converted in $\mathrm{mm\,w.e.\,yr^{-1}}$ by dividing it by the surface of the glaciated area. (2) The $\mathrm{MAR_{ERA}}$ SMB has been estimated over 1979–2013.

Reference	Time period	Mass balance ($\mathrm{km^3\,yr^{-1}}$)	SMB estimate ($\mathrm{mm\,w.e.\,yr^{-1}}$)(1)	$\mathrm{MAR_{ERA}}$ estimate ($\mathrm{mm\,w.e.\,yr^{-1}}$)
Mémin et al. (2011)	2003–2008	−9.1	−65	−98
Mémin et al. (2011)	2003–2008	−15.5	−243	−98
Mémin et al. (2011)	1998–2007	−25.0	−508	−88
Wouters et al. (2008)	2003–2007	−8.8	−49	−118
Nuth et al. (2010)	65/90–03/07(2)	−9.7	−106	−75

et al. (2011) (corresponding to the MB of $-9.1\,\mathrm{km^3\,yr^{-1}}$), both obtained from GRACE measurements. It also compares well with Nuth et al. (2010), knowing that the time period of their estimate is different from ours and different from the time period over which the calving flux was estimated. The high GRACE value of Mémin et al. (2011) (MB of $-15.5\,\mathrm{km^3\,yr^{-1}}$) and the value obtained by ground gravity observations (MB of $-25\,\mathrm{km^3\,yr^{-1}}$) give a surface loss much larger than ours but those values are also quite large compared to the other studies. To sum up, $\mathrm{MAR_{ERA}}$ compares well with studies for which the SMB has been estimated and also gives satisfying results compared to other studies for which we had to estimate the SMB contribution using a calving flux value estimated over the same period.

SMB measurements starting in the 1960s on individual glaciers show a stability of the SMB until the late 1990s (Hagen et al. (2003b) and references therein). The SMB of these glaciers located near the coast was negative, meaning that the glaciers are losing mass but without any acceleration nor deceleration of the surface mass loss. However, some glaciers like Kongsvegen and Kronebreen experienced increased melting in the late 1990s (Nuth et al., 2012) but their SMB stabilised in the second half of the 2000s. Integrated over the entirety of Svalbard, the 1979–2013 linear temporal trend of the $\mathrm{MAR_{ERA}}$ SMB ($-0.1\,\mathrm{Gt\,yr^{-2}}$) is not statistically significant and therefore suggests stability. Contrary to individual SMB measurements, we can not affirm that the integrated SMB is really negative as the averaged $\mathrm{MAR_{ERA}}$ SMB is close to zero and given the biases associated to the used 10 km resolution. Moholdt et al. (2010) highlighted a very negative SMB in 2003–2004 followed by a series of more balanced values between 2004 and 2007. $\mathrm{MAR_{ERA}}$ also suggests very low values of SMB in 2003 and 2004 ($\sim -12\,\mathrm{Gt}$) and more balanced values over 2005–2012. We can therefore conclude that the

SMB has been stable (yet negative) over the past 35 years when integrated over the entirety of Svalbard. The recent trend is however opposite to what has been occurring over the Greenland ice sheet, where the SMB has been stable until the end of the 1990s and record melts have been observed since 2006 and can be explained by the recent change in atmospheric flow frequencies in summer, causing more frequent southerly flows over Greenland but rather northerly flows over Svalbard in summer (Fettweis et al., 2013b).

Over Svalbard, the mean 1979–2005 summer 700 hPa ERA-Interim atmospheric circulation was a westerly or west–southwesterly flow (Fig. 2.6a). After 2005, however, the circulation changed as a result of more frequent North Atlantic Oscillation (NAO) negative phases in summer. $Z700_{JJA}$ (summer 700 hPa geopotential height, representing the general circulation) increased more over Greenland than it did over Svalbard (Fig. 2.6b) resulting in northwesterly flows over Svalbard and more anticyclonic conditions over Greenland (Fettweis et al., 2013b). Consequently, a summer temperature increase breaking melt records has been observed over Greenland since 2006 (Fettweis et al., 2013b). Over Svalbard, on the contrary, the northerly flow brings colder air (Fig. 2.7b, showing temperature at 850 hPa (T850) as it drives the melt variability, according to Fettweis et al. (2013a)), and the surface mass balance has remained stable over the period 1979–2012 despite the recent observed Arctic warming (Anisimov et al., 2007). In summer 2013, however, the 700 hPa summer atmospheric circulation was again a westerly flow and could not oppose Arctic warming anymore. As a result, the 2013 JJA ERA-Interim T850 anomaly with respect to the 1979–2005 mean (Fig. 2.7c) was positive, contrary to the 2006–2012 period, and MAR_{ERA} simulated the highest TAS_{JJA} of the last 35 years (Fig. 2.8), causing the meltwater runoff to break records ($44.1\,Gt\,yr^{-1}$). The 2013 MAR_{ERA} SMB was also the lowest of the last 35 years ($-20.4\,Gt\,yr^{-1}$), whereas the precipitation was higher than average but not significantly different (Fig. 2.5a).

The recent change in the 700 hPa summer atmospheric circulation, damping the effect of the observed Arctic warming over Svalbard is also responsible for the stabilisation of the summer TAS (TAS_{JJA} simulated by MAR_{ERA} in Fig. 2.8) in the second half of the 2000s, as opposed to Greenland. Over the past 35 years, the annual Svalbard temperature has risen by 2.8 °C as shown in Fig. 2.8 whereas the mean summer temperature increase is more moderate (0.79 °C for the past 35 years). Both linear trends are statistically significant but, for the summer temperature, the very high value of 2013 has a large influence on the value of the

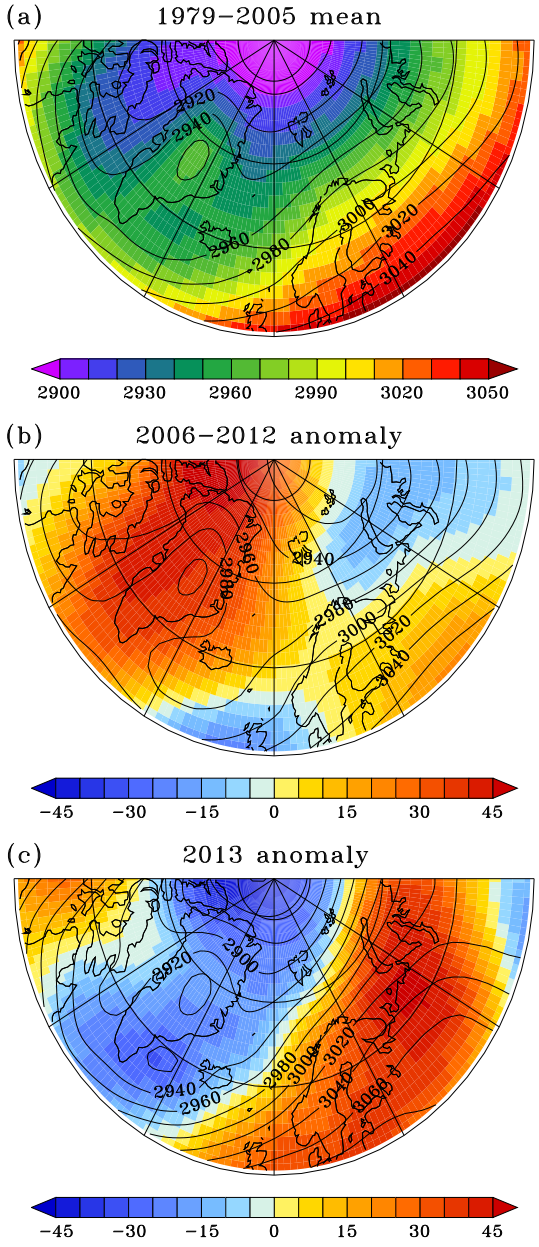

Figure 2.6: **(a)** Mean 1979–2005 JJA geopotential height at 700hPa ($Z700_{JJA}$) (m) from ERA-Interim. **(b)** 2006–2012 mean $z700_{JJA}$ anomaly (m) with respect to the 1979–2005 mean. **(c)** Same as **(b)** but for 2013. The black lines represent the mean $Z700_{JJA}$ for each period

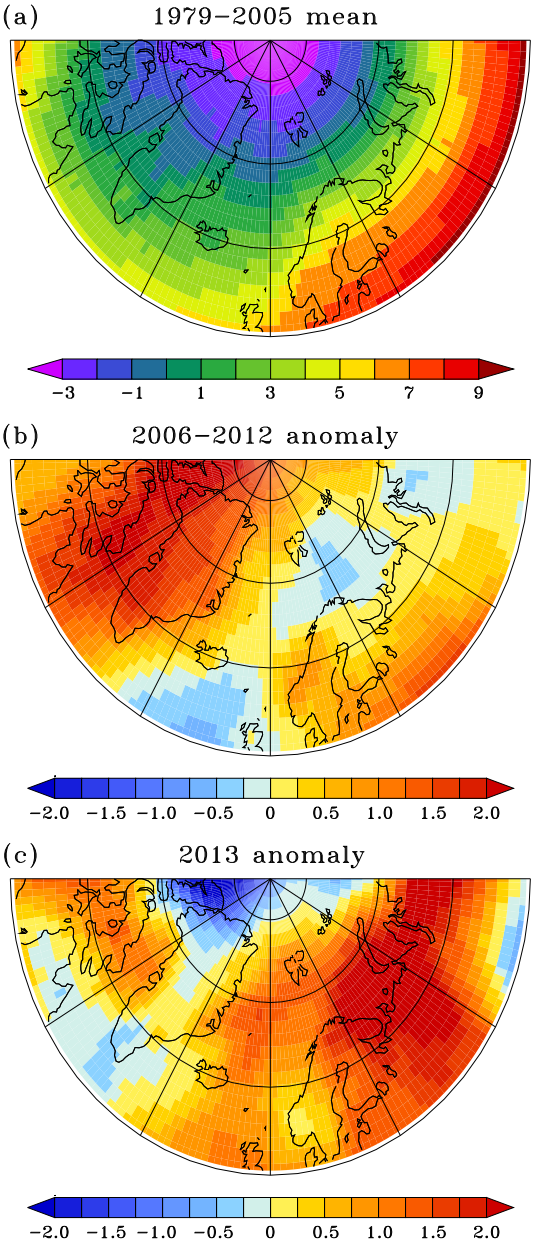

Figure 2.7: **(a)** 1979–2005 $T850_{JJA}$ mean (°C) from ERA-Interim. **(b)** 2006–2012 mean $T850_{JJA}$ anomaly (°C) with respect to the 1979–2005 mean. **(c)** Same as **(b)** but for 2013.

trend given its position at the end of the time series. If we exclude summer 2013, the JJA temperature trend is not statistically significant.

While the mean annual values of precipitation and run-off are quite similar (18.7 and 20.9 $Gt\,yr^{-1}$, Fig. 2.5a), the precipitation amount has been stable

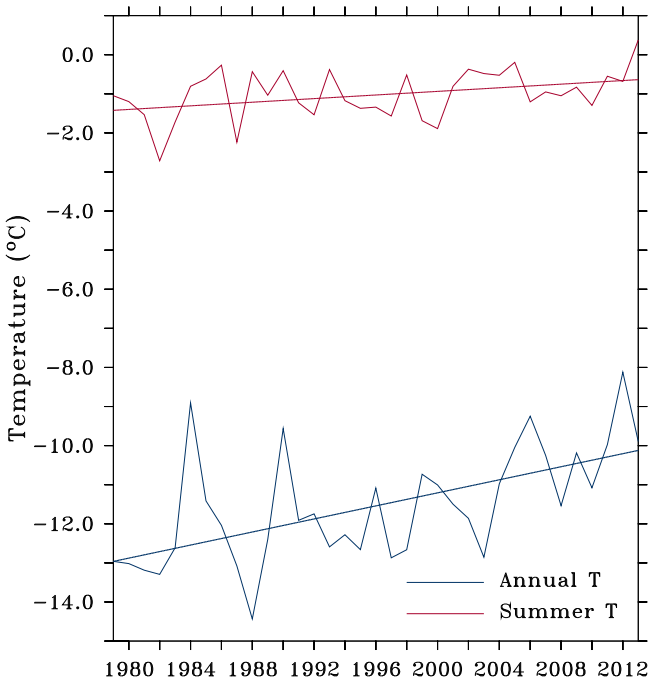

Figure 2.8: Evolution of the mean annual (blue) and summer (red) MAR_{ERA} TAS (°C) integrated over the permanent ice area between 1979 and 2013 with their linear trend.

over 1979–2013 (interannual variability of 2.7 Gt yr^{-1}), whereas the interannual variability of run-off is high (7.4 Gt yr^{-1}). Sublimation and evaporation, for their part, are quite constant and contribute very little to the SMB variability. Their negative values for every year indicate that MAR simulates a greater deposition than sublimation and evaporation. About 64 ± 9 % of the total liquid water (melt plus liquid precipitation) runs off and the remaining 36 % refreezes (Fig. 2.5b). Contrary to runoff and melt, the amount of water that refreezes is constant from year to year (standard deviation of 0.95 Gt yr^{-1} for the refreezing vs. 6.6 Gt yr^{-1} for the melt). Here again, none of the linear trends over 1979–2013 are significant.

The surface mass balance (Fig. 2.9a) is positive only on the ice caps on Nordaustlandet and in high elevation zones in north Spitsbergen where temperatures are low or precipitation high or both. The mean annual TAS (Fig. 2.9c) goes from −5 °C on the west coast of Spitsbergen to almost −15 °C in the centre of the ice caps and in Newtontoppen region (highest elevations, Fig. 2.2). Moreover, there is a west-to-east temperature gradient showing the effect of the North Atlantic Drift bringing oceanic heat to the west coast of the archipelago. This temperature gradient is enhanced by the larger SIC along the east coast that further cools it and increases the contrast with the west coast. The mean TAS_{JJA} (Fig. 2.9d) is positive along the coasts, except in northeastern Spitsbergen and Austfonna where

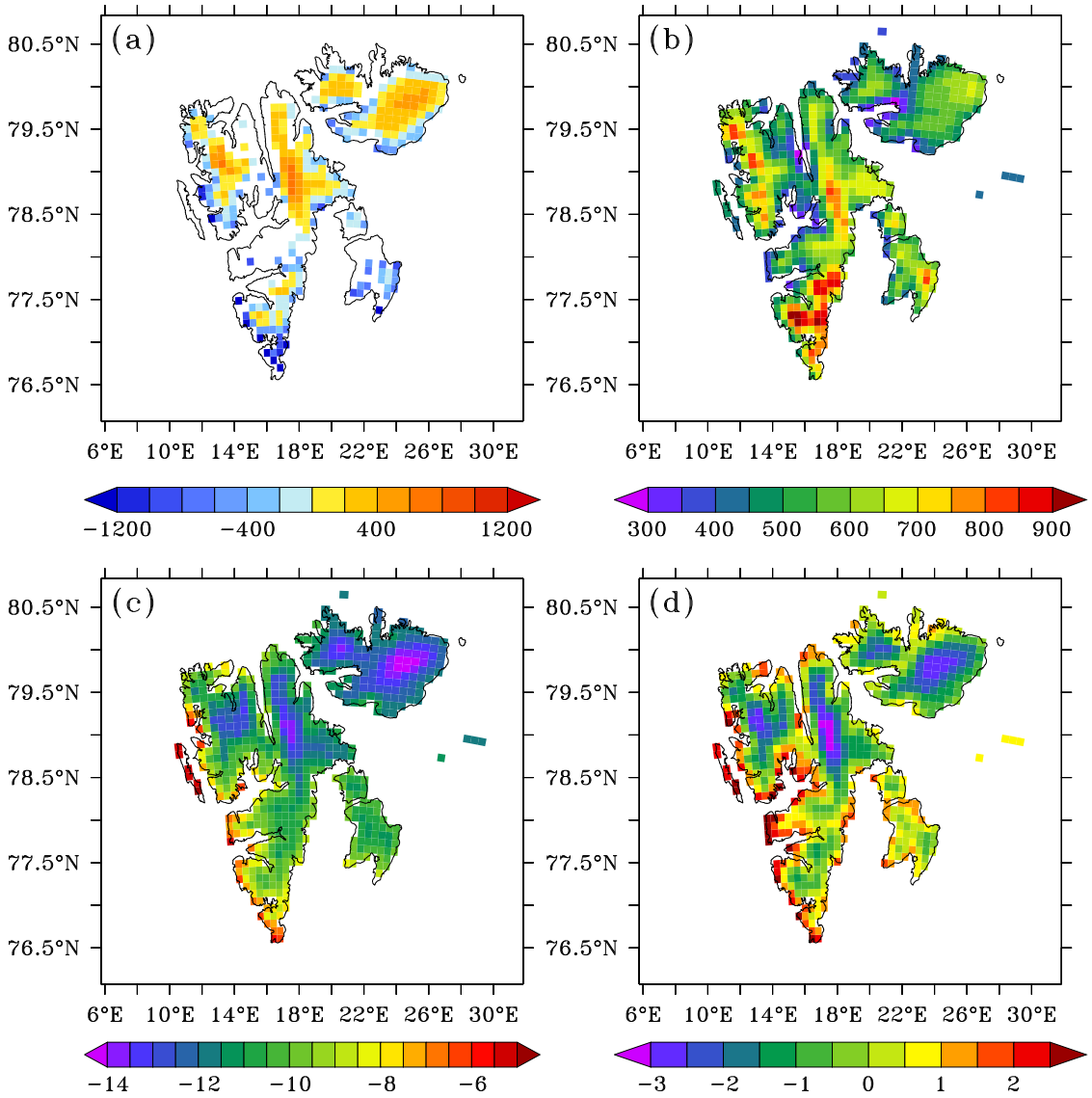

Figure 2.9: **(a)** Mean annual SMB (mm w.e. yr^{-1}) averaged over 1979–2013. **(b)** Same as **(a)** for the annual precipitation (mm w.e. yr^{-1}). **(c)** Same as **(a)** for the mean annual near-surface temperature (TAS) (°C). **(d)** Same as **(a)** for the mean summer near-surface temperature (TAS_{JJA}) (°C).

sea ice is still present in summer. The west-to-east gradient is less pronounced in summer than on the annual timescale as the sea ice strongly decreases on the east coast of Spitsbergen in summer. Precipitation (Fig. 2.9b) is lower on the west coast of Spitsbergen than on the east coast (e.g. on Austfonna) because of frequent depressions in the Barents Sea bringing humid air on the eastern coast of Svalbard (Winther et al., 1998; Hisdal, 1976). Due to the underestimation of the elevation, we can expect precipitation to be lower than observed as MAR likely underestimates the amount of humidity/clouds blocked by the mountains. The impact of the humidity underestimation on the longwave radiation also explains

in part the MAR cold bias. According to Liestøl (1993), the maximum amount of precipitation (more than 1000 mm) is found in the southeastern part of Spitsbergen, where the wind transports humid air onto the mountain slopes. In our case, the maximum is also located in the south of Spitsbergen but it is underestimated (900–950 mm).

The net energy flux (NET) available at the surface for the melt can be written:

$$\mathrm{NET} = \mathrm{SWnet} + \mathrm{LWnet} + \mathrm{SHF} + \mathrm{LHF} \quad (\mathrm{W\,m^{-2}}),$$

where

- SWnet = SWD × (1 − a) is the net downward shortwave radiation, i.e. the amount of the downward shortwave (= solar radiation) energy flux (SWD) that is absorbed by the surface following its albedo (a).

- LWnet = LWD-LWU is the net longwave radiation, i.e. the difference between the downward longwave radiation coming from the atmosphere and the upward longwave radiation emitted by the surface.

- SHF and LHF are the sensible and latent heat fluxes. These fluxes are negligible with respect to the solar and infrared fluxes and are therefore not shown in Fig. 2.10.

Over 1979–2013, the net energy flux at the surface in summer has increased (Fig. 2.10), as a result of increases in both net downward shortwave (SWnet) and longwave (LWnet) summer energy fluxes, giving more energy for the melt. However, only the longwave energy fluxes linear trends are significant. As the summer SWD has been decreasing, the dominant factor causing the increase of SWnet over 1979–2013 is the decrease of the surface albedo. The increase in LWD is a consequence of the increasing greenhouse effect-induced atmosphere warming as well as the significant increase of summer cloud cover (5 % in 35 years with a 1979–2013 mean cloud cover of 73 ± 3 %). The cloudiness increase is also responsible for the SWD decrease through the greater reflection of the sunlight by the clouds.

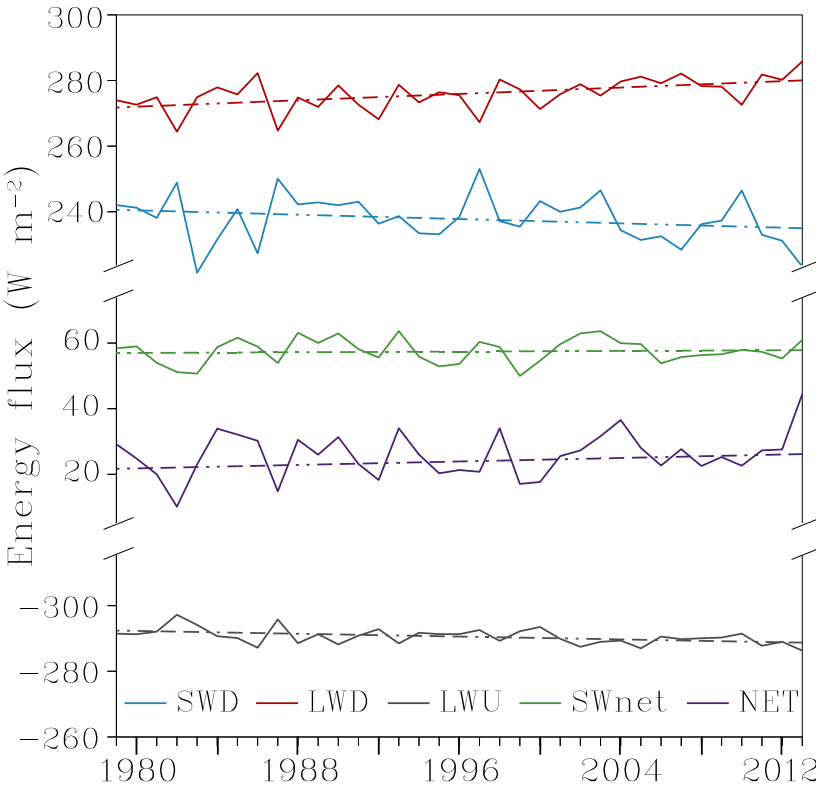

Figure 2.10: 1979–2013 evolution of the JJA energy balance components fluxes ($W\,m^{-2}$) simulated by MAR_{ERA} over the permanent ice area with their linear trends in dashed lines.

2.5 Comparison of ERA-Interim and MIROC5 over Svalbard

With the aim of performing future projections with MAR (Chapter 3), we need a global model (GCM) to force its lateral boundaries, and we need to be sure that MAR forced by the GCM is able to correctly simulate the current climate over Svalbard. Indeed, the future projections will be more uncertain if MAR forced by the GCM shows huge biases over the present. Given the dependency of RCM outputs to the forcings (Fettweis et al., 2013a), it is first necessary to evaluate the GCM itself over Svalbard, to be able to explain the possible biases when MAR is forced by the GCM with respect to MAR forced by ERA-Interim (chosen here as reference over current climate as in Fettweis et al., 2013a). Suitable GCMs are those that are capable of modelling the free atmosphere as MAR is not able to correct possible biases in the free atmosphere in view of the dimension of our integration domain. To achieve this, we have compared Z700, representing the atmospheric circulation and T850, as well as TAS and SIC, as MAR is forced by

SST and SIC over ocean. Among the CMIP5 models evaluated in Fettweis et al. (2013a), MIROC5 (Model for Interdisciplinary Research On Climate, Watanabe et al., 2010; Sakamoto et al., 2012) is one of the best GCMs over Greenland with respect to ERA-Interim. The MIROC5 global model works also well over Svalbard as we will show hereafter. As the historical run ends in 2005, the comparison period extends here from 1980 to 2005.

According to Fig. 2.11, the annual mean MIROC5-based Z700 is higher than ERA's by about 40 to 55 m. The annual positive anomaly is significant at the 95 % confidence level (for clarity, the significant anomalies correspond to the non-hatched areas) whereas the summer difference barely is. We consider the difference significant at the 95 % confidence level if it is higher than twice the standard deviation of the ERA- Interim-based Z700 (representing the interannual variability of Z700). The solid lines, showing the mean Z700, suggests that the circulation is slightly diverted (clockwise for the annual circulation and anticlockwise for the JJA circulation), from ERA-Interim to MIROC5 going from a westerly flow in ERA to a west–northwesterly flow in MIROC5.

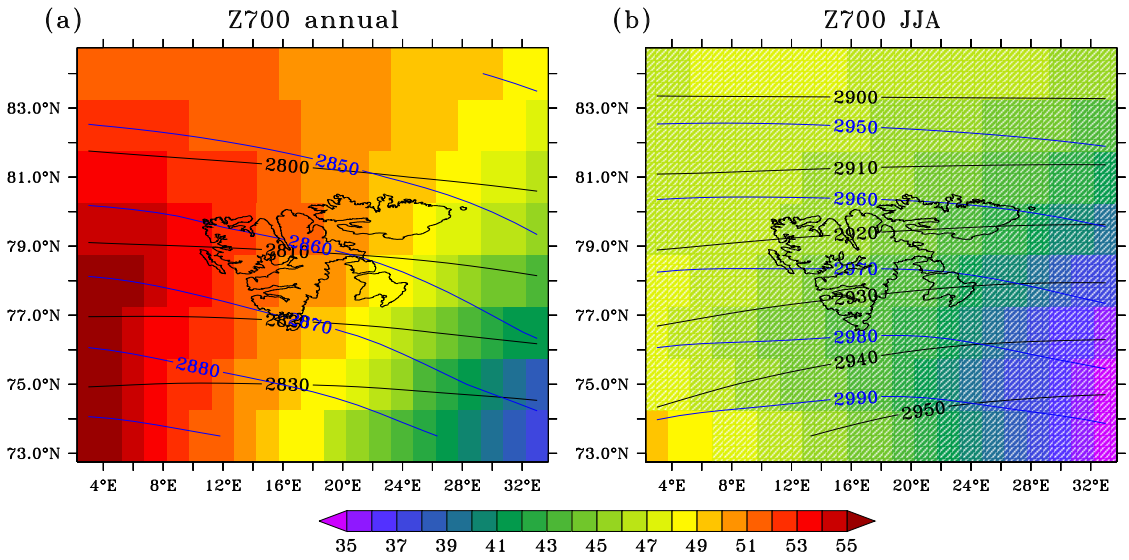

Figure 2.11: **(a)** Difference of mean annual geopotential height (m) at 700 hPa (Z700) between MIROC5 and ERA-Interim over 1980–2005. The black lines show Z700 for ERA-Interim and the blue lines are for MIROC5. **(b)** Same as **(a)** but in summer (JJA). The non-hatched areas correspond to the areas for which the difference is significant at the 95 % confidence level (with respect to the ERA-Interim-based 1980–2005 interannual variability), whereas the hatched areas corresponds to non-significant differences.

At the annual timescale (1980–2005), MIROC5 is colder at 850 hPa than ERA-Interim by 2 to 4 °C, and this difference is significant over the south and east of Svalbard (Fig. 2.12a, annual mean). In summer, this T850 anomaly is not

significant (Fig. 2.12b). At the surface (TAS, Fig. 2.12c and d), the cold bias is even larger, especially at the annual timescale, except in the southwestern corner, where we have a non-significant positive bias. Contrary to the JJA T850 anomaly, the TAS_{JJA} cold bias of MIROC5 with respect to ERA-Interim is significant.

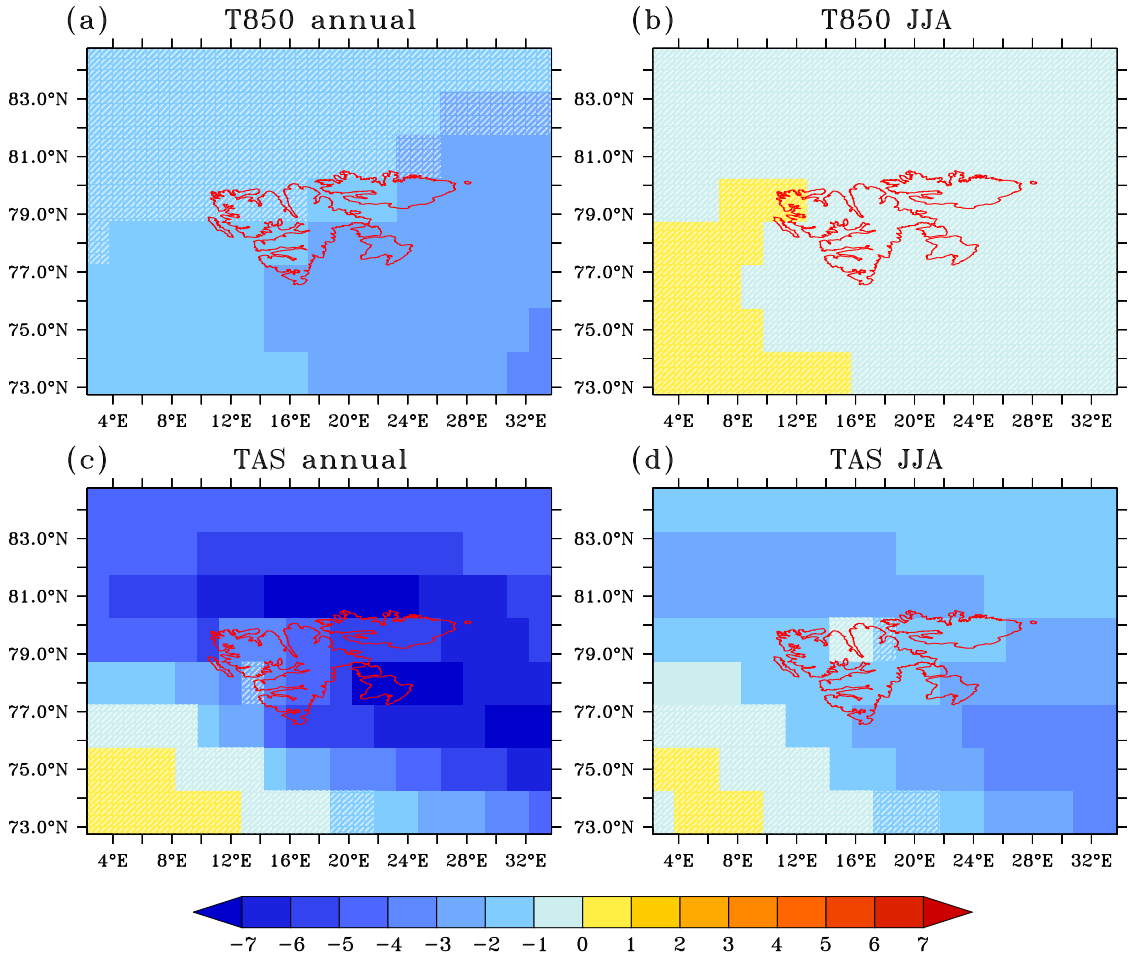

Figure 2.12: **(a)** Annual 850 hPa temperature (T850) difference (°C) between MIROC5 and ERA-Interim over 1980–2005. **(b)** Same as **(a)** but in summer (JJA). **(c)** Same as **(a)** but for the near-surface temperature (TAS, °C). **(d)** Same as **(c)** but in summer (JJA). The non-hatched areas correspond to the areas for which the difference is significant at the 95 % confidence level.

The temperature difference is linked in part to the larger SIC in MIROC5 with respect to ERA-Interim (Fig. 2.13). The only zone where the temperature anomaly is positive corresponds to the zone where the MIROC5 SIC is lower than the ERA-Interim SIC. Conversely, the area in the southeastern corner where MIROC5 prescribes more than 50 % of ice coverage, whereas the ocean is mostly ice free with ERA, corresponds to the zone where MIROC5 is the coldest compared to ERA-Interim.

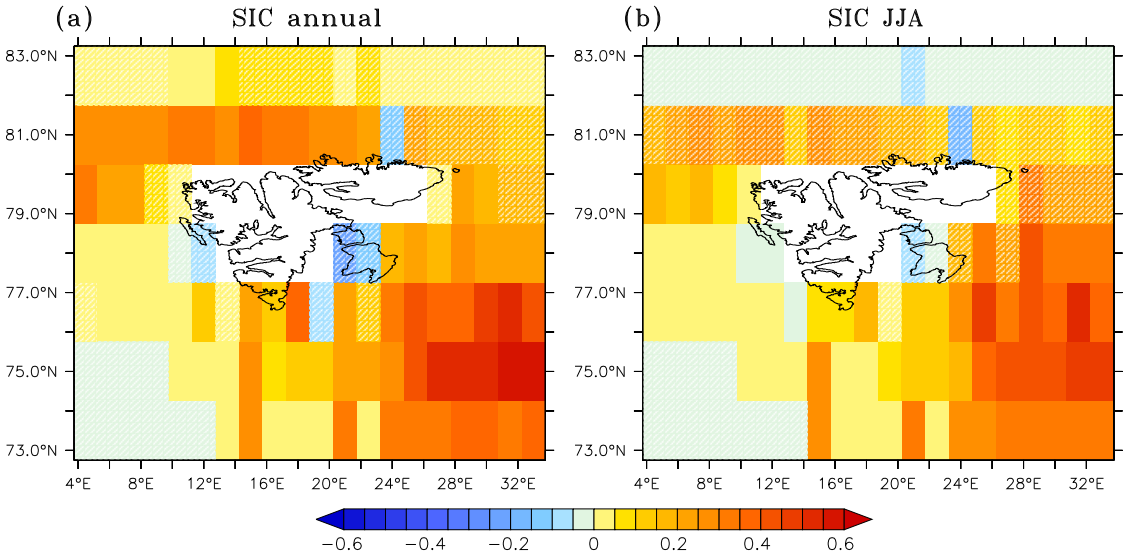

Figure 2.13: **(a)** Annual sea-ice cover (SIC) difference between MIROC5 and ERA over 1980–2005. The SIC go from zero to one according to the portion of the oceanic pixel covered in sea ice (0 = ice-free pixel, 1 = pixel completely covered with sea ice). **(b)** Same as **(a)** but in summer (JJA). The non-hatched areas correspond to the areas for which the difference is significant at the 95 % confidence level.

Contrary to air temperatures that are forced only at the lateral boundaries of our integration domain, SIC and sea surface temperatures (SST) are 6 hourly forced over the entire MAR domain as MAR is not coupled with an oceanic model. Their biases therefore impact on the climate modelled by MAR, especially near the coast, where most of the weather stations are located.

2.6 Comparison of MAR forced by ERA-Interim and MIROC5

According to Fig. 2.14a showing the annual cycle of TAS, MAR forced by MIROC5 (hereafter $\mathrm{MAR_{MIROC5}}$) is colder than $\mathrm{MAR_{ERA}}$ through the whole year: during summer, the difference is close to zero, but it is larger than 5 °C in winter. Integrated over the entirety of Svalbard, the annual SMB is positive with $\mathrm{MAR_{MIROC5}}$ ($+4.0\,\mathrm{Gt\,yr^{-1}}$ on average over 1980–2005, corresponding to $134\,\mathrm{mm\,w.e.\,yr^{-1}}$), whereas Svalbard loses mass on average with $\mathrm{MAR_{ERA}}$ ($-1.6\,\mathrm{Gt\,yr^{-1}}$ or $-54\,\mathrm{mm\,w.e.\,yr^{-1}}$) over 1980–2005. The SMB differences occur mainly in summer through meltwater runoff (Fig. 2.14c) as the precipitation difference (Fig. 2.14d) between $\mathrm{MAR_{ERA}}$ and $\mathrm{MAR_{MIROC5}}$ is much smaller than the runoff difference (only 58 % of the $\mathrm{MAR_{ERA}}$ runoff is modelled by $\mathrm{MAR_{MIROC5}}$,

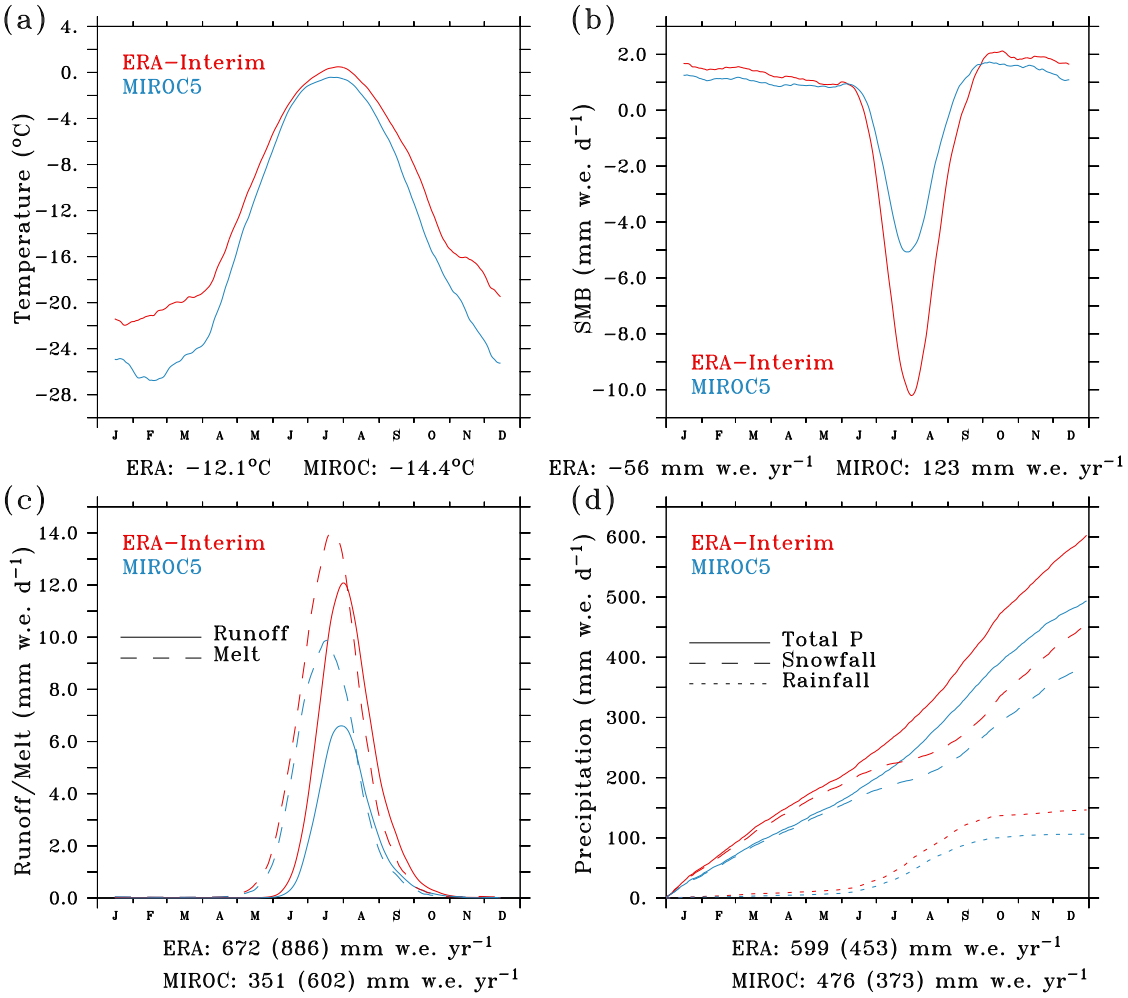

Figure 2.14: **(a)** 1980–2005 mean annual near-surface temperature cycle (°C) for $\mathrm{MAR_{ERA}}$ (red) and $\mathrm{MAR_{MIROC5}}$ (blue). A 30-day running mean has been applied to smooth the curves. The numbers give the mean annual temperature integrated over the permanent ice area for $\mathrm{MAR_{ERA}}$ and $\mathrm{MAR_{MIROC5}}$. **(b)** Same as **(a)** but for the surface mass balance (mm w.e. day^{-1}). The numbers give the annual SMB (mm w.e. yr^{-1}) integrated over the permanent ice area for $\mathrm{MAR_{ERA}}$ and $\mathrm{MAR_{MIROC5}}$. **(c)** Same as **(a)** but for the runoff (solid line) and melt (dashed line) (mm w.e. day^{-1}). The listed numbers give the mean annual runoff, with the melt over the permanent ice area in brackets (mm w.e. yr^{-1}). **(d)** Same as **(a)** but for the cumulated total precipitation (solid line), snowfall (large dashes) and rainfall (small dashes) (mm w.e. day^{-1}). The numbers give the mean annual precipitation and snowfall (shown in brackets) over the permanent ice area (mm w.e. yr^{-1}).

whereas 82 % of the total amount of $\mathrm{MAR_{ERA}}$ snowfall is modelled). The melt season is shorter for $\mathrm{MAR_{MIROC5}}$ than for $\mathrm{MAR_{ERA}}$ ($\sim$ 145 day yr^{-1} vs. $\sim$ 155 day yr^{-1}) and the magnitude of surface melt is also smaller (68 % of the amount of melt in $\mathrm{MAR_{ERA}}$) with $\mathrm{MAR_{MIROC5}}$ (Fig. 2.14c).

The amount of precipitation in $\mathrm{MAR_{MIROC5}}$ is lower than in $\mathrm{MAR_{ERA}}$ (Figs. 2.14d and 2.15a). The difference is caused by (i) the cold bias of MIROC5 (the atmosphere can contain less moisture) and (ii) the difference in SIC between

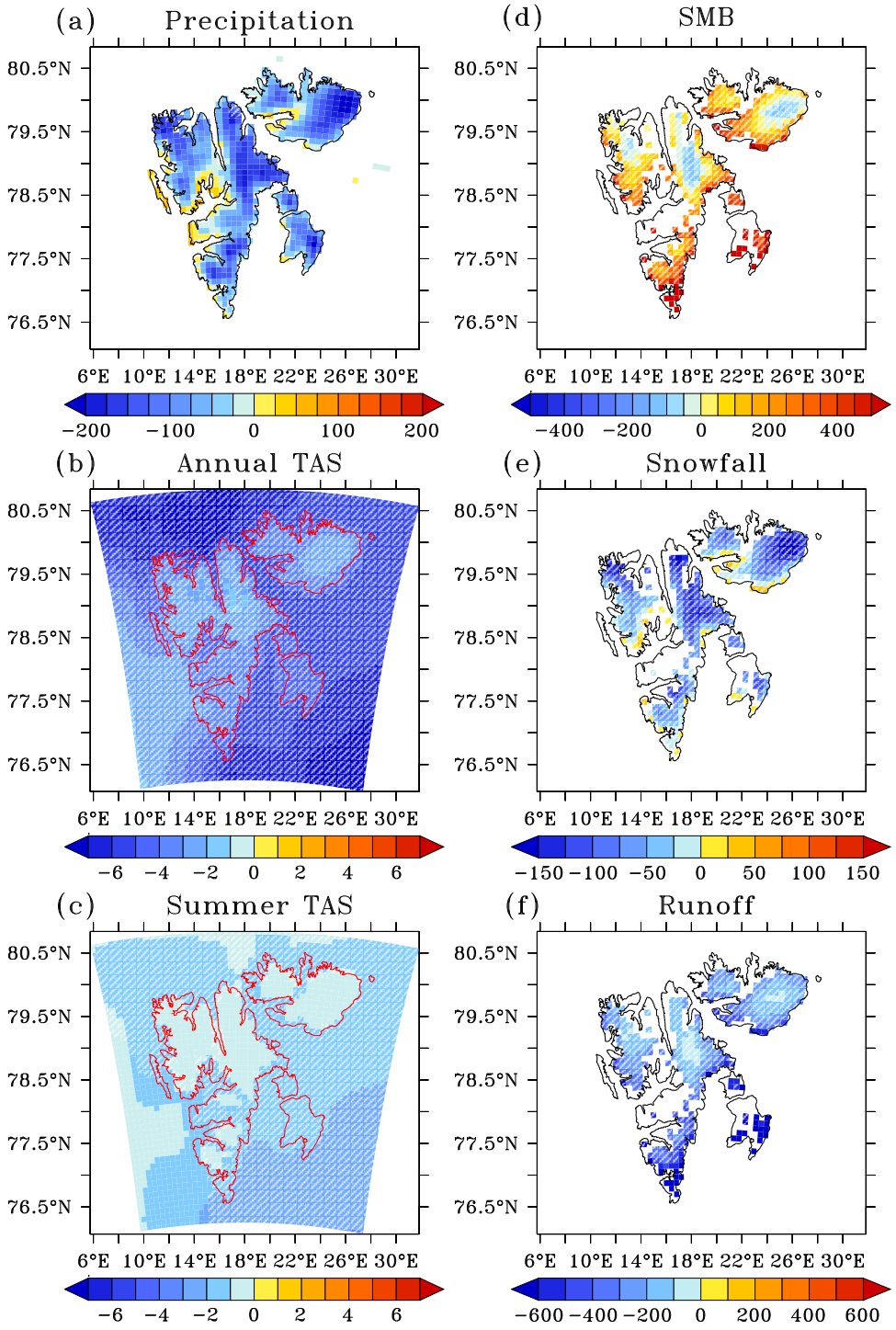

Figure 2.15: **(a)** Annual precipitation difference ($mm\,yr^{-1}$) between MAR_{MIROC5} and MAR_{ERA} averaged over 1980–2005. **(b)** Same as **(a)** but for the annual near-surface temperature (°C). **(c)** Same as **(b)** but for summer (JJA). **(d)** Same as **(a)** but for SMB ($mm\,w.e.\,yr^{-1}$) between MAR_{MIROC5} and MAR_{ERA} averaged over 1980–2005. **(e)** Same as **(a)** but for the snowfall ($mm\,w.e.\,yr^{-1}$). **(f)** Same as **(a)** but for the runoff ($mm\,w.e.\,yr^{-1}$). The non-hatched areas correspond to the areas where the difference is significant.The non-hatched areas correspond to the areas where the difference is significant (i.e. higher than twice the interannual variability of MAR_{ERA}).

ERA-Interim and MIROC5. When the ocean is covered with ice, the exchange of moisture between the ocean and the atmosphere is strongly reduced and so is the amount of water available for precipitation (Noël et al., 2014). An overestimation of SIC also results in a decrease of inland TAS (Noël et al., 2014). The larger SIC in MIROC5 therefore also causes MAR_{MIROC5} to be colder than MAR_{ERA}, especially in the northwestern and southeastern corners of our integration domain according to Figs. 2.15b and 2.13. The bias, still greater than 1.0 °C in the high elevation central regions in the north of Spitsbergen and in the interior of Austfonna, indicates that Svalbard is extremely impacted by the sea surface conditions, even far inland. However, this TAS negative anomaly is also induced by the MIROC5-based free atmosphere, which is too cold at the MAR lateral boundaries. Due to positive feedbacks, it is likely that the SIC overestimation and the too-cold free atmosphere are linked in MIROC5.

Finally, the TAS bias is reduced over land (about 1.5 °C for the annual bias and 1 °C in summer, Fig. 2.15b and c) in MAR_{MIROC5} compared to the MIROC5 bias and becomes significant in MAR_{MIROC5} in summer only near the coast where the sea-ice bias has the greatest influence (Noël et al., 2014), suggesting that MAR is really able to improve the MIROC5 inputs (showing a significant cold bias over most of the land area).

Over 1980–2005, the SMB simulated by MAR_{ERA} (Fig. 2.9 also holds for the 1980–2005 period, as the climate has been stable over the last 35 years) is positive only in the northwestern and northeastern central parts of Spitsbergen and on the ice caps whereas MAR_{MIROC5} predicts a mass gain over most of Svalbard (Fig. 2.16) due to the underestimation of the melt. The only locations where large amounts of mass are lost every year with MAR_{MIROC5} are the west coast and the very southern part of Spitsbergen. Over the reference period, MAR_{ERA} predicts that only 48 % of the area of Svalbard covered with permanent ice has a positive SMB while with MAR_{MIROC5}, 74 % of this area gains mass on average. Integrated over the entirety of Svalbard, the SMB modelled by MAR_{MIROC5} is therefore positive (Table 2.12).

Over most of Svalbard, the MAR_{MIROC5} SMB is larger than the MAR_{ERA} SMB (Fig. 2.15d) because of the run-off deficit in MAR_{MIROC5} (Fig. 2.15f). However, the SMB bias is not significant, given its large interannual variability, except in some places in the very south of Spitsbergen and Edgeøya. The snowfall bias is almost never significant and the areas of significant runoff underestimation in MAR_{MIROC5} are mostly located where the JJA temperature bias is the largest

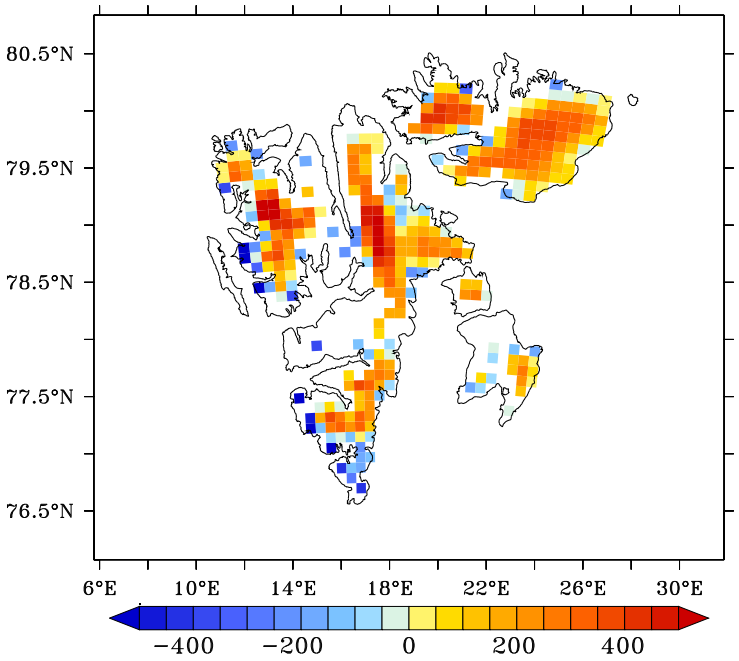

Figure 2.16: 1980–2005 mean annual SMB (mm w.e. yr^{-1}) modelled by MAR_{MIROC5}.

Table 2.12: 1980–2005 mean SMB, its components (Gt yr^{-1}) and annual and JJA TAS (°C) with their linear trends (Gt yr^{-2} and °C yr^{-1}) from MAR_{ERA} and MAR_{MIROC5}. The statistically significant (i.e. superior to twice the interannual variability of the variable in MAR_{ERA} or MAR_{MIROC5}) linear trends are in bold.

	Mean (Gt yr^{-1} – °C)		Trend (Gt yr^{-2} – °C yr^{-1})	
	MAR_{ERA}	MAR_{MIROC5}	MAR_{ERA}	MAR_{MIROC5}
SMB	−1.6	4.0	−0.2	**−0.6**
Runoff	20.2	10.7	0.2	**0.7**
Precipitation	18.1	14.8	−0.004	0.1
Sublimation/evaporation	−0.57	0.15	−0.007	−0.02
Temperature (annual)	−11.2	−15.1	0.05	0.1
Temperature (summer)	−0.9	−1.9	0.03	**0.07**

(Fig. 2.15e and f). In the centre of northern Spitsbergen, the SMB modelled by MAR_{MIROC5} is lower than MAR_{ERA} SMB (coincidently where the later is positive) as it corresponds to areas where the precipitation bias is the largest, likely as a result of too-low temperature in MIROC5 disallowing significant precipitation. In south Spitsbergen and on Edgeøya on the other hand, the precipitation modelled by MAR_{MIROC5} is less underestimated whereas the runoff bias is very negative, hence causing a largely positive SMB bias.

Whereas we saw in Sect. 2.4 that there has been no SMB temporal trend over the past 35 years according to MAR_{ERA}, MAR_{MIROC5} shows a significant SMB trend (−0.6 Gt yr^{-2}, Fig. 2.5). The runoff and summer temperature trends

are also significant, contrary to MAR_{ERA} (Table 2.12). The negative SMB trend is due to the inability of MIROC5 to correctly represent the recent atmospheric circulation change damping the global warming impact over Svalbard, according to Fettweis et al. (2013b). As a result, the summer temperature rises significantly instead of remaining constant and the melt is overestimated in the second half of the 2000s.

2.7 Chapter conclusion

In this study, MAR has been evaluated over Svalbard: although it is too cold, the modelled SMB is close to the measured one in areas where the 10 km resolution is enough to correctly represent the topography (i.e. on Austfonna). On Spitsbergen, on the other hand, the 10 km resolution is not able to resolve the complex topography and therefore the precipitation pattern. As a result, large biases in the SMB are present and higher resolutions are therefore needed to correctly simulate the SMB in this area.

What has been observed on several glaciers between the 1960s and the 1990s has been extended to the present day over the entirety of Svalbard in this study: there has been no significant temporal change of the surface mass balance over the last 35 years despite the global change-induced Arctic warming observed since the end of 1990s (Serreze et al., 2009). Because of the recent change in atmospheric circulation in summer (favouring northwesterly flow over Svalbard), there has not been any recent record surface melt in Svalbard like in Greenland until 2013. In 2013 on the other hand, the atmospheric circulation was again a westerly flow over Svalbard, causing the SMB to break a record in Svalbard whereas the melt was much more moderate in Greenland. This shows the important role of general circulation anomalies in summer and the need to have time series long enough to know if these recent circulation changes are due to natural variability or not.

With the perspective of performing future simulations, we have compared MIROC5 and ERA-Interim over Svalbard as well as MAR forced by MIROC5 and ERA-Interim over 1980–2005. Averaged over 1980–2005, MIROC5 is significantly colder than ERA-Interim and prescribes more sea ice that impacts the temperature over land and the precipitation simulated by MAR. MAR_{MIROC5}, however, has proven able to improve the MIROC5 results, and the SMB, runoff and precipitation differences to the MAR_{ERA} simulations are barely significant. In summer, the

near-surface temperature difference over the land is significant only close to the coastline.

If we look at the temporal evolution of the SMB, on the other hand, MAR_{MIROC5} SMB shows a significant negative trend, contrary to MAR_{ERA} SMB, because MIROC5 does not represent the recent atmospheric change that caused the SMB of Svalbard to remain constant on average. However, integrated over the entirety of Svalbard, the differences are not statistically significant, suggesting that the MIROC5-forced future projections should not be affected a lot by the biases over current climate with respect to the ERA-Interim-forced run.

CHAPTER 3

Future climate and surface mass balance of Svalbard glaciers in an RCP8.5 climate scenario: a study with the regional climate model MAR forced by MIROC5

We present in this chapter the results of our future projection of the Svalbard climate and surface mass balance with MAR forced by the global model MIROC5. We start with the future SMB of Svalbard and its regional evolution through the 21st century (Sect. 3.2) In Sect. 3.3, we investigate the temperature change and how it should be impacted by the sea ice cover decrease. In Sect. 3.4, we describe the evolution of the melt season and, finally, the sensitivity of the energy balance components to rising temperatures is investigated in Sect. 3.5.

The content of this chapter has been published in *The Cryosphere*, 9, 945–956, 2015 (Lang et al., 2015b).

3.1 Model and climate forcings

The version and forcings of the model are the same as those used over the present era in Chapter 2. We ran MAR over the period 2006–2100 at a spatial resolution of 10 km. The lateral and upper (tropopause) boundaries (temperature, humidity, wind speed and surface pressure) as well as oceanic boundaries (sea surface temperature and sea ice cover) were forced every 6 h by the MIROC5 global model (Model for Interdisciplinary Research on Climate; Watanabe et al., 2010; Sakamoto et al., 2012) using the RCP8.5 scenario (Moss et al., 2010).

MIROC5 has been successfully evaluated over Svalbard in Chapter 2. MIROC5 performs as one of the best CMIP5 GCMs (general circulation models) over Greenland (Fettweis et al., 2013a; Belleflamme et al., 2013). Over Svalbard, MIROC5 also performs well and the near-surface temperature bias from MIROC5 is no longer significant over land in MAR forced by MIROC5. As a result, SMB, precipitation and runoff modelled by MAR forced by ERA-Interim and MIROC5 are not significantly different over the present era.

Melt increases non-linearly with temperature, so it is very important to realistically simulate the present climate, especially the elevation of the 0 °C isotherm. Of course, simulating a realistic current climate does not necessarily mean that future changes are also robust. CMIP5 GCMs do not project significant circulation changes in the Arctic (Belleflamme et al., 2013) so that projected temperature changes dominate the SMB change (Fettweis et al., 2013a). The temperature increase projected by MIROC5 follows the CMIP5 ensemble mean

until 2060 (Fig. 3.1) and exceeds the ensemble mean after that. Our projection for 2100 with this forcing may therefore be representative for later decades, and does not alter the main results. The extreme scenario RCP8.5 was chosen to have a forced warming signal that significantly exceeds natural interannual variability.

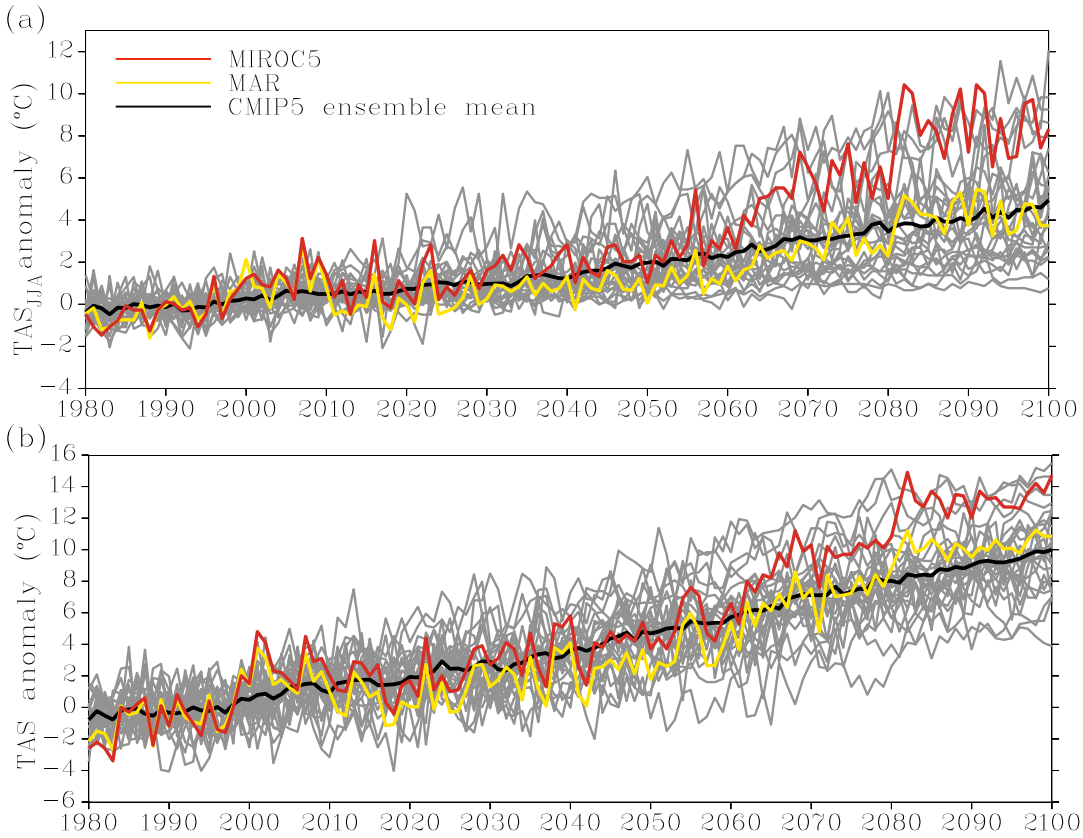

Figure 3.1: **(a)** 1980–2100 evolution of the JJA near-surface temperature (TAS_{JJA}, °C) anomaly over Svalbard with respect to the 1980–2005 mean simulated by MIROC5 (red curve), the CMIP5 GCMs (grey curves), the ensemble mean (black curve) and MAR forced by MIROC5 under the RCP8.5 scenario (yellow curve). **(b)** Same as **(a)** but for the annual near-surface temperature.

3.2 Surface mass balance

Figure 3.2a shows that MAR SMB is projected to be negative on average over 2070–2099 over the entire archipelago, according to the MIROC5-based RCP8.5 scenario. $MAR_{RCP8.5}$ predicts that the greatest losses will mostly happen in the southern part of Spitsbergen with values lower than $-4000\,\mathrm{mm\,w.e.\,yr^{-1}}$ in the most extreme cases, where we also have the largest differences compared to the 1980–2005 average (Fig. 3.2b and Fig. 2.16 in Chapter 2 (MAR_{histo})). This

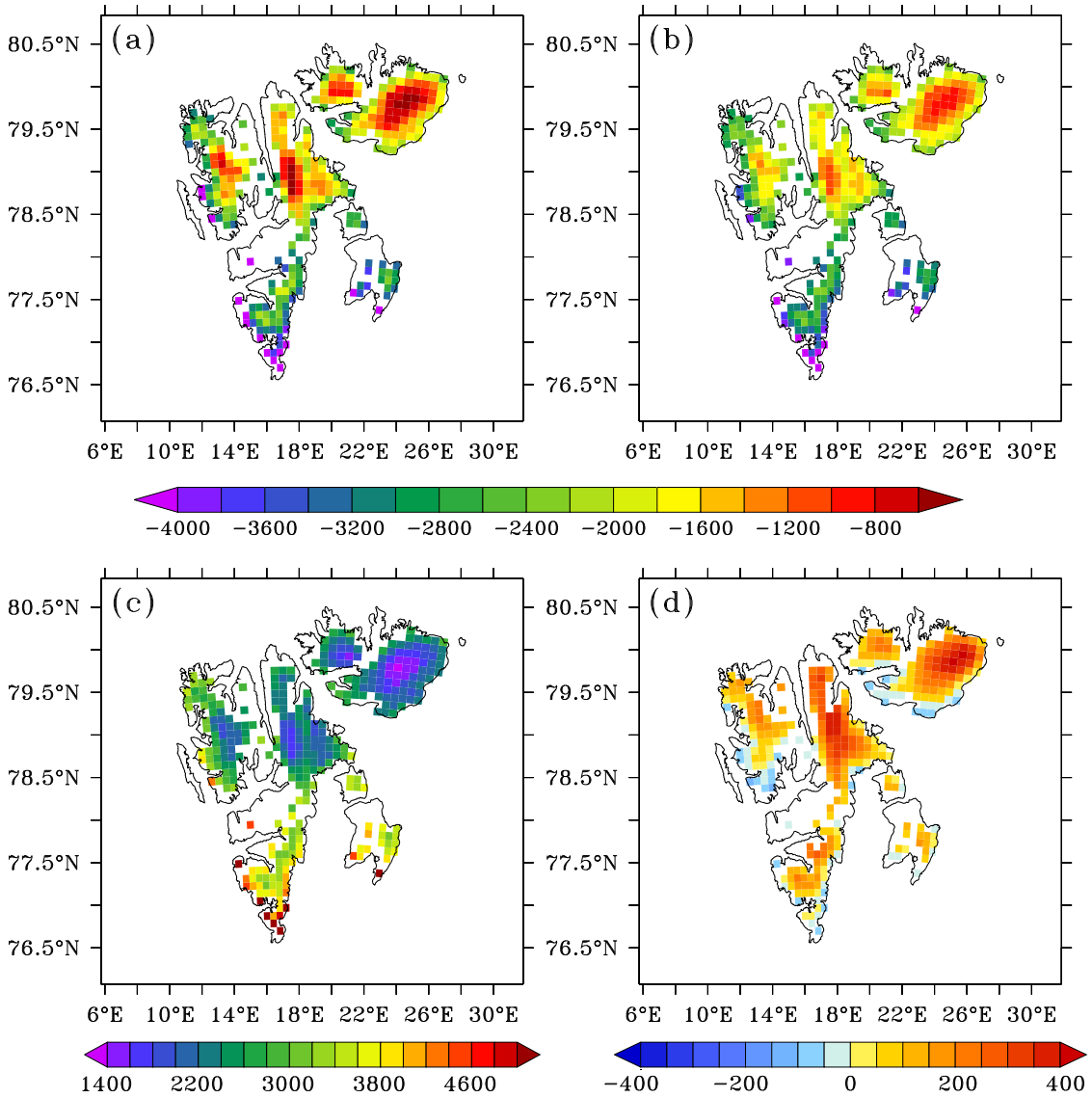

Figure 3.2: **(a)** 2070–2099 mean SMB (mm w.e. yr^{-1}) as simulated by MAR forced by the MIROC5-based RCP8.5 scenario. **(b)** Difference between **(a)** and the 1980–2005 mean shown in Fig. 2.16 in Chapter 2. **(c)** Same as **(b)** but for runoff. **(d)** Same as **(b)** but for precipitation.

suggests that the surface mass loss from small southern glaciers will be higher than over the ice caps and large ice fields of northern Spitsbergen. The mean 2070–2099 meltwater runoff anomaly is largely positive (Fig. 3.2c), and the largest anomalies (> 5000 mm w.e. yr^{-1}) are also located in the south of the archipelago. The snowfall will mostly increase (Fig. 3.2d) but not nearly enough to compensate for the increase in meltwater runoff, as also simulated by MAR over the Greenland ice sheet (Fettweis et al., 2013a) and by RACMO2 (Regional Atmospheric Climate Model) in the Canadian Arctic Archipelago (Lenaerts et al., 2013). At lower elevations, however, the snowfall anomaly is mostly negative because the winter

solid precipitation increase will not be able to compensate for the summer decrease as a large part of the current snowfall is projected to become rainfall at the end of this century.

Figure 3.3, showing the temporal evolution of the annual SMB for five different regions around the archipelago, confirms that the surface mass loss acceleration after 2050 is larger in the south of the archipelago than in the north.

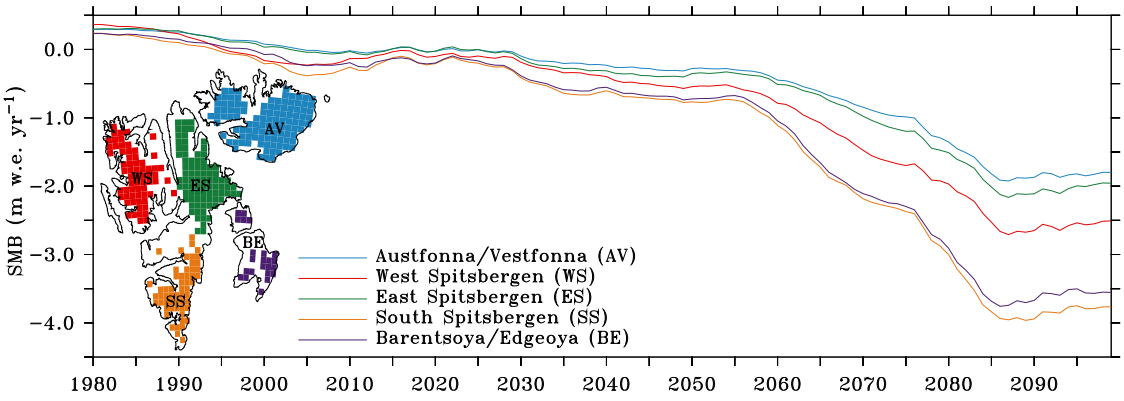

Figure 3.3: SMB 10-year running mean (m w.e. yr^{-1}) for five different regions (Austfonna and Vestfonna, west Spitsbergen, east Spitsbergen, south Spitsbergen and Barentsøya and Edgeøya) as simulated by MAR forced by the MIROC5-based historical scenario over 1980–2005 and RCP8.5 afterwards. The units are in m w.e. yr^{-1} (rather than Gt yr^{-1}) to be independent of the different areas of the regions. The permanent ice mask of each region defined for the regional evolution is shown in the inset.

$\text{MAR}_{\text{histo}}$ and $\text{MAR}_{\text{RCP8.5}}$ project a similar SMB evolution for all our five regions until 2050. After 2050, the acceleration of surface mass loss is projected to increase suddenly and be more pronounced in the south of Spitsbergen and on Barentsøya and Edgeøya (BE) than in west/east Spitsbergen and on Austfonna and Vestfonna (AV). After 2085, the surface mass loss is projected to stabilise and even to decrease slightly according to the MIROC5-based RCP8.5 scenario. The SMB future evolution is primarily determined by the significant runoff increase (Fig. 3.4a) as the snowfall remains much more constant in time and very similar from region to region (Fig. 3.4b). The increasing summer near-surface temperature (TAS_{JJA}, JJA for June–July–August) explains in part the acceleration of melt around 2050 but not the regional differences (Fig. 3.4c), which result rather from the surface JJA albedo–melt feedback (Fig. 3.4d) associated with the expansion of the ablation/bare ice zone as also projected over the Greenland ice sheet (Franco et al., 2013).

However, the JJA albedo–melt feedback is partly reduced in the west by the decrease of the solar flux at the surface caused by a larger cloud optical depth in

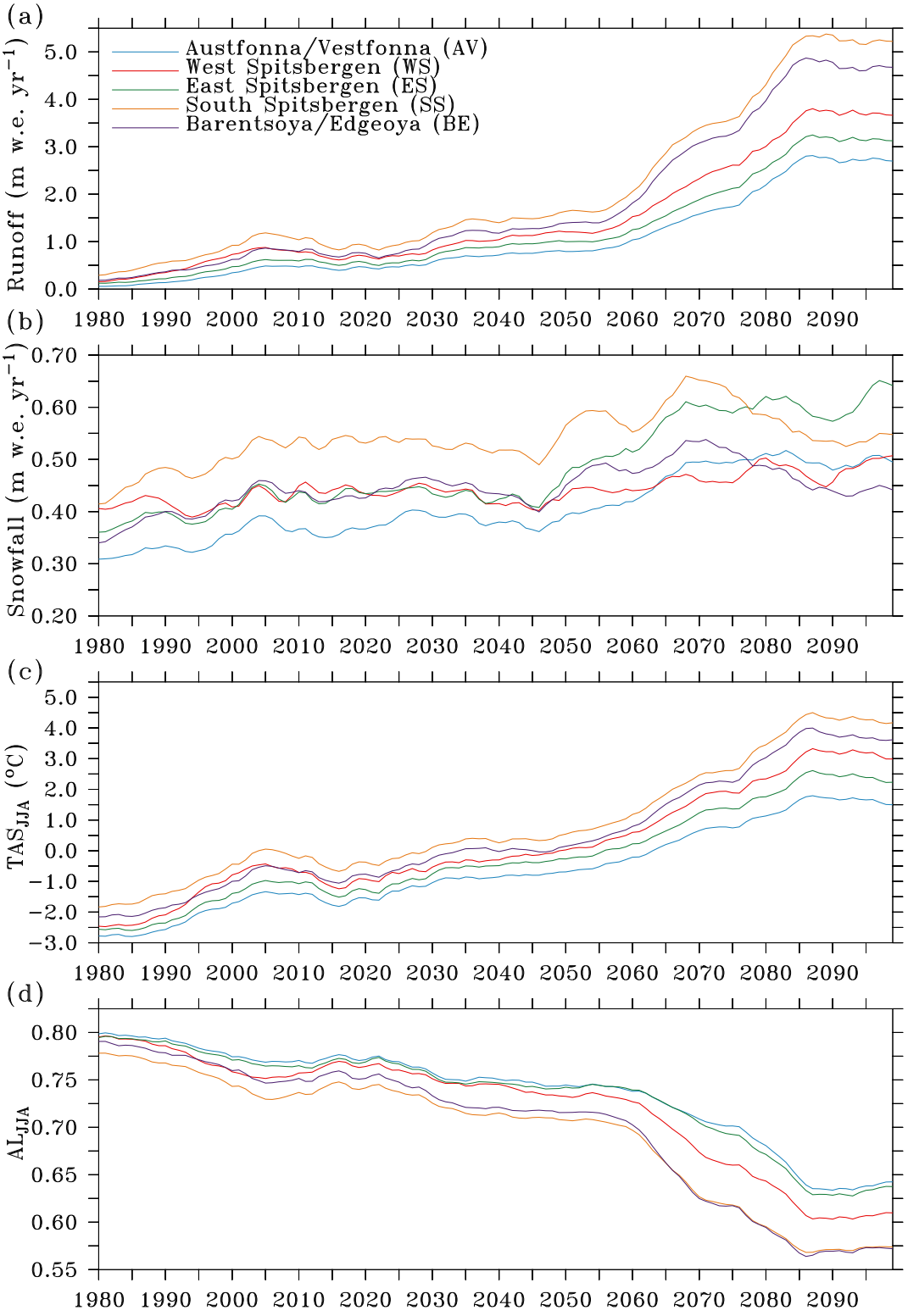

Figure 3.4: **(a)** 10-year running mean of the meltwater runoff (RU, m w.e. yr^{-1}) over 1980–2099 for the five regions shown in Fig. 3.3. **(b)** Same as **(a)** but for snowfall. **(c)** Same as **(a)** but for the JJA near-surface temperature (TAS$_{JJA}$,°C). **(d)** Same as **(a)** but for the JJA surface albedo (AL$_{JJA}$).

west and south Spitsbergen in summer, compared to the northeast and the AV ice caps (Fig. 3.5a and b). The larger cloud optical depth in the west and the south is caused by a warmer and therefore more humid atmosphere. As a result, despite a larger decrease of JJA surface albedo in west Spitsbergen than in the other northern regions, the amount of net shortwave radiation absorbed by the surface in west Spitsbergen is closer to the amount over the other regions (Fig. 3.5c).

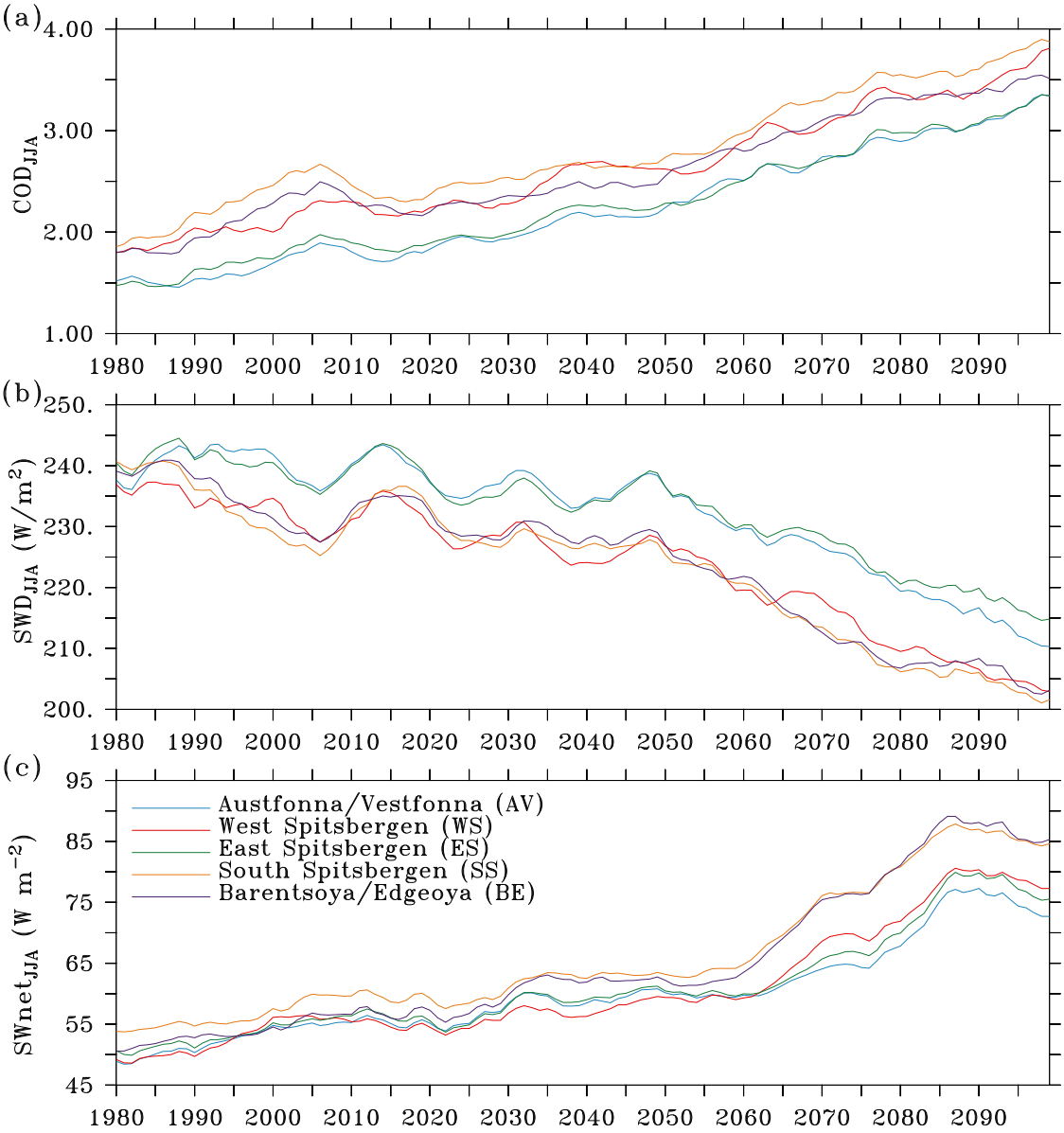

Figure 3.5: **(a)** 10-year running mean of the JJA cloud optical depth (COD_{JJA}). **(b)** Same as **(a)** but for the JJA incoming solar radiation at the surface (SWD_{JJA},W m^{-2}). **(c)** Same as **(a)** but for the JJA net solar radiation at the surface ($SWnet_{JJA}$,W m^{-2}).

Figure 3.6 shows the projected yearly anomaly (with respect to the historical mean) of SMB integrated over the 21st century. This gives an estimate of the

impact on the ice caps topography of the SMB changes integrated over this century (by assuming that there is no change in ice dynamics). In the south and along the

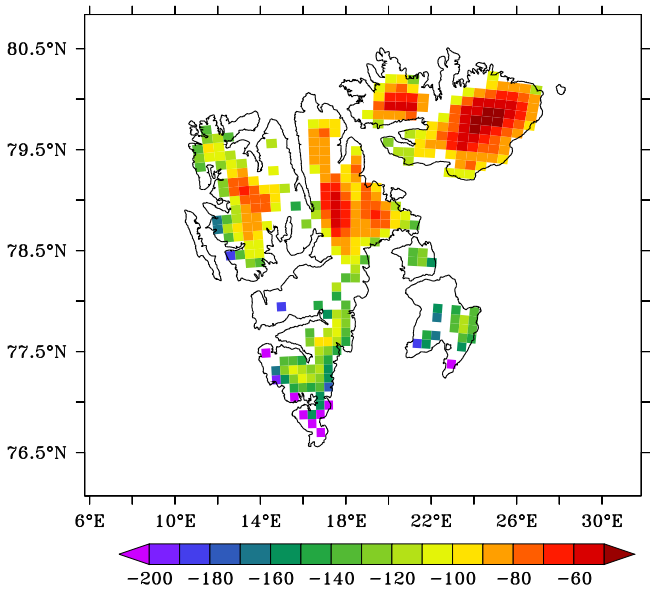

Figure 3.6: Projected cumulated anomaly of SMB changes (m w.e.) over the 21st century. The SMB anomaly is the difference with the 1980–2005 mean and has been summed over 2000–2100.

west coast, some glaciers could lose more than 200 m w.e. over the 21st century. BE is projected to be the first of our five regions to undergo net ablation as $MAR_{RCP8.5}$ projects that the accumulation zone on BE will disappear by 2065 and will be reduced to less than 5 % of the total glaciated area of BE as early as 2035 (Fig. 3.7). In south Spitsbergen, the vanishing of the accumulation zone is projected to happen around 2065 and even Austfonna and Vestfonna will undergo net ablation at the end of the 21st century, leading to rapid degradation of firn. However, on Austfonna, given the large ice thickness (Dowdeswell et al., 2008), we expect that a great part (in area) of the ice cap will still remain at the end of the century even if the SMB is negative everywhere and that the retreat will only concern the margins in 2100.

Over the whole 21st century, the integrated Svalbard $MAR_{RCP8.5}$-based SMB decrease corresponds to a mass loss of 2600 km^3 w.e. (i.e. 2827 km^3 of ice) with respect to the historical mean. The $MAR_{RCP8.5}$ SMB decrease compared to the present value is therefore projected to contribute 7.2 mm to the 21st century sea level rise (SLR), according to MIROC5-based $MAR_{RCP8.5}$. Radić et al. (2014) calculated a mean value of the sea level rise associated with the 21st century SMB changes of Svalbard with a positive degree-day (PDD) model based on the outputs of an ensemble of 14 GCMs for the RCP8.5 scenario. Their projected

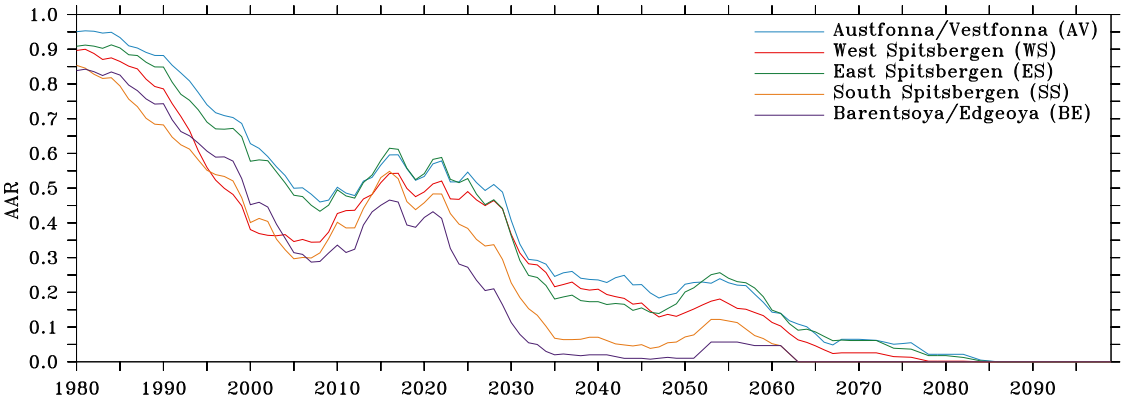

Figure 3.7: 10-year running mean of the accumulation area ratio (AAR) over 1980–2099 for the five regions shown in Fig. 3.3. AAR represents the ratio of the area of the accumulation zone of a region compared to the total area of the region, i.e. the proportion of a region that is in the accumulation area.

SLR at the end of the century is more than twice as large as ours (15.81 mm). Marzeion et al. (2012) projected a SLR between 15 and 25 mm for Svalbard for the RCP8.5 scenario, with an empirical model based on the outputs of climatologies and CMIP5 GCMs. However, these values were based on large-scale temperature and precipitation changes from global models, in most of which the topography of Svalbard is not explicitly represented given their huge spatial resolution. Moreover, the surface temperature of glaciated regions is limited to 0 °C in MAR, damping the MAR near-surface temperature increase (Fig. 3.1), whereas there is no limitation in most GCMs (Goelzer et al., 2013). Additionally, those studies are based on empirical calculations of the energy balance while ours are physically based, which also explains part of the differences in SMB values. Finally, there is also an error in our estimation due to the use of a fixed ice mask and topography. However, we estimate this error to be small (10 % of the SMB anomaly, see discussion below) and the SLR contribution from MAR would still have been twice as small as the Marzeion et al. (2012) and Radić et al. (2014) estimations had we not used a fixed ice mask and topography. Radić et al. (2014) estimated the total present ice volume of Svalbard to be 9089 km^3, which corresponds to a potential sea level rise of 23 mm. Our projection therefore suggests that 31 % of their present estimated volume will disappear by 2100. According to a previous estimate of 7000 km^3 (equivalent to a sea level rise of 20 mm) by Hagen et al. (1993), about 40 % of the ice mass is projected to disappear by 2100 in our projection, due to surface mass loss only.

As shown in Chapter 2, a resolution of 10 km smoothes the topography, especially on Spitsbergen where the topography is very steep. As a result, the

elevation is underestimated over a large part of Svalbard and some low altitude glaciers should not even exist in our 10 km grid, causing a likely overestimation of the surface mass loss in our projection. Moreover, glaciers are typically concentrated at higher elevations, where the negative elevation bias in MAR is largest, leading to further overestimated mass loss. The topography is also fixed in our simulations, which is an acceptable approximation under the present climate but will likely introduce an underestimation of the melt increase in the future, as a result of surface lowering. On the other hand, glaciers are going to retreat in the future, and using a fixed ice mask like we do overestimates the melt, as some areas should not be covered with permanent ice under the future warmer climate. The contribution of these areas (with relatively high mass loss) to the sea level rise should be removed in our projection. As the aforementioned effects partly compensate for each other, we expect a relatively minor impact on our future projection. According to Goelzer et al. (2013), the additional SMB changes coming from topography changes are about 10 times lower than SMB changes directly induced by climate warming. Over the Greenland ice sheet, those effects are projected to contribute to about only 5–10 % of the SMB anomaly by the end of the century (Fettweis et al., 2013a) and we assume their contribution to be of the same order of magnitude in Svalbard. However, only a high-resolution simulation coupled with an ice sheet model could yield insight in the magnitude of this contribution. In southern Spitsbergen, given the very negative values of SMB and the fact that glaciers rather than ice caps prevail, we expect the retreat effect to be dominant and $MAR_{RCP8.5}$ probably overestimates the surface mass loss in this area. On Austfonna, on the other hand, we expect the retreat to be limited only to the proximity of the margins, but the elevation decrease towards the centre of the ice cap is also expected to be limited. We therefore expect that, on Austfonna, both effects will balance each other out, or at least that none of them will be largely dominant.

3.3 Near-surface temperature

$MAR_{RCP8.5}$ predicts a rather small near-surface temperature increase in summer (TAS_{JJA} increase of 3.0 to 6.5 °C) compared to the winter increase (TAS_{DJF} (December–January–February) increase of 11 to 25 °C) (Figs. 3.8c, d and 3.12a). The spatial range of temperature increase over our domain is also much smaller in summer than in winter (3 °C vs. almost 15 °C), due to the presence of

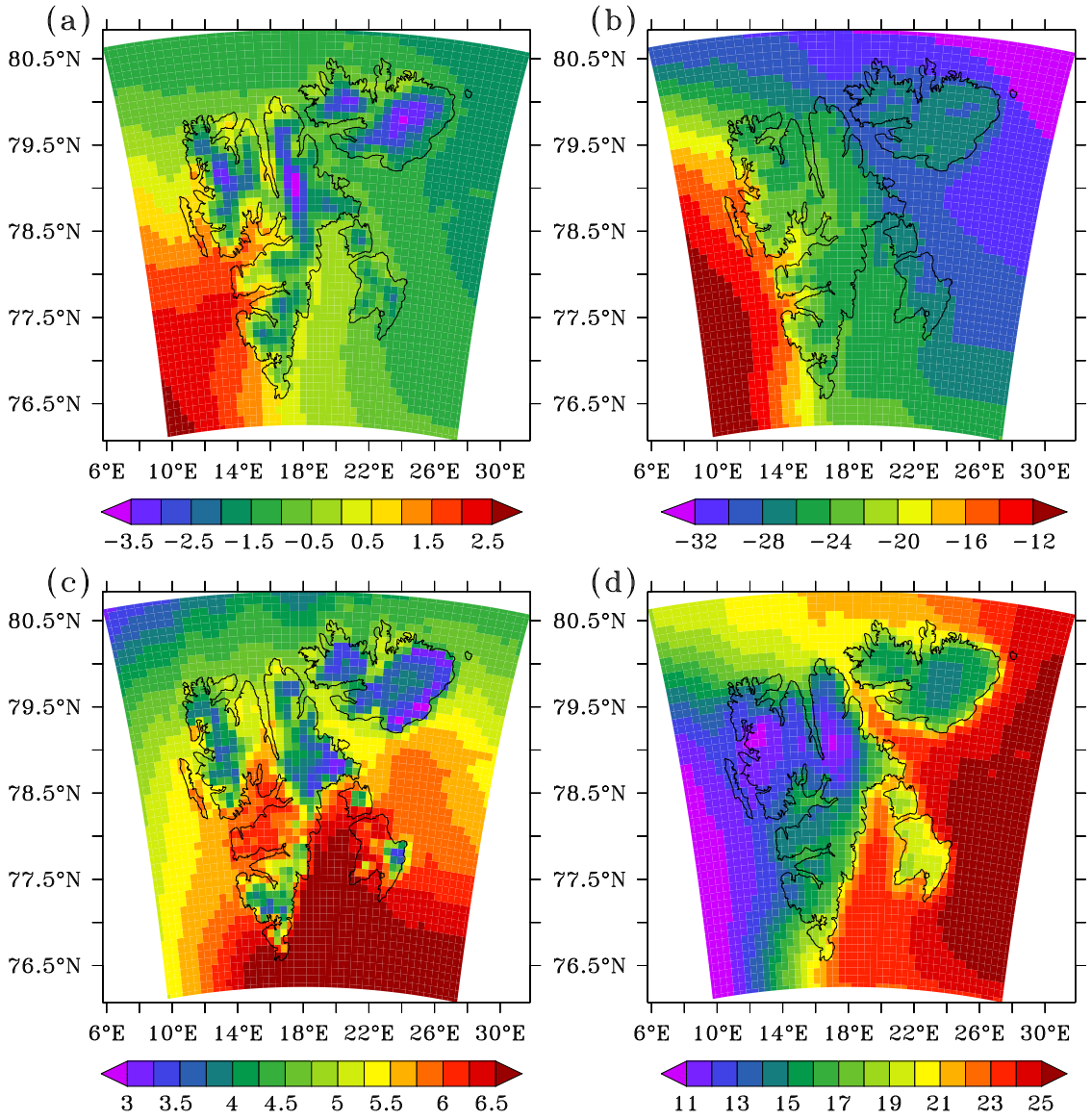

Figure 3.8: **(a)** 1980–2005 mean summer (JJA) near-surface temperature (°C). **(b)** Same as **(a)** but for winter (DJF). **(c)** 2070–2099 mean summer (JJA) near-surface temperature anomaly (°C) with respect to the 1980–2005 mean. **(d)** Same as **(c)** but for winter (DJF).

a 10 °C west-to-east winter gradient projected by MAR.

The pattern and magnitude of the temperature increase modelled by $MAR_{RCP8.5}$ are similar to Day et al. (2012) estimates. Førland et al. (2011) projected a temperature increase in Longyearbyen of 2.8 and 10.4 °C in JJA and DJF by the end of the century using B2, A1B and A2 scenarios while our temperature is projected to increase by 6 °C in JJA and 14 °C in DJF. Considering that Day et al. (2012) and Førland et al. (2011) worked with B2, A1B and A2 scenarios and we used RCP8.5, it is to be expected that our temperature increase is larger (Rogelj et al., 2012), and we can conclude that our results are in qualitative

agreement with those of Day et al. (2012) and Førland et al. (2011).

In summer, TAS is already close to 0 °C over the historical period (Fig. 3.8a) and can not increase very much because the excess energy available at the surface is used to melt snow/ice. According to our MIROC5-based RCP8.5 scenario, JJA temperature is projected to increase by 3.75 to 4.75 °C over the glaciated areas (Fig. 3.8c) and the only regions where the TAS increase is larger (up to 6.5 °C) are regions with small permanent ice area at present, i.e. BE and Nordenskiöld Land (orange/red area separating the north and south of Svalbard in Fig. 3.8c).

The higher temperature increase in winter is due to (i) very low present-day DJF temperatures (Fig. 3.8b) allowing it to increase much more before reaching freezing point and (ii) the projected decrease of the winter sea ice cover (SIC) (also highlighted by Day et al. (2012) and Førland et al. (2011)), that is also responsible for the large west-to-east temperature gradient. At present, there is a large west-to-east SIC gradient, caused by the North Atlantic Drift, preventing sea ice from forming west of Svalbard. In a warming climate, the SIC gradient will decrease, hence strongly reducing the west-to-east gradient in near-surface air temperature.

In the future, near-surface temperature will increase more in areas where sea ice can decrease. Therefore, in the west, as there is already no significant sea ice cover in the present climate, the projected temperature increase is much lower than in the east. We have shown in Chapter 2 that the ocean has a large influence on the climate in Svalbard, even quite far inland. In Fig. 3.8a, showing the 1980–2005 mean JJA TAS, the temperature follows the topography whereas in winter (Fig. 3.8b), the most dominant temperature gradient is the west-to-east gradient due to the presence or absence of sea ice. At the end of the century, the effect of topography is projected to become dominant in winter (Fig. 3.9b) as most of the sea ice will have disappeared according to the MIROC5-based RCP8.5 scenario. The DJF east coast maximum temperature increase in Day et al. (2012) is located on the east coast of Nordaustlandet, whereas ours is on BE and our Nordaustlandet anomaly lies rather around +16/17 °C, compared to +21 °C in Day et al. (2012) using HadRM3 (Hadley regional climate model). This is probably due to the fact that MIROC5 overestimates the present sea ice extent and still has up to 40 % of sea ice cover on the east coast of Nordaustlandet over the period 2070–2099 (Fig. 3.10), whereas HadGEM1 (Hadley Centre Global Environmental Model; used as forcings in Day et al., 2012) ocean is mostly ice-free at the end of this century.

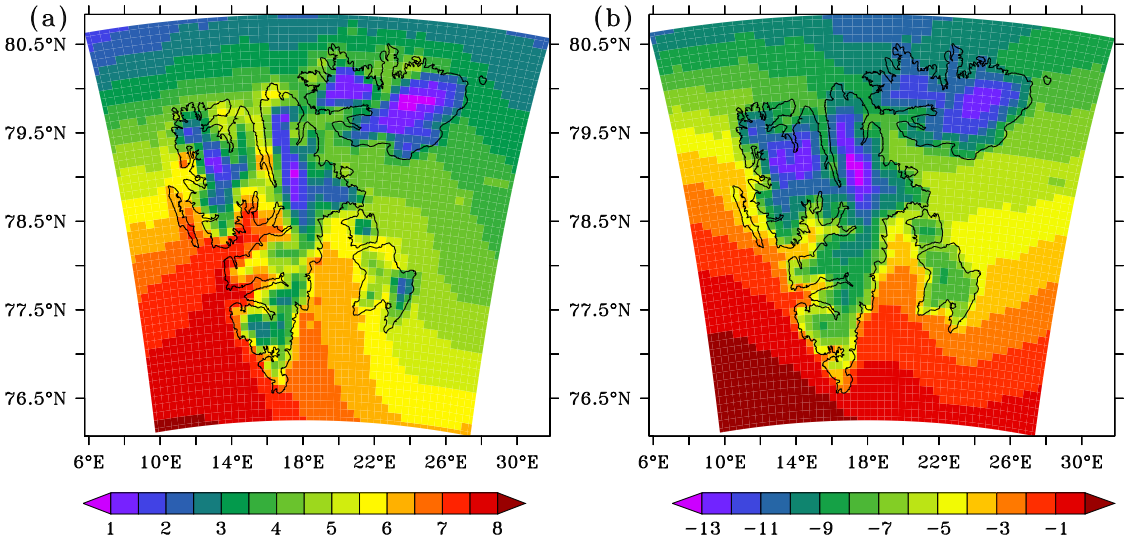

Figure 3.9: **(a)** 2070–2099 mean summer (JJA) near-surface temperature (°C). **(b)** Same as **(a)** but for winter (DJF).

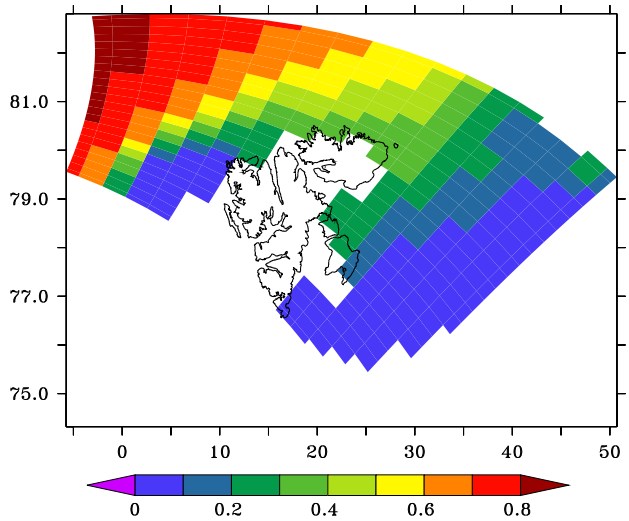

Figure 3.10: 2070–2099 mean winter (DJF) sea-ice cover from MIROC5.

3.4 Melt season

During the first half of this century, $MAR_{RCP8.5}$ projects that the beginning of the melt season (Fig. 3.11a) will not vary much (melt season will start 0.2 days earlier per year) because the effect of the temperature increase bringing more energy for the melt (Fig. 3.12a) will be compensated by the albedo effect (Fig. 3.12c) induced by increasing winter snowfall (Fig. 3.12b). As the amount of snowfall increases, so does the winter snowpack height above bare ice/old dirty snow at the beginning of the summer. The appearance of low albedo zones in summer is therefore delayed and SWnet (net shortwave radiation flux) available

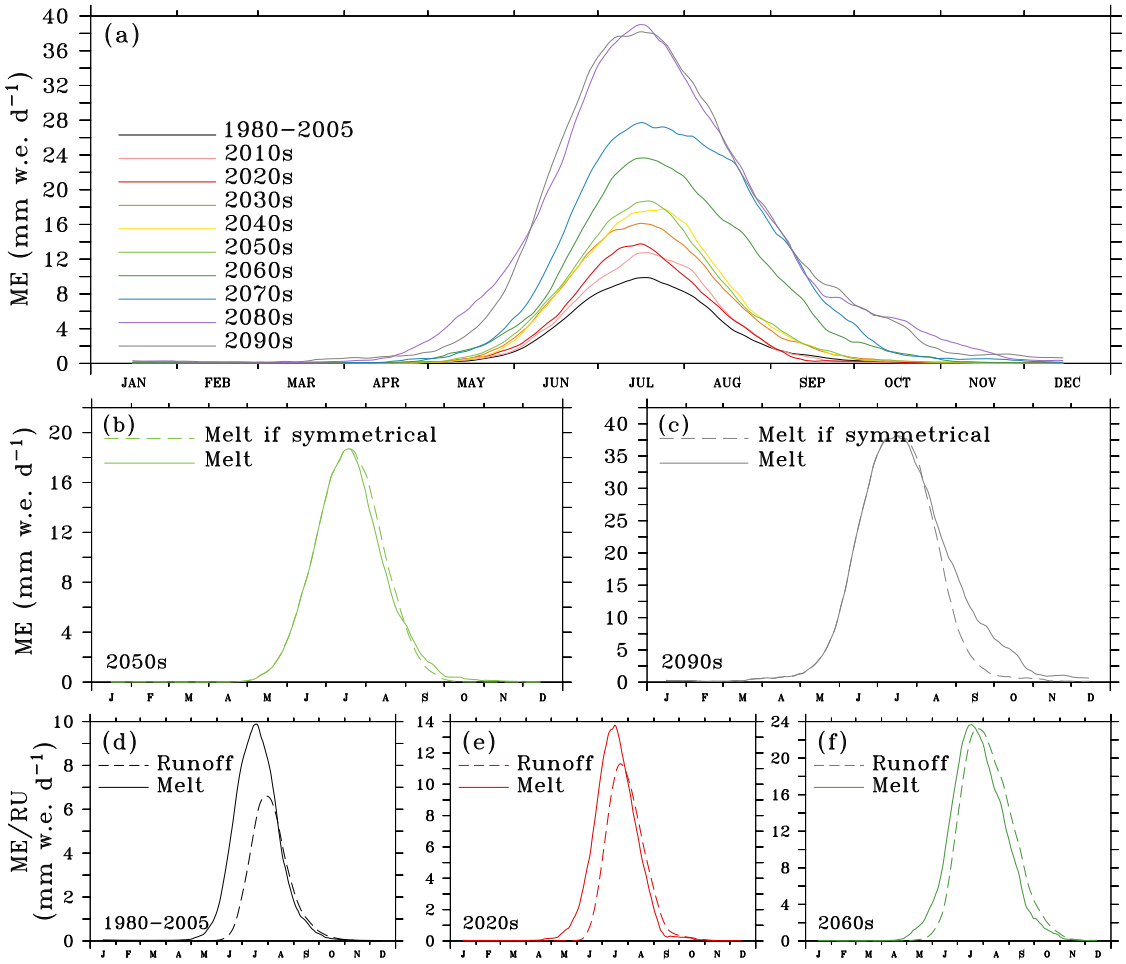

Figure 3.11: **(a)** Mean annual cycle of the surface melt (mm w.e. d^{-1}, 30-day running mean) for the listed decades. The 1980–2005 mean is shown in black as comparison. **(b)** Annual cycle of the surface melt in the 2050s (solid line) as well as, in dashed lines, the cycle if it were symmetrical with respect to its maximum. **(c)** Same as **(b)** but for the 2090s. **(d)** Mean annual cycle of melt (solid line) and runoff (dashed line) (mm w.e. d^{-1}) during the 1980–2005 period. **(e)** Same as **(d)** in the 2020s. **(f)** Same as **(d)** in the 2060s.

for the melt in the energy budget is reduced. After the 2050s, the temperature increase is projected to dominate the effect of heavier snowfall accumulation and the melt season is expected to start significantly sooner (1.5 days earlier per year).

The seasonal melt maximum happens around 15–20 July through the whole 21st century and coincides with the temperature maximum. Before 2050, the temperature seasonal cycle is more or less symmetrical with respect to its maximum value. The seasonal melt (albedo) cycle is also symmetrical with respect to its maximum (minimum) (Figs 3.11b and 3.12c). In the second half of the century, the temperature and therefore the melt are projected to increase more after their seasonal maximum than at the beginning of summer. The melt asymmetry is also partly explained by changing snowfall that is projected to increase before June

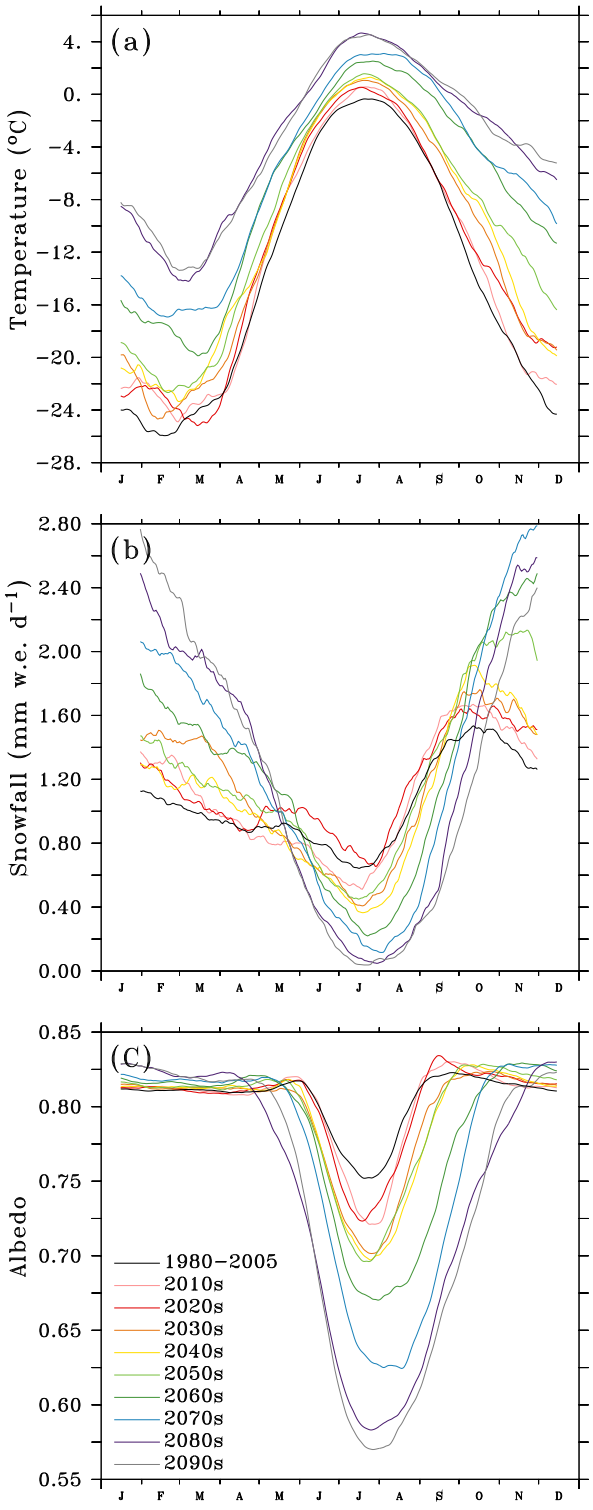

Figure 3.12: **(a)** Mean annual cycle of TAS (°C, 30-day running mean) over the permanent ice covered area for the listed decades. The 1980–2005 mean is given in black as comparison. **(b)** Same as **(a)** but for the snowfall (mm w.e. d^{-1}). As the daily variability of precipitation is very high, we have applied here a 60-day running mean instead of 30 days (like in Figs. 3.11 and 3.12a and c) in order to make the figure more clear. **(c)** Same as **(a)** but for the albedo.

but to significantly decrease in late summer, impacting the melt through positive albedo feedback.

As early as the 2030s, the $\mathrm{MAR}_{\mathrm{RCP8.5}}$ time of runoff maximum coincides with the time of melt maximum (Figs. 3.11d, e and f). The 5- to 8-day delay visible in Fig. 3.11d, e and f corresponds to the time needed in MAR for the meltwater to runoff from the glaciers to the sea as parametrised in Zuo and Oerlemans (1996). The runoff maximum is also projected to be equal to (or near to) the melt maximum. This agreement in time is due to the fact that, from the 2030s, at the time of the melt maximum, a smaller fraction of the melting area is covered with snow (retaining part of the meltwater and delaying the runoff) and large areas are covered with bare ice or impermeable snowpack (snow becomes impermeable when its density reaches 830 $\mathrm{kg\,m^{-3}}$ and prevents meltwater from percolating and refreezing) damping the meltwater retention capacity of the glaciers. During the historical period and up until the 2020s on the other hand, the presence of snow above ice in the ablation zone allows part of meltwater to be stored in the snowpack and refreeze in winter without running off. A rapid decrease of the refreezing capacity of the Greenland ice sheet and its buffering role in the future was also projected by van Angelen et al. (2013). Conversely, at the beginning of the melt season, there will still be a small delay between the melt and runoff seasons as the bare ice will be covered by the winter snowpack even at the end of the century. However, this delay will decrease steadily with time as the water storage and refreezing capacity will also decrease, as a consequence of the snow cover decrease in the enlarging ablation zone.

3.5 Energy balance

Studying energy balance components anomaly vs. temperature anomaly (rather than vs. time) offers the advantage that results do not depend on the choice of a particular future scenario, as shown by Fettweis et al. (2013a).

The net energy available at the surface for the melt (NET) can be calculated as follows:

$$\mathrm{NET} = \mathrm{SWnet} + \mathrm{LWnet} + \mathrm{SHF} + \mathrm{LHF} \quad (\mathrm{W\,m^{-2}}), \tag{3.1}$$

where

– $\mathrm{SWnet} = \mathrm{SWD} \times (1 - a)$ is the net shortwave radiation, i.e. the amount of the

downward shortwave (solar radiation) energy flux (SWD) that is absorbed by the surface following its albedo (a).

– LWnet = LWD − LWU is the net long-wave radiation, i.e. the difference between the downward long-wave radiation coming from the atmosphere (LWD) and the upward long-wave radiation emitted by the surface (LWU).

– SHF and LHF are the sensible and latent heat fluxes.

Two other net shortwave radiation fluxes have also been estimated (Fig. 3.13c and Table 3.1) in order to distinguish between the effects of the albedo change and the solar radiation change alone on SWnet, as done in Franco et al. (2013):

– $\mathrm{SWalb} = \mathrm{SWD}_{\mathrm{ave}} \times (1-\mathrm{a})$

– $\mathrm{SWswd} = \mathrm{SWD} \times (1-\mathrm{a}_{\mathrm{ave}})$

where the subscript "ave" denotes the 1980–2005 mean value. SWalb represents the effect of the varying albedo alone on SWnet and has been computed by keeping constant the amount of solar radiation reaching the surface (1980–2005 mean value of SWD) and allowing the albedo to vary throughout the investigated period (1980–2100). SWswd, on the other hand, represents the effect of the varying amount of solar radiation alone at the surface and has been computed by keeping the albedo constant and allowing SWD to vary (1980–2100).

In summer, the snowpack melts and the subsurface heat flux is therefore negligible. In the future, it will become even more negligible as larger and larger parts of the glaciated area will start melting and most of the snowpack will have a temperature of 0 °C. We therefore do not take this flux into account in the energy balance equation.

Figure 3.13b shows that the JJA net energy flux at the surface (and therefore melt and runoff, Fig. 3.13a) quadratically increase with the JJA TAS projected changes, as also projected over Greenland (Franco et al., 2013). Figure 3.13c shows the evolution of the anomaly of each energy balance component (JJA) as a function of the $\mathrm{TAS}_{\mathrm{JJA}}$ anomaly.

$\mathrm{MAR}_{\mathrm{RCP8.5}}$ predicts that, at the end of the century (2080–2099 mean), the anomaly of SWnet will represent 33 % of the NET anomaly, while the SWalb anomaly, reflecting the effect of the albedo on SWnet, will account for 50 % of the NET anomaly (Table 3.1). The expected increase in cloud optical depth will

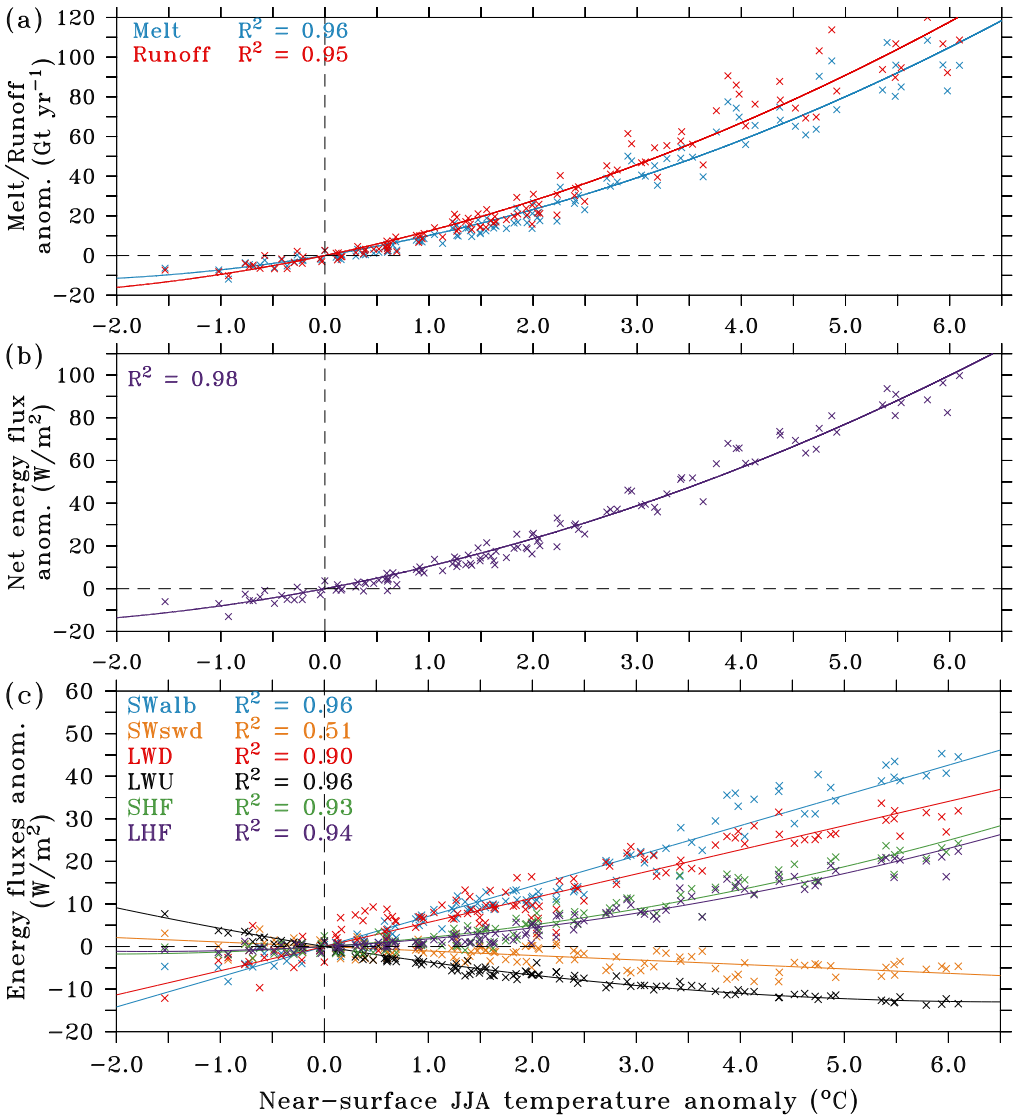

Figure 3.13: **(a)** Melt and runoff anomalies ($\mathrm{Gt\,yr^{-1}}$) vs. $\mathrm{TAS_{JJA}}$ anomaly (°C). The anomalies are differences with respect to the 1980–2005 mean. **(b)** Same as **(a)** but for the JJA net energy flux at the surface ($\mathrm{W\,m^{-2}}$). **(c)** Same as **(a)** but for the JJA energy balance components. The solid lines are quadratic regression curves.

decrease the incident solar radiation at the surface (Fig. 3.13c), and it partly compensates for the increase of SWalb associated with the decreasing albedo, leading to a positive and increasing SWnet, as also projected over Greenland (Franco et al., 2013).

The second contribution to the NET increase is the sensible heat flux, whose anomaly at the end of the century is projected to represent 24 % of the NET anomaly, as a consequence of the advection of warmer (oceanic) air over the cold ice/snow surface. At present, the modelled TAS is negative on average in summer and therefore lower than the snow/ice temperature (0 °C as the surface snow/ice is

Table 3.1: Anomaly of the energy balance components ($W\,m^{-2}$) and relative contribution of the energy balance components to the NET anomaly (2080–2099 mean compared to the historical period).

Energy balance component	Anomaly ($W\,m^{-2}$)	% of NET anomaly
SWnet	25	33
SWalb	38	49
SWswd	−6	−7.5
SHF	19	24
LHF	17	22
LWnet	16	21
NET	77	

melting). SHF is thus also negative and the surface loses energy to the atmosphere. $MAR_{RCP8.5}$ predicts that, around 2030, the summer near-surface temperature will become positive and consequently higher than the melting snow/ice temperature. The JJA SHF averaged over the entire Svalbard will also become positive.

The third contribution to the NET change is the latent heat flux, counting for 22 % over Svalbard, whereas it is the smallest contributor of the energy fluxes over Greenland (Franco et al., 2013). LHF is currently negative as evaporation and sublimation, requiring energy, are the dominant processes, but they will decrease in the future in favour of condensation and deposition (giving energy to the surface) as more and more humid and warm air due to the reduction of sea ice during summer will be advected towards the cold ice surface. On the other hand, condensation and deposition will also directly contribute to accumulation (10 % of the mean 2080–2099 accumulation) and act to oppose mass loss. In contrast to the Greenland ice sheet (Noël et al., 2014), which is higher in altitude, the oceanic conditions around Svalbard have a larger impact on its climate. In Svalbard, the katabatic winds, weaker than in Greenland, can not prevent the warm oceanic air from penetrating up to the central regions, and the SHF and LHF increase will take place over the entire land area instead of along the ice sheet margins as in Greenland (Franco et al., 2013).

Finally, the weakest contribution will come from the net long-wave radiation flux (LWnet, 21 % of the 2080–2099 NET anomaly). The increase in long-wave radiation emitted downward by the warmer and wetter atmosphere following the increase of the greenhouse gases concentration will partly be counterbalanced by the increase in upward long-wave radiation emitted by the surface, due to the

surface temperature increase.

3.6 Chapter conclusion

Over the 21st century, according to $MAR_{RCP8.5}$, the warming induced SMB decrease will be amplified by the snow/ice albedo feedback related to the extension of the ablation area that will increase the net shortwave radiation absorbed by the surface (and thus increase the energy available for the melt) and will decrease the meltwater retention capacity. The projected rapid decrease of the albedo will cause an acceleration of mass loss around 2050. $MAR_{RCP8.5}$ simulates a larger acceleration of mass loss in the south of the archipelago compared to the north. This regional difference is due to a larger increase of JJA SWnet in the south, related to the larger decrease of the JJA surface albedo. SWnet is the component of the energy balance the most sensitive to an increase in temperature because of the decreasing surface albedo. However, the downward shortwave radiation itself also decreases with increasing temperature due to an increase in cloud optical depth which partly counterbalances the effect of the melt–albedo positive feedback.

The summer sensible and latent heat fluxes are both negative at present but will increase with increasing temperature and become positive in the future, thereby heating the surface. The LHF increase will be caused by the decreasing SIC allowing for more evaporation around Svalbard and warmer and more humid air to be advected over the cold ice surface, showing the significant impact of the oceanic conditions on Svalbard, even far inland. The SHF will become positive when the temperature of the warmer oceanic air advected over the cold ice/snow surface will become positive, causing the atmosphere to give energy to the surface.

The temperature is projected to increase more in winter than in summer as (i) the surface temperature is limited to 0 °C, damping the temperature increase in summer and (ii) sea ice retreat is higher in winter than in summer since a large part of the ocean surrounding Svalbard is already ice free in the current climate (Day et al., 2012; Førland et al., 2011). Because of the larger present sea ice cover east of the archipelago than west of it, the winter temperature increase will be larger in the east than in the west.

All glaciated areas of the archipelago are projected to undergo net ablation by the end of the century. The disappearance of the accumulation zone is projected to happen much earlier in the south and northwest of Spitsbergen

than in the northeast and on the ice caps. However, even in these regions, the accumulation area is projected to completely disappear by the end of the century. The contribution of Svalbard 21st century SMB changes to sea level rise under the RCP8.5 scenario will be about 7.1 mm, according to MIROC5-forced MAR.

The increase of snowfall accumulation during winter and spring and the small increase in temperature at the beginning of the melt season explain why, during the first half of this century, the melt season is not expected to start much earlier than now, as the low albedo zones will be covered by a thicker winter snowpack. However, as the melt area is projected to be no longer covered with melting snow but rather with bare ice at the time of the melt maximum as early as the 2030s, the meltwater retention and refreezing capacity of the ice sheet will decrease greatly, and the runoff maximum will be equal in magnitude to the melt maximum and there will not be any delay between them.

Finally, it should be noted that the ice caps topography is fixed during our simulation, suggesting that we underestimate the surface mass loss in our projection as glacier thinning is not taken into account. On the other hand, our ice sheet mask is also fixed, suggesting that our projected integrated surface melt includes ice areas that will disappear in the near future and therefore that we overestimate the contribution of Svalbard to the sea level rise. This drives the necessity of coupling MAR with an ice sheet model in further developments to evaluate if not taking into account the glaciers thinning is counterbalanced by the use of a fixed permanent ice mask or not. In addition, a 10 km resolution results in an underestimation of the topography over most of the archipelago and an increased melt. Future projections at higher resolution (~ 5 km) are therefore required to better resolve the altitude of small glaciers.

CHAPTER 4

Very high resolution SMB over Svalbard with the regional climate model MAR coupled with an online downscaling technique

We established in Chapter 2 that, because of the very hilly topography of Spitsbergen, the largest island of the Svalbard archipelago, a spatial resolution of 10 km was not enough to resolve the complexity of the surface mass balance pattern and higher resolution simulations were needed. Regional climate models fully coupled to an energy balance model like MAR are ideal tools for the modelling of the surface mass balance, as they allow high spatial resolution simulations and can be calibrated for a specific region/climate. However, this kind of models explicitly solving the energy balance requires a huge amount of computation time. Moreover, MAR uses the hydrostatic equilibrium approximation, which becomes less valid when the spatial resolution is higher than 5 km. It is therefore not possible to achieve ∼1km resolutions with the current version of MAR. That is why we have implemented an online downscaling technique into MARv3.5, in which the surface module SISVAT runs at a resolution twice as high (3.75 km here) as the atmospheric module (7.5 km) allowing to explicitly simulate SMB at resolutions higher than 5 km. Section 4.1 describes the developments made in the model while Sect. 4.3 evaluates it and compares the outputs to a "classic" MAR simulation. Finally, we present the SMB simulations over the period 1960 – 2014 in Sect. 4.4 before we conclude in Sect. 4.5.

The content of this chapter will be submitted in *The Cryosphere*.

4.1 Model and forcings

4.1.1 Model

In the current version of MAR, the ice mask is fractional, i.e. a certain proportion (0–100 %) of each pixel is covered with permanent ice and the rest of the pixel is covered with tundra. Each pixel is therefore made of 2 sub-cells, one for ice and one for tundra, which do not represent distinct regions of the pixel but simply the fraction of the pixel covered by permanent ice and tundra. The SISVAT variables whose values depend on whether the ground is covered by ice or tundra (e.g. the amount of solar radiation absorbed by the surface depends on the albedo) are computed separately on both sub-cells and the inputs from SISVAT to the atmospheric module (e.g. surface fluxes, surface temperature) are

weighted mean values over the pixel, calculated according to the fraction of the pixel covered by both land covers.

With our downscaling technique, two different grids are needed: one for atmospheric variables (hereafter low resolution grid) and the other one, at a resolution twice as high, for SISVAT variables (hereafter high resolution grid). Those two grids are superimposable as the high resolution grid is constructed in such a way that 4 pixels make the four quadrants of one pixel in the low resolution grid (hereafter called "the 4 sub-pixel" of a MAR pixel). The elevation of a pixel in the low resolution grid is equal to the mean elevation of its 4 sub-pixels in the high resolution grid. The fractional ice mask, for its part, is constructed on the high resolution grid. In this version of MAR, each pixel is not made of 2 sub-cells but 5. The first 4 represent the permanent ice covering the 4 sub-pixels from the high resolution grid and the fifth one represents the tundra covered part covering all 4 sub-pixels. The 4 permanent ice sub-cells have their own elevation and ice fraction while the elevation of the tundra sub-cell is the elevation of the corresponding pixel in the low resolution grid, i.e. the mean elevation of the 4 sub-pixels in the high resolution grid.

At each MAR time step, near-surface temperature and specific humidity are corrected on the sub-grid, as a function of the elevation difference between the sub-pixels and the main atmospheric pixel (see Sect. 4.1.2) and local vertical gradients calculated on the low resolution grid, as in Franco et al. (2012).

As usually, the SISVAT variables computed for each sub-cells are averaged after the SISVAT call in MAR on the low resolution grid, except that there are now 5 sub-cells in the weighted average instead of 2. This method allows to model the surface mass balance at a resolution twice as high with only 20 % additional computation time whereas a classic simulation at a resolution twice as high would require at least 8 times more computation time.

Only near-surface temperature and specific humidity are corrected and precipitation are not. As mentioned by Giorgi et al. (2003), the correlation between precipitation and topography is not straightforward. Indeed, precipitation does not depend only on the local topography but also on the topography present upstream of the air mass bringing the humidity. If a high elevation region is not represented in the low resolution topography, orographic precipitation may occur somewhere else and there will be a precipitation bias in both regions. As there are more precipitation uncertainties (Sect. 4.3.1) in MAR than for temperature, correcting precipitation would add even more uncertainty. Precipitation correction

will therefore be dealt with in future developments and the amount of precipitation on the 4 sub-pixels is simply equal to the amount occurring on the atmospheric pixel they come from.

4.1.2 Temperature and humidity correction technique

Near-surface temperature and specific humidity are extrapolated from the low resolution grid to the higher resolution grid as follows (Fig. 4.1).

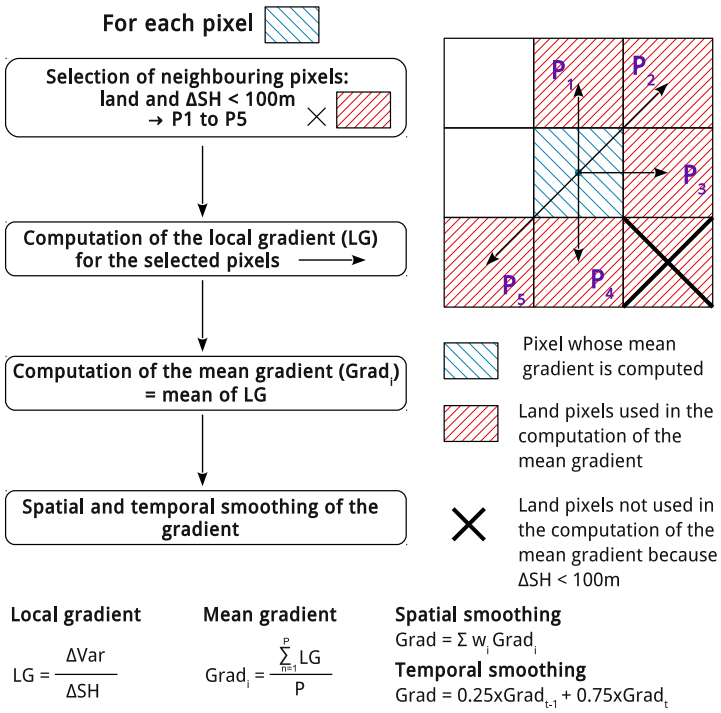

Figure 4.1: Computation of the near-surface temperature and humidity gradients.

First, for each land pixel of the low resolution grid, we calculate the local temperature/humidity gradient versus elevation between the pixel and each one of its 8 neighbouring pixels, provided that they are land pixels and that the elevation differences are larger than 100 m (to avoid infinite or aberrant gradients). Some pixels can therefore have zero neighbours satisfying those criteria (grey hatched areas in Fig. 4.6) and the temperature of these pixels is in this case not extrapolated over their 4 sub-pixels, as no temperature gradient is computed. Finally, a mean gradient is computed by averaging the 8 local gradients and a spatial and temporal smoothing is applied in order to remove aberrant values. For the spatial smoothing, the central pixel has a weight of 4, the "side" pixels have a weight of 2 and the

"diagonal" pixels have a weight of 1. The temporal smoothing is done such as the previous time step gradient counts for 25 % and the gradient of the current time step counts for 75 %. Note that, as the tundra covered sub-cell elevation is the elevation of the low resolution grid pixel, its temperature and humidity are therefore not corrected.

4.1.3 Forcings and simulations

The lateral (temperature, wind and specific humidity at each vertical level) and oceanic (sea surface temperature and sea-ice cover) boundaries of our integration domain were forced every 6h by the ECMWF reanalysis (ERA-40 over 1960–1978 and ERA-Interim over 1979–2014). We have run two different simulations. The first one, at a resolution of 7.5km ($MAR_{7.5km}$), uses the same version of MAR as Chapter 2 and 3. The second one uses the online downscaling technique implemented in MAR by running the atmosphere at a resolution of 7.5 km and SISVAT at a resolution of 3.75km ($MAR_{3.75km}$). The same MAR physics (version 3.5) is used in both simulations.

4.2 Topography and ice mask

Our 7.5 and 3.75 km resolution topographies and ice masks (Figs4.2a–d) were interpolated from the Norsk Polarinstituut topography and the ice mask from Nuth et al. (2013) as in Chapter 2. We consider pixels as permanent ice pixels if their surface is covered by more than 50 % of ice. Otherwise, the land pixels are considered to be tundra pixels. When we compute integrated values over the permanent ice area, we only consider pixels that are covered by more than 50 % of ice and values are weighted by the ice area of each pixel. As a result, we do not consider in our integrated values 8.6 % of the ice area in the 7.5 km run and 6.9 % in the 3.5 km run, corresponding to the pixels with ice covering less than 50 % of their surface. The area of the considered permanent ice is 30 071 km^2 in the 7.5 km grid and 30 663 km^2 in the 3.75 km grid.

Compared to the previously used 10 km topography, the 7.5 km elevation distribution (Fig. 4.3), represented by the histogram of elevations classes listed in Table 4.1, is much closer to the reference distribution coming from the 250 m topography and the 3.75 km topography improves furthermore the elevation distribution: the RMSE is smaller and the mean elevation and standard deviation

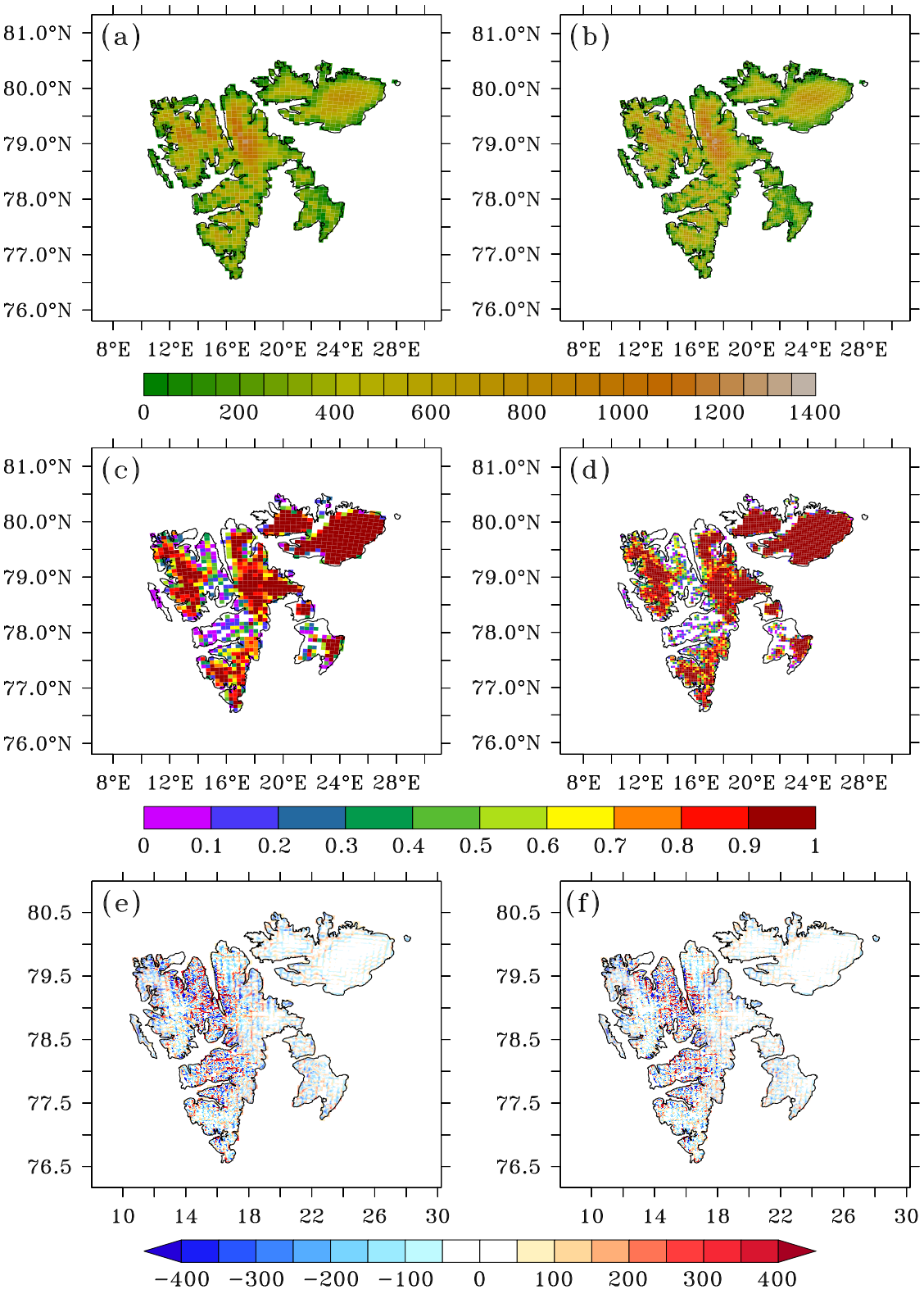

Figure 4.2: 7.5 and 3.75 km topographies ((**a**) and (**c**)), ice masks ((**c**) and (**d**)) and elevation difference with respect to the 250 m topography ((**e**) and (**f**)).

are closer to the 250 m topography values (Table 4.2). At 10 km, classes above class 11 (elevation ≥1100 m) were absent whereas the elevation goes up to class 13 in the 7.5 km topography (maximum elevation of 1282 m) and class 14 in the 3.75 km topography (maximum elevation of 1304 m). Below 300 m (classes 1–3), the elevation is overestimated on average in both the 7.5 and 3.75 km topographies, while it is underestimated above 300 m.

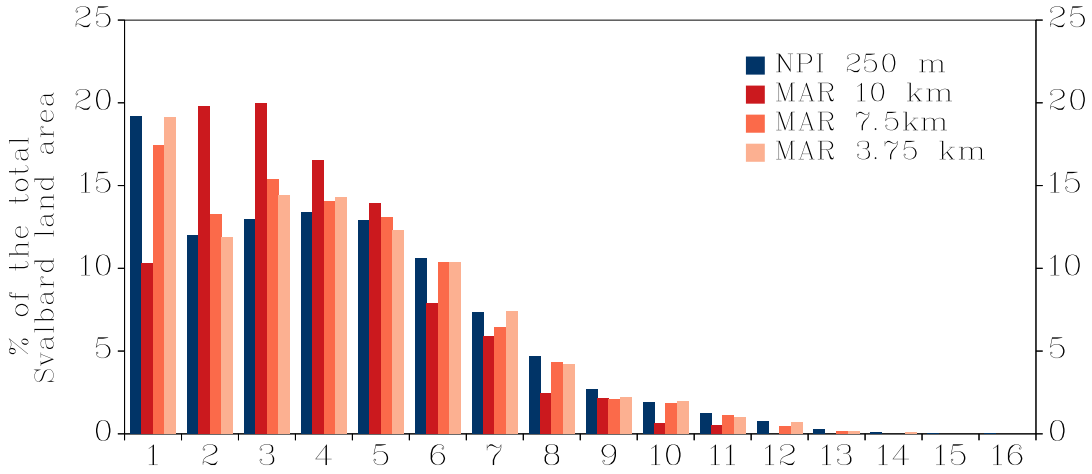

Figure 4.3: Histogram of the 16 elevation classes defined in Table 4.1, in percentage of the total area of Svalbard for the Norsk Polarinstitutt topography interpolated on a 25 m grid and the 10, 7.5 and 3.75 km topographies as used in MAR.

Table 4.1: Percentage of the total land area covered by each elevation class, mean absolute error (MAE, m) between the elevation in the 10/7.5/3.75 km grids and the 250 m grid, percentage of the area with underestimated elevation in the 10/7.5/3.75 km grids compared to the 250 m grid.

Class	Alt range (m)	% of total land area	MAE (m)			% of area with underestimated elevation		
			10 km	7.5 km	3.75 km	10 km	7.5 km	3.75 km
1	]0,100]	19	115	86	66	31	37	42
2	]100,200]	12	104	101	85	40	41	43
3	]200,300]	13	109	97	84	55	47	47
4	]300,400]	13	115	101	86	69	55	52
5	]400,500]	13	129	102	87	78	60	58
6	]500,600]	11	140	102	86	83	63	59
7	]600,700]	7	151	112	95	84	63	59
8	]700,800]	5	183	133	110	89	70	67
9	]800,900]	3	220	166	138	89	68	68
10	]900,1000]	2	224	152	129	92	70	67
11	]1000,1100]	1	258	160	134	98	79	71
12	]1100,1200]	1	319	176	142	100	82	77
13	]1200,1300]	0.3	378	216	177	100	93	87
14	]1300,1400]	0.09	404	244	202	100	100	99
15	]1400,1500]	0.03	479	312	276	100	100	100
16	>1500	0.01	586	397	345	100	100	100

However, despite the improvements brought by the use of the 7.5 and 3.75 km

topographies, elevation differences with respect to the 250 m topography can still be huge (≥400m) on Spitsbergen, even at 3.75 km (Figs 4.2e and f). Averaged over the whole domain, the error of the 3.5 km topography is 135 m (Table 4.2).

Table 4.2: Mean elevation (m) and standard deviation (m) in the 250 m, 10 km, 7.5 km and 3.75 km topographies. Root mean square error (RMSE, m) of the 10 km, 7.5 km and 3.75 km topographies compared to the 250 m topography.

Topography	Mean elevation (m)	Standard deviation (m)	RMSE (m)
250 m	371	268	–
10 km	327	219	175
7.5 km	360	254	151
3.75 km	364	261	135

4.3 Evaluation

As validation of MAR, we have compared the outputs of $MAR_{7.5km}$ and $MAR_{3.75km}$ to near-surface temperature, precipitation and SMB observations, as well as to the outputs of MAR at 10km forced by ERA-Interim from Chapter 2 (hereafter called MAR_{10km}).

4.3.1 Temperature

We have compared the $MAR_{7.5km}$ and $MAR_{3.75km}$ near-surface temperature and precipitation to observations from 5 stations from the Norwegian weather stations network (Fig. 2.2 and Table 4.3). $MAR_{7.5km}$ and $MAR_{3.75km}$ were both forced by the ERA-Interim reanalysis and, as we wanted to compare the outputs to the MAR_{10km} outputs, the period over which we evaluated MAR is 1979–2013.

Table 4.3: Stations used for validation. Coordinates of the stations, period over which data are available, elevation (m) of the stations and the nearest land pixel in the 7.5 km topography and distance between the station and the pixel (km).

Station	Coordinates		Period of observation		Elevation(m)		Dist station
			Temperature	Precipitation	Station	MAR	-pixel(km)
Ny-Ålesund	78.92° N	11.93° E	1979–2013	1979–2013	8	40	3.4
Svalbard Airport	78.25° N	15.50° E	1979–2013	1979–2013	28	32	6.8
Sveagruva	77.88° N	16.72° E	1979–2013	1979–2002	9	270	5.9
Hornsund	77.00° N	15.54° E	2005–2013	1996–2013	10	26	2.5
Kapp Heuglin	78.25° N	22.82° E	2006–2013	–	14	41	6.3

First, as the atmospheric variables of $MAR_{3.75km}$ are computed on the lower resolution grid, the $MAR_{3.75km}$ results are the same as the $MAR_{7.5km}$ results (Figs 4.4a 4.4b, and 4.5).

Table 4.4: Annual and summer correlation (R), bias (°C), centred RMSE (RMSEc, °C) and RMSE (°C) averaged for all stations for MAR_{10km}, $MAR_{7.5km}$ and $MAR_{3.75km}$.

	Annual				Summer			
	R	Bias (°C)	RMSEc (°C)	RMSE(°C)	R	Bias (°C)	RMSEc (°C)	RMSE(°C)
MAR_{10km}	0.96	-2.70	2.7	3.8	0.79	-2.90	1.7	3.4
$MAR_{7.5km}$	0.96	-0.23	2.6	2.6	0.82	-0.34	1.8	1.8
$MAR_{3.75km}$	0.96	-0.22	2.6	2.6	0.82	-0.34	1.8	1.8

As for MAR_{10km}, the correlation between the daily $MAR_{7.5km}$ and $MAR_{3.75km}$ outputs and the observations is excellent at the annual time scale (R = 0.96- 0.97, Fig. 4.4a and Table 4.4) whereas the daily variability of near-surface temperature is less well represented (R = 0.7–0.9, Fig. 4.4b) if only the summer months (June–July–August, JJA) are considered but is better at 3.75 km than at 10 km. The root mean square error (RMSE) is smaller for $MAR_{3.75km}$ than for MAR_{10km} at every station, both annually and in summer because the biases are strongly reduced in $MAR_{3.75km}$ compared to MAR_{10km}. The centred RMSE (RMSEc), representing the mean error without considering the effect of biases, is however slightly larger for $MAR_{7.5km}$ and $MAR_{3.75km}$ than for MAR_{10km} at all stations in summer (Fig. 4.4b) and all stations but Svalbard Airport and Sveagruva at the annual time scale (Fig. 4.4a), because the standard deviation of MAR_{10km} is closer to the standard deviation of the observations than $MAR_{3.75km}$ at the aforementioned stations. The biases between the model and the observations are largely reduced (Fig. 4.5, Table 4.4) and become lower than 1 °C for most of the stations at the annual and summer time scale. In summer, the only station for which the temperature bias remains quite large is Sveagruva (mean cold bias of -1.5 °C) because, even at a 7.5 km resolution, the topography around the station is highly overestimated (Table 4.3). However, $MAR_{7.5km}$ and $MAR_{3.75km}$ show much better agreement with the observations than MAR_{10km} at Sveagruva. At Kapp Heuglin, the elevation of the pixel was already close to the station elevation in the 10 km topography and $MAR_{7.5km}$ and $MAR_{3.75km}$ therefore do not improve the results. The large winter bias at Hornsund and Kapp Heuglin come from a bug in the MAR code, that has been corrected in MARv3.6. In MARv3.5, the sea ice temperature is highly underestimated and the near-surface temperature is therefore also underestimated. Finally, at Ny-Ålesund and Svalbard Airport, MAR now represents almost perfectly the near-surface temperature annual cycle.

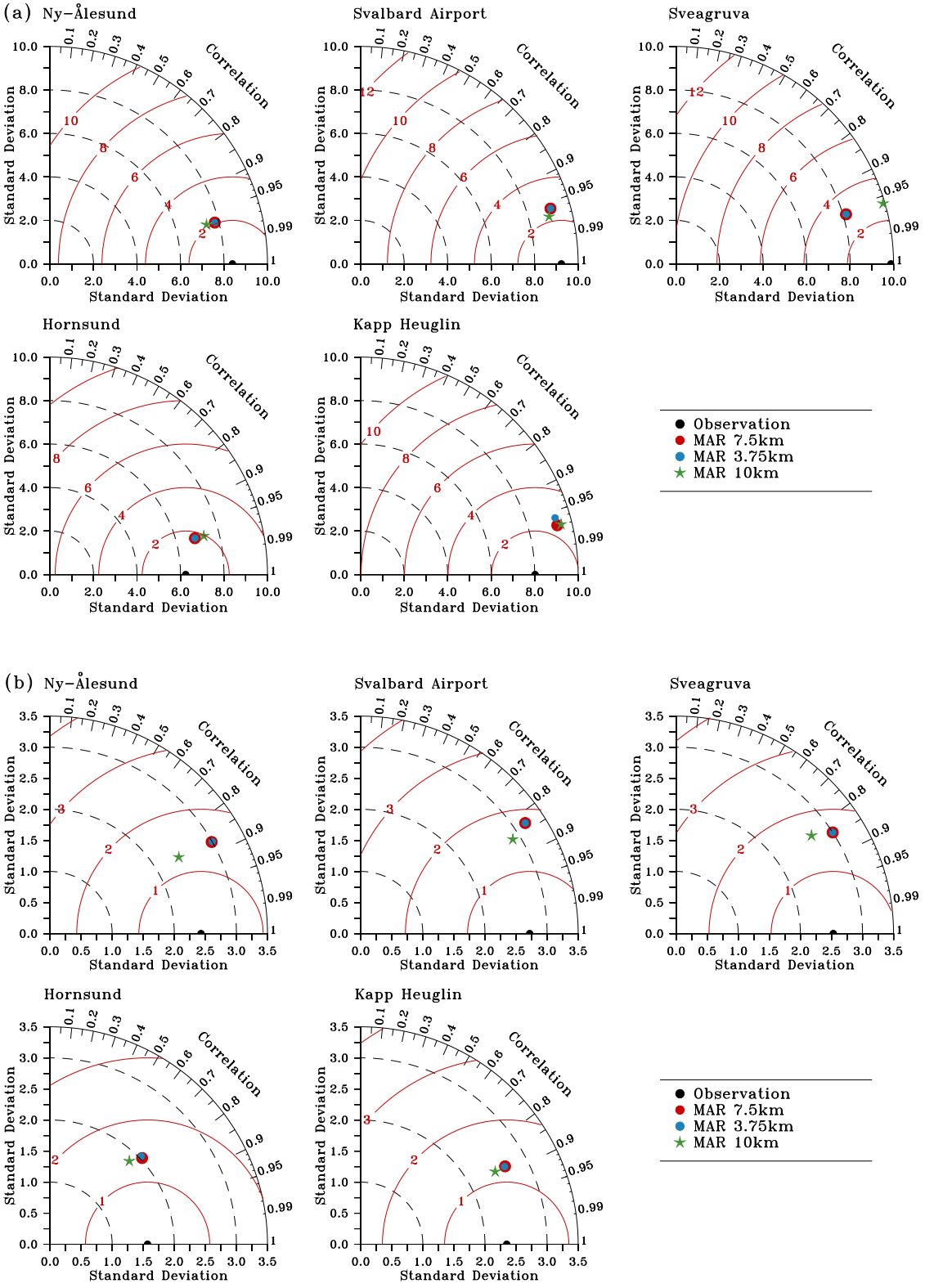

Figure 4.4: **(a)** Taylor diagram of the MAR daily near-surface temperature outputs vs weather stations measurements for the 5 stations shown in Fig. 2.2. **(b)** Same as **(a)** but for summer (June–July–August).

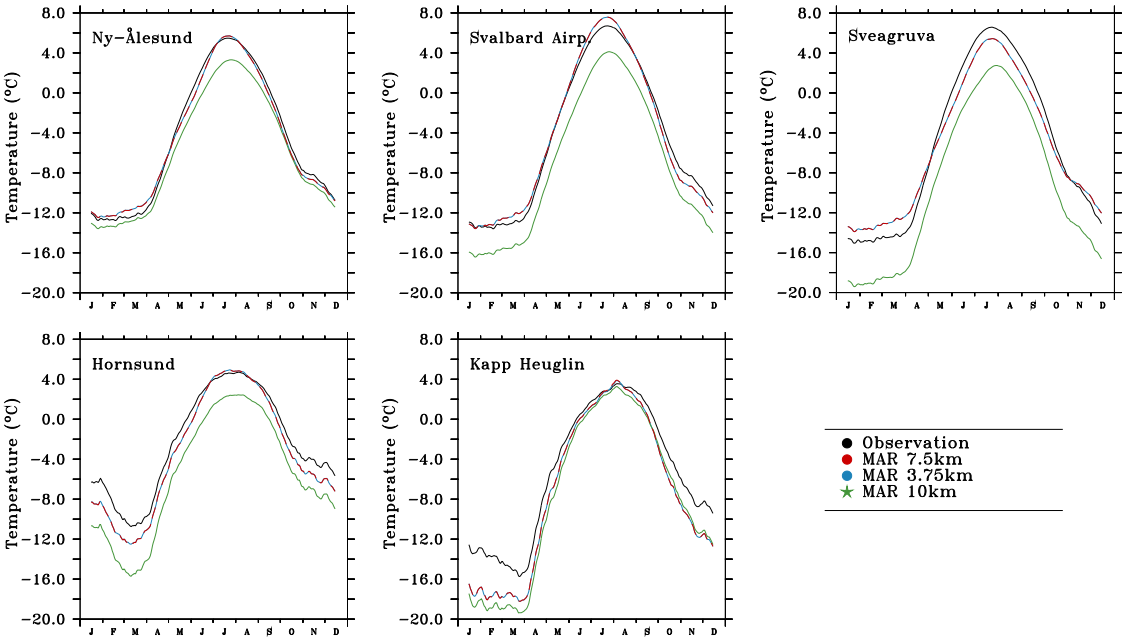

Figure 4.5: Annual cycle of the near-surface temperature from the different MAR simulations and the weather stations observations (black curves) for the 5 stations shown in Fig. 2.2, averaged over the period for which data were available (Table 4.3). A 30-day running mean has been applied.

For precipitation, the results are similar to MAR_{10km}: the mean annual amount is underestimated at Ny–Ålesund and overestimated at Hornsund, Svalbard Airport and Sveagruva (Table 4.5). The daily variability of precipitation is very poorly represented and MAR performs a little bit better at the annual timescale but the correlations are still rather low (R<0.35). As mentioned in Chapter 2, the precipitation pattern on Spitsbergen, where all the stations are located, is very complex and we can not resolve its spatial distribution at such resolutions. Finally, the large gaps in the precipitation time series at all stations makes the evaluation even more difficult.

Table 4.5: Percentage of missing observations (% MO), 1979–2013 mean annual measured precipitation ($mm\,yr^{-1}$), proportion of that precipitation that is simulated by $MAR_{7.5km}$ and $MAR_{3.75km}$, correlation (R) between the daily/annual measured and modelled precipitation.

Station	% MO	Pobs	Pmod/Pobs		R daily		R annual	
		($mm\,yr^{-1}$)	$MAR_{7.5km}$	$MAR_{3.75km}$	$MAR_{7.5km}$	$MAR_{3.75km}$	$MAR_{7.5km}$	$MAR_{3.75km}$
Ny-Ålesund	47	409	0.76	0.75	0.4	0.4	0.6	0.6
Svalbard Airport	39	187	1.93	1.92	0.3	0.3	0.0	0.0
Sveagruva	42	252	1.53	1.53	0.3	0.3	0.2	0.2
Hornsund	50	378	1.11	1.11	0.2	0.2	0.6	0.6

4.3.2 Surface mass balance

We have compared the $MAR_{7.5km}$ and $MAR_{3.75km}$ SMB outputs to the measurement of Pinglot et al. (1999, 2001) (Figs 4.6, 4.7 and Table 4.6). As the ice cores were retrieved in the accumulation area, precipitation is an important component of the SMB and the 7.5 km and 3.5 km outputs are comparable as our downscaling technique impacts mainly melt given that only near surface temperature and humidity are downscaled and precipitation is not.

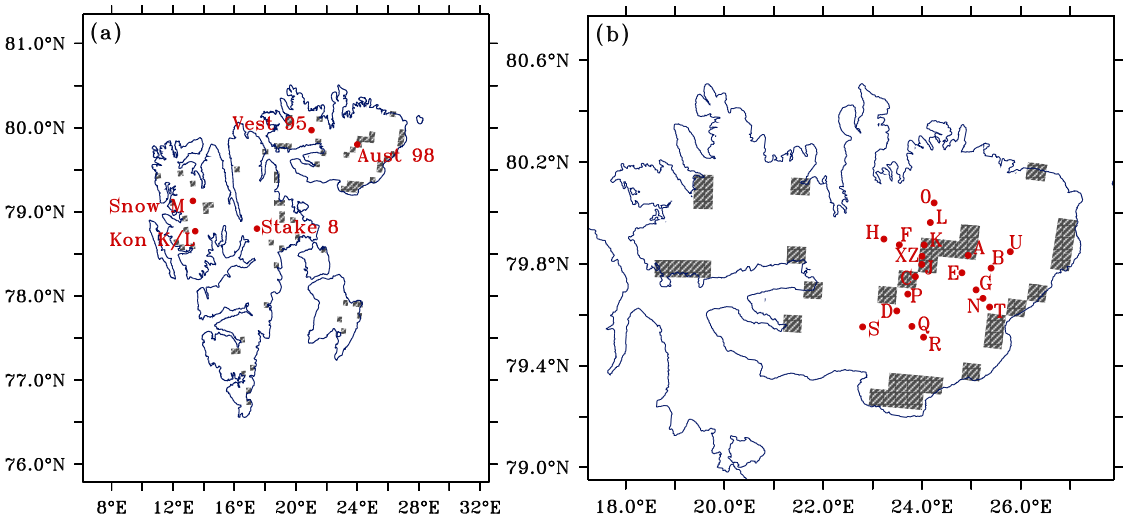

Figure 4.6: **(a)** Location of the stakes of Pinglot et al. (1999) used in the SMB validation. **(b)** Same as **(a)** but for Pinglot et al. (2001). The hatched areas correspond to the pixels with no temperature and humidity correction in $MAR_{3.75km}$ (Sect. 4.1.2).

On Spitsbergen, $MAR_{3.75km}$ performs better than $MAR_{7.5km}$ at Snow M, where the overestimation of the SMB is reduced, and at Stake 8, where it correctly simulates the accumulation (Table 4.6). At Kon L and Kon K, the results are similar for both runs: MAR performs well at Kon L (a little bit better at 3.75 km) whereas it underestimates the SMB a lot at Kon K. Even though the accumulation at Kon K is still highly underestimated, there is an improvement in $MAR_{3.75km}$ compared to MAR_{10km}. At the 10km resolution, Kongsvegen, with an area of approximatively 100 km^2 corresponds to one pixel only and the accumulation and ablation zones are not resolved. As a result, the SMB is an accumulation/ablation average and is largely underestimated for both stakes. At 7.5 and 3.75 km,the accumulation and ablation zones are better resolved and Kon L is almost in the accumulation range of Pinglot et al. (1999) while at Kon K, closer to the ablation zone, MAR underestimates the SMB a lot suggesting that a resolution of 3.75 km is not enough to resolve the SMB spatial variability in this area. On Austfonna and

Table 4.6: Elevation of the sites from Pinglot et al. (1999, 2001) used in the validation and of the closest $MAR_{7.5km}$ and $MAR_{3.75km}$ pixels, distance between the stakes and the closest pixel, minimum and maximum measured SMB ($m\,w.e.\,yr^{-1}$) from Pinglot et al. (1999, 2001) and simulated by $MAR_{7.5km}$ and $MAR_{3.75km}$. (1) For stakes O and T, only an average value was available. (2) The closest pixel is in the ablation zone.

Stake	Elevation (m)			Distance pixel -stake (m)		SMB Pinglot ($m\,w.e.\,yr^{-1}$)		SMB MAR ($m\,w.e.\,yr^{-1}$)	
	Stake	7.5 km	3.75 km	7.5 km	3.75 km	Min.	Max.	7.5 km	3.75 km
Snow M	1170	1125	1126	1.8	0.7	0.54	0.6	0.96	0.86
Kon K	639	591	593	2.3	0.7	0.45	0.52	0.11	-0.04[(2)]
			681		3.0				0.07
Kon L	726	825	842	3.9	1.1	0.57	0.67	0.55	0.56
Stake 8	1173	884	955	4.2	1.7	0.74	0.76	0.69	0.79
Vest 95	600	593	599	2.0	1.5	0.36	0.46	0.30	0.33
Aust 98	740	753	743	2.4	1.8	0.45	0.58	0.49	0.48
A	729	722	720	2.1	1.3	0.41	0.43	0.43	0.44
B	586	623	627	2.9	1.3	0.33	0.35	0.44	0.41
C	707	679	692	3.4	1.2	0.53	0.55	0.40	0.35
D	708	651	668	3.2	1.5	0.33	0.35	0.53	0.49
E	720	708	716	2.6	0.9	0.36	0.37	0.42	0.41
F	727	702	720	2.9	2.0	0.36	0.38	0.34	0.35
G	604	559	567	2.7	0.3	0.29	0.30	0.30	0.29
H	619	702	684	3.8	1.5	0.21	0.22	0.34	0.31
J	758	753	743	2.4	1.6	0.46	0.58	0.48	0.48
K	728	744	734	2.4	1.3	0.36	0.38	0.39	0.38
L	620	660	647	3.3	1.6	0.30	0.32	0.24	0.22
N	491	460	459	2.7	1.0	0.19	0.21	0.21	0.22
O	506	568	549	4.4	3.0	0.11[(1)]		0.17	0.18[(2)]
P	653	640	637	1.4	1.4	0.48	0.50	0.32	0.30
Q	613	536	559	4.3	1.8	0.28	0.30	0.38	0.35
R	511	532	517	2.4	0.5	0.21	0.24	0.37	0.30
S	651	606	624	1.4	1.6	0.34	0.35	0.48	0.49
T	360	293	427	3.5	2.4	0.00[(1)]		0.02	0.23[(2)]
U	619	619	619	2.5	0.3	0.21	0.24	0.42	0.44
X	783	753	764	4.2	1.5	0.45	0.46	0.44	0.43
Z	783	753	764	4.2	1.5	0.39	0.45	0.44	0.43

Vestfonna, $MAR_{3.75km}$ performs better for 9 stakes and $MAR_{7.5km}$ for 10 stakes but the simulated SMB is most of the time very similar for both runs, whether it be better represented at 3.75 or 7.5 km, showing that a resolution of 7.5 km is enough to represent the much smoother topography of Austfonna and Vestfonna. MAR performs very well for stakes A, F, G, J, K, N, Z and Aust 98. The X and Z ice cores were retrieved only a few hundred metres apart and correspond to the same

MAR pixel but their accumulation are significantly different, showing that, even on Austfonna, there can be substantial spatial SMB variations at a very local scale that MAR can not represent. Considering that and the fact that the closest pixel is often ∼1.5 km away from its associated stake, we can also consider that MAR performs very well at stakes E, X and Vest 95 ($MAR_{3.75km}$) and T ($MAR_{7.5km}$). If we compare the MAR accumulation pattern (Fig. 4.7) to Fig. 9 of Pinglot et al. (2001), we see that MAR performs well along the margins but underestimates the accumulation in the central parts of Austfonna: the accumulation is higher than 0.5 m w.e. yr^{-1} in Pinglot et al. (2001) whereas it reaches 0.51 for only one $MAR_{7.5km}$ pixel and 0.495 for $MAR_{3.75km}$. This is confirmed at stakes C, L, and P, for which the MAR SMB is quite underestimated.

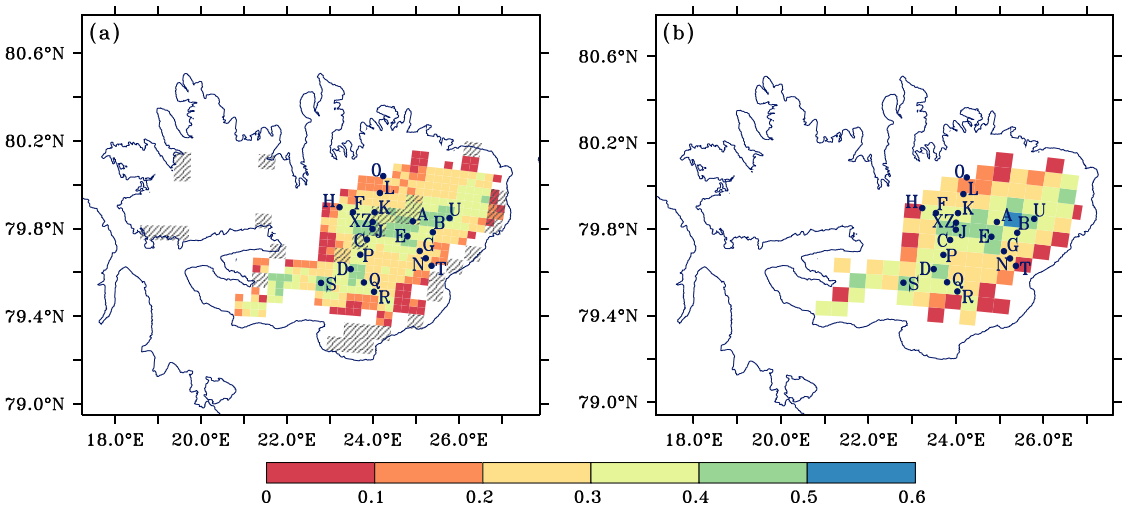

Figure 4.7: **(a)** 1986–1999 mean accumulation pattern of $MAR_{3.75km}$. The hatched areas correspond to the pixels with no temperature and humidity correction. **(b)** Same as **(a)** but for $MAR_{7.5km}$.

Stakes A, C, J, K, X and Z are located in pixels for which the SMB was not corrected because the elevation difference between the pixel and its 8 neighbours was smaller than 100 m (Sect. 4.1.2, hatched pixels in Fig. 4.6b). For these stakes, the modelled 3.75 km-SMB is therefore the 7.5 km-SMB. The elevation difference between the 7.5 km and the 250 m topographies is however small for those pixels (less than 50m). Moreover, stakes A, J, K and X give a very good estimation of the SMB, showing once more that a resolution of 7.5 km is enough to resolve the topography at the top of Austfonna and that the underestimation of accumulation at stakes C and Z can not be attributed to the use of a too low resolution. At Stakes D, S and U, MAR overestimate SMB a lot. Compared to the accumulation pattern of Pinglot et al. (2001), the accumulation area, and

especially the $0.2\,\mathrm{m\,w.e.\,yr^{-1}}$ isopleth, on which stake U is located in Pinglot et al. (2001), extends too far towards the northeast of the ice cap, explaining the overestimation of the modelled SMB at stake U. For stakes D and S, the MAR accumulation pattern shows a local overestimation with accumulation larger than $0.4\,\mathrm{m\,w.e.\,yr^{-1}}$ that is not present in Pinglot et al. (2001).

We can therefore conclude that, on Austfonna, where the topography is quite smooth, MAR performs well and a resolution of 7.5 km is enough whereas on Spitsbergen, our online downscaling technique improves the simulated SMB. It would however be better to increase the resolution even more, as there are still some large SMB biases on Spitsbergen.

4.4 Results

The SMB pattern and values are generally the same for $\mathrm{MAR_{7.5km}}$ and $\mathrm{MAR_{3.75km}}$ (Figs 4.8a and b) and the difference between the 2 runs is mainly the representation of the narrow ablation zones. For example, a zoom on south Spitsbergen (Figs 4.8c and d) shows that, at 3.75 km, we have 4 distinct accumulation zones separated by regions with negative SMB, whereas in $\mathrm{MAR_{7.5km}}$, those 4 regions are all connected and MAR is not able to resolve the narrow ablation zones present between them. On the east coast, there is also a region in the north of south Spitsbergen where the ablation zone, visible with $\mathrm{MAR_{3.75km}}$, is missing in $\mathrm{MAR_{7.5km}}$. Differences in integrated SMB values between $\mathrm{MAR_{7.5km}}$ and $\mathrm{MAR_{3.75km}}$ ($0.46\,\mathrm{Gt\,yr^{-1}}$ vs $-0.76\,\mathrm{Gt\,yr^{-1}}$) come from "transition" areas near the equilibrium line, i.e. from regions that go from accumulation to ablation zones, corresponding to regions with temperature close to 0 °C where we can go from positive to negative temperature after the correction. For those regions, due to the melt-albedo feedbacks, the SMB of a 7.5 km pixel is not equal to the mean SMB of its 4 sub-pixels whereas it is in regions that are not transition regions. From now on, we will therefore focus only on the 3.75 km simulation. The different permanent ice masks are also partly responsible for the differences in SMB values when integrated over the whole Svalbard. With the 3.75 km grid, we have about 600 more $\mathrm{km^2}$ than with the 7.5 km grid and those 600 $\mathrm{km^2}$ correspond to low altitude areas with largely negative SMB.

The 1960–2014 $\mathrm{MAR_{3.75km}}$ mean SMB is $-0.76 \pm 8.8\,\mathrm{Gt\,yr^{-1}}$, corresponding to $-25 \pm 288\,\mathrm{mm\,w.e.\,yr^{-1}}$ (Table 4.7). The 1979–2013 mean is $-83 \pm 294\,\mathrm{mm}$

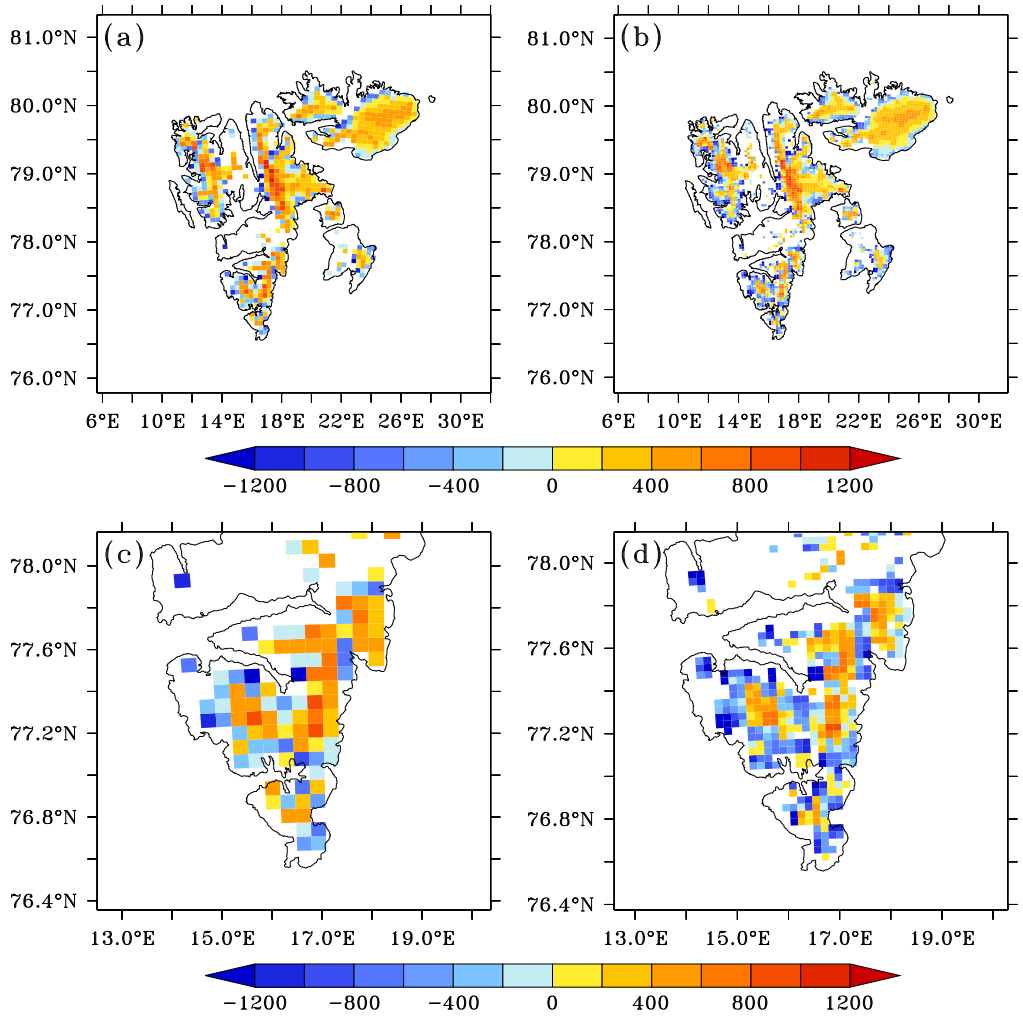

Figure 4.8: **(a)** 1960 – 2014 mean SMB (m w.e. yr^{-1}) for $MAR_{7.5km}$. **(b)** Same as **(a)** but for $MAR_{3.75km}$. **(c)** Same as **(a)** but with a zoom on south Spitsbergen. **(d)** Same as **(b)** but with a zoom on south Spitsbergen.

w.e. yr^{-1}, which is lower than the MAR_{10km} mean of -54 ± 236 mm w.e. yr^{-1}, for the reasons cited earlier.

Hagen et al. (2003b) have computed an integrated value of the Svalbard SMB of -14 ± 3 mm w.e. yr^{-1}, based on long term time series from measurements made on individual glaciers between the 1960s and the 1990s. Despite its positive value, our estimation of $+17$ mm w.e. yr^{-1} is in agreement with theirs, considering the large interannual variability (271 mm w.e. yr^{-1}) of the SMB and the fact that the estimation of Hagen et al. (2003b) is based on measurements that were carried out during different time periods while we considered here the period 1960–1999.

Over 1979–2013, the MAR_{10km} SMB was negative but its trend was not significant. The $MAR_{3.75km}$ SMB is also negative over 1979–2013 and its trend is not significant (Table 4.7).

Table 4.7: top panel: 1979–2013 MAR_{10km} and $MAR_{3.75km}$ mean SMB ($Gt\,yr^{-1}$) with interannual variability ($Gt\,yr^{-1}$) and trends with their uncertainty range ($Gt\,yr^{-2}$). Bottom panel: Same as top panel but for the 1960 – 2014 SMB and its components ($Gt\,yr^{-1}$) and annual and summer near-surface temperature (°C). The significant trends are in bold.

	Mean	Interannual variability ($Gt\,yr^{-1}$ – °C)	Trend	Uncertainty range ($Gt\,yr^{-2}$ – $°C\,yr^{-1}$)
		1979 – 2013		
MAR_{10km}	-1.6	7.1	-0.10	0.24
$MAR_{3.75km}$	-2.5	9.0	-0.09	0.30
		1960 – 2014		
SMB	-0.76	8.8	-0.13	0.15
RU	27.6	8.6	**0.17**	0.14
SU	-0.68	0.4	**-0.01**	0.00
ME	29.3	7.6	**0.16**	0.12
P	24.7	6.0	0.05	0.07
RF	6.9	1.8	**0.03**	0.03
SF	17.8	3.3	0.01	0.05
Tann	-10.9	1.5	**0.06**	0.02
Tsum	-0.67	0.6	**0.01**	0.01

Over 1960–2014, the SMB as modelled by $MAR_{3.75km}$ is still negative and the trends are still not significant: Svalbard is losing ice through surface processes every year on average but, according to MAR, there was no acceleration of the mass loss over the last 55 years (Fig. 9).

According to Snedecor and Cochran (1971), the trend is significant (here at the 95 % confidence interval) if it is larger than the uncertainty range. As shown in Table 4.7, the 1960–2014 trend is lower than the uncertainty range but the values are extremely close to each other, meaning that the statistical significance of the trend is debatable. The stability of the SMB over Svalbard with respect to other Arctic ice caps has been attributed to a recent change in the summer 700hPa atmospheric circulation between 2006 and 2012, with northwesterly fluxes over Svalbard instead of westerly fluxes (1979–2005 mean), causing colder than usual conditions (Fettweis et al. (2013b) and Chapter 2) and damping the warming observed in other Arctic regions. In 2013, there was a southwesterly flux bringing warmer air on Svalbard and causing an SMB record. In 2014, the circulation was again coming from the northwest instead of the west and the 2014 T850 anomaly with respect to the 1979–2005 mean was negative over Svalbard. The 2014 melt and runoff were therefore close to the average value and no SMB record was broken in 2014 ($-3.1\,Gt\,yr^{-1}$).

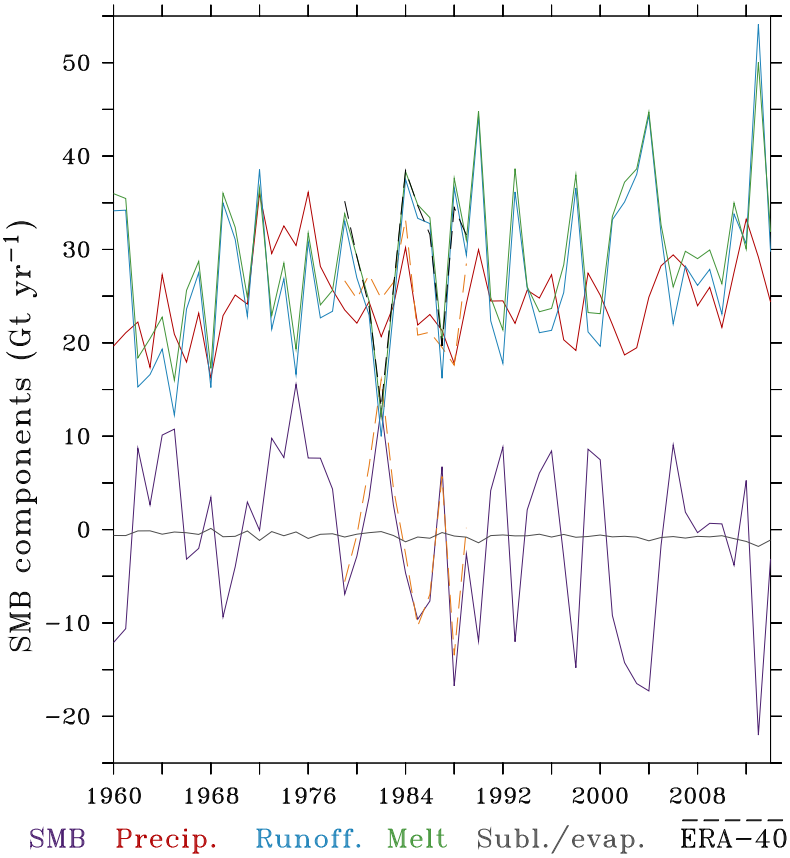

Figure 4.9: 1960 – 2014 evolution of the SMB, precipitation, melt, runoff and sublimation and evaporation (Gt yr^{-1}) integrated over the permanent ice area of Svalbard as simulated by MAR$_{3.75\text{km}}$. The dashed curves represents the SMB, melt and precipitation simulated by MAR forced by ERA-40 over 1979–1989.

On the contrary to the ERA-Interim era, runoff and melt have been significantly increasing over the last 55 years. The increase in runoff has been partly compensated by the significantly increasing deposition and non-significantly increasing precipitation, making the SMB trend non-significant. Snowfall, making the major part of precipitation, has remains stable over 1960–2014 while rainfall, counting for only 28 % of the total precipitation, has been significantly increasing due to the temperature increase changing part of the solid precipitation into liquid precipitation. The annual temperature has increased by 3.3 °C between 1960 and 2014 and the summer temperature by 0.6 °C and both trends are significant.

The net energy available for the melt in summer (NET, Chapters 2 and 3) has increased significantly over the period 1960–2014 (+8.9 W m^{-2} in 55 years, Fig. 4.10, Table 4.8), as a result of the increasing net shortwave radiation (SWnet, SWD remained stable while the albedo decreased significantly), downward longwave radiation (LWD) and sensible and latent heat fluxes (SHF and LHF).

The LWD and LHF trends are significant but SWnet and SHF are not. The upward longwave radiation (LWU) has also been significantly increasing towards more negative values (LWU takes energy from the surface), as a result of the surface temperature increase, and compensates a little the increase in LWD ($+4.9\,\mathrm{W\,m^{-2}}$ for LWD vs $-2.4\,\mathrm{W\,m^{-2}}$ for LWU), resulting in a non-significant LWnet increasing trend. The increasing atmospheric temperature resulting from increasing greenhouse effect as well as the increasing summer cloud cover are both responsible for the LWD increase. On the contrary to the $\mathrm{MAR_{10km}}$ 1979–2014 trend, the 1960–2014 increasing cloud cover trend is not significant (Fig. 4.11, Table 4.8). However, as for the SMB, the significance of the summer cloud cover trend is debatable, given the very close values of the trend, its uncertainty range and the interannual variability of the summer cloud cover.

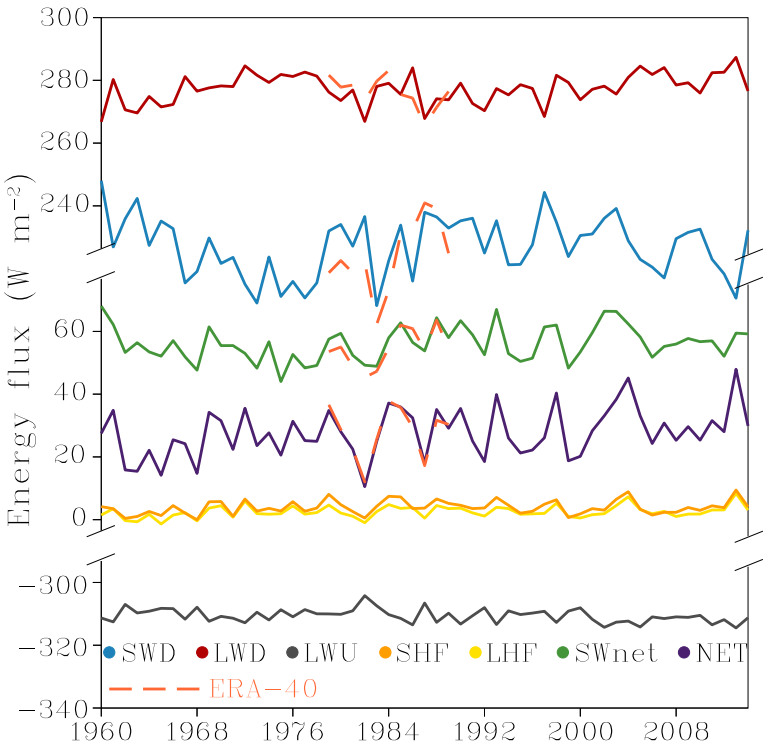

Figure 4.10: 1960–2014 evolution of the energy balance components ($\mathrm{W\,m^{-1}}$) averaged over the permanent ice area. The dashed curves represents the energy balance components simulated by MAR forced by ERA-40 over 1979–1989.

Over the ERA-40 era (1960–1978), the summer cloud cover and cloud optical depth increased significantly (+50 % of cloud cover and +28 % of cloud optical depth, Fig. 4.11), causing a marked significant decrease in SWD (-1.59 ± 0.55 $\mathrm{W\,m^{-2}\,yr^{-1}}$), increase in LWD ($+0.69 \pm 0.28\,\mathrm{W\,m^{-2}\,yr^{-1}}$) and LWnet ($+0.67 \pm 0.24$ $\mathrm{W\,m^{-2}\,yr^{-1}}$). The net energy available for the melt however did not increase

Table 4.8: 1960 – 2014 trends of the JJA energy balance components ($W\,m^{-2}\,yr^{-1}$), cloud cover (CC) and cloud optical depth (COD) (yr^{-1}) and their uncertainty range. The significant trends are in bold.

	Trend ($W\,m^{-2}\,yr^{-1}$)	Uncertainty range ($W\,m^{-2}\,yr^{-1}$)
NET	**0.165**	0.124
SWD	0.002	0.159
SWnet	0.066	0.091
LWD	**0.090**	0.076
LWU	**-0.045**	0.033
LWnet	0.045	0.064
SHF	0.028	0.035
LHF	**0.035**	0.031
	Trend (yr^{-1})	Uncertainty range (yr^{-1})
CC	0.0005	0.0007
COD	0.0006	0.0007

significantly during this period resulting in a non-significant melt trend. As a result of the increasing cloud cover, precipitation also increased significantly over 1960–1978 ($+0.72 \pm 0.36\,Gt\,yr^{-2}$). SMB therefore also increased significantly ($+0.63 \pm 59\,Gt\,yr^{-2}$) but the significance of the trend is less marked than for precipitation or the energy balance components. The ERA-40 summer near-surface temperature trend is, for its part, non-significant. Over the ERA-interim era (1979–2014) on the other hand, SMB has been stable, despite an increasing summer near-surface temperature ($+0.021 \pm 0.020\,°C\,yr^{-1}$). The ERA-40 reanalysis are known to overestimate the humidity compared to ERA-Interim (Dee et al., 2011) and the significant trends could be an artifact from ERA-40. However, despite differences in cloud cover (Fig. 4.11, dashed curves) and therefore in some energy balance components (LWD and LWnet, SWD but not SWnet) between MAR forced by ERA-Interim and MAR forced by ERA-40, the NET energy available in summer for the melt is the same with both sets of forcings (Fig. 4.10). As a consequence, the melt and runoff (Fig. 4.10, dashed curves) are also the same with MAR forced by ERA-Interim and ERA-40. Precipitation is a little overestimated (1979–1984) in MAR forced by ERA-40 compared to MAR forced by ERA-Interim, indicating that the overestimation of humidity in ERA-40 could induce a precipitation bias in MAR. SMB is however little impacted by the precipitation difference during the overlapping period and is the same for both

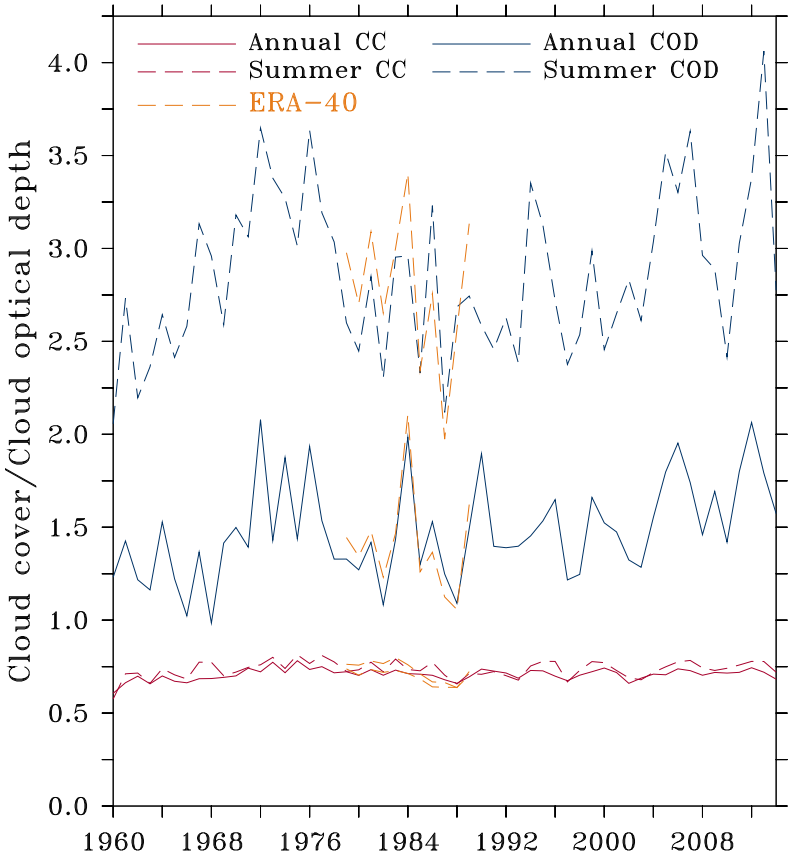

Figure 4.11: 1960 – 2014 evolution of annual (solid lines) and summer (dashed line) cloud cover (CC) and cloud optical depth (COD) averaged over the permanent ice area. The dashed curves represents the CC and COD simulated by MAR forced by ERA-40 over 1979–1989.

runs. The significant SMB increase over the 1960s–1970s is therefore probably not an artifact. A MAR simulation with other forcing fields (the NCEP reanalysis v1 for example) would however be useful to determine with certainty the reality of this significant trend.

As a consequence of the larger cloud cover over the ERA-40 era, precipitation was particularly high during the period 1972–1977 (Fig. 4.11), with 3 years (1972–1974–1976) significantly wetter than the 1960–2014 mean. This 6-year period is in the top 12 wettest years of the last 55 years and the 3 significantly wetter years are among the wettest 4. Among the significantly wetter years, 1972 also had significantly higher runoff and therefore an SMB very close to zero and below the trend. The years 1973, 1974, 1976 and 1977 had close to average or below average runoff and therefore relatively high SMB (9.8 $\mathrm{Gt\,yr^{-1}}$ for 1973 and 7.7 for the other three). In 1975 the amount of runoff was very small (only 16.6 $\mathrm{Gt\,yr^{-1}}$) and 1975 therefore holds the last 55 years's positive SMB record (15.6 $\mathrm{Gt\,yr^{-1}}$). With 1978 also having relatively high SMB, we have a period of 6 consecutive years

with SMB above the trend. The only longest period with above-the-trend SMB is 2005–2012, the 8-year period during which the summer atmospheric circulation changed (Fettweis et al. (2013b) and Chapter 2). But, again, precipitation might be overestimated in the ERA-40 period.

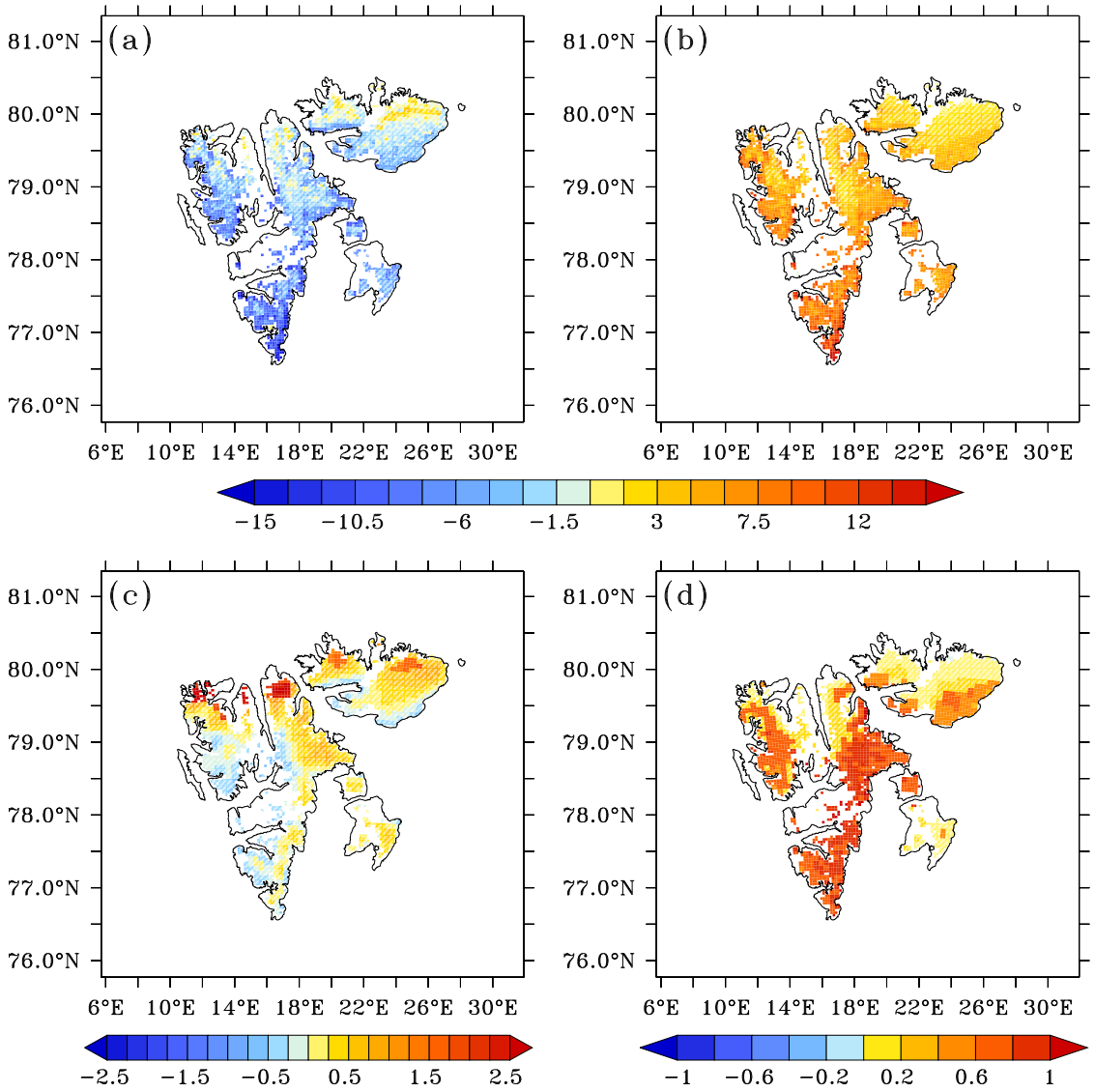

Figure 4.12: **(a)** 1960–2014 mean SMB trend (mm w.e. yr^{-2}) for $MAR_{3.75km}$. The non-hached areas correspond to the regions where the 1960–2014 SMB trend is not significant. **(b)** Same as **(a)** but for the melt. **(c)** Same as **(a)** but for snowfall. **(d)** Summer near-surface temperature change over 1960–2014 (°C/55 yr). For clarity, the temperature trend has been integrated over the 55-year period.

Over 1960–2014, melt has increased over all glaciated areas of Svalbard (Fig. 4.12b) and the trend is significant over all south Spitsbergen, most of north-western Spitsbergen and the south of northeastern Spitsbergen and Austfonna. Summer temperature also increased everywhere (Fig. 4.12d) and melt increased

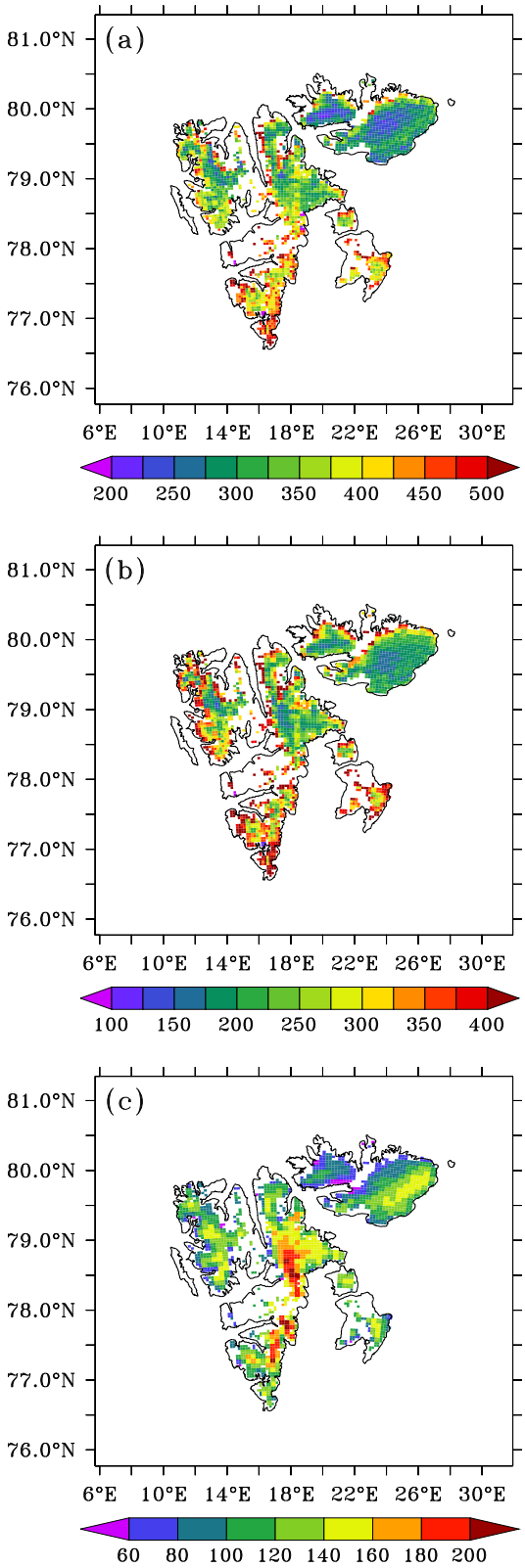

Figure 4.13: **(a)** 1960–2014 mean SMB standard deviation (mm w.e. yr^{-1}). **(b)** Same as **(a)** but for the melt. **(c)** Same as **(a)** but for snowfall.

significantly mostly where temperature did. In central regions of north Spitsbergen however, snowfall (Fig. 4.12c) increased enough to make the increasing melt non-significant by increasing the surface albedo despite a significantly increasing summer temperature. The snowfall trend is mostly not significant as part of snowfall has become rainfall as a result of rising temperature. On the west coast of Spitsbergen, snowfall decreased while melt increased and SMB therefore decreased significantly (Fig. 4.12a). In the south of northeastern Spitsbergen and Austfonna, however, melt increased significantly but snowfall increased too. As a result, SMB decreased but the trend is not significant. In south Spitsbergen, there are regions where melt increased so much that, even with increasing snowfall, SMB still decreased significantly. Finally, in the north of the ice caps, melt increased non-significantly whereas snowfall increased (even significantly in the very north). SMB therefore increased in the northern regions of the ice caps. The increasing trend is however significant for only one MAR pixel and, of the 30 663 km^2 covered with permanent ice, 10 575 km^2 have a significantly decreasing SMB trend.

The SMB interannual variability (represented by the mean annual standard deviation, Fig. 4.13a) is higher where the trend is the largest, i.e. mostly in south Spitsbergen and particularly in the ablation zone of south Spitsbergen (Fig. 4.8b). Melt also varies more from year to year (Fig. 4.13b) where the trend is the largest and much less where the melt is low, i.e. in the accumulation zone of Austfonna and northeastern Spitsbergen. Finally, snowfall is more constant from year to year than SMB (Fig. 4.13c).

4.5 Chapter conclusion

We implemented in MAR an online downscaling technique that allows the land module SISVAT to run at a resolution twice as high as the atmospheric module while only requiring 20 % additional computation time. We compared a simulation at a resolution of 7.5 km without downscaling to a simulation with downscaling (7.5 km resolution for the atmospheric variables and 3.75 km for the SISVAT variables). The use of the 7.5 km resolution improved a lot the agreement between MAR and near-surface temperature observations compared to the 10 km resolution simulations from Chapter 2.

On Spitsbergen, MAR compares better with accumulation measurements but a resolution of 3.75 km is still not enough to correctly represent the complexity of the topography while on Austfonna, a 7.5 km resolution is enough and the 3.75 km

resolution does not improve the results. Moreover, on Spitsbergen, the narrow ablation zones are much better resolved at 3.75 km than at 7.5 km. Given the small amount of additional computation time, we can conclude that our downscaling technique is an efficient tool for the simulation of SMB at very high resolution.

Over the last 55 years, the SMB, runoff/melt and sublimation trends were significant but the significance of the trends is debatable, given the large inter-annual variability of the variables and the very close values of the trends and their uncertainty range. SMB has mostly decreased significantly in south and west Spitsbergen whereas the increasing trends are not significant. Near-surface temperature has increased significantly, both on the annual and summer time scale.

CHAPTER 5

General conclusions and perspectives

The purpose of this thesis was to simulate the present and future climate and surface mass balance of Svalbard at high resolution with the regional climate model MAR. We implemented a subroutine allowing the surface module SISVAT to run at a resolution twice as high as the atmospheric module of MAR with only 20 % more computation time. In this subroutine, near-surface temperature and humidity are corrected from the atmospheric MAR lower resolution grid to the SISVAT higher resolution grid by extrapolating these fields to the elevation of the corresponding pixel in the high resolution grid, with the help of local temperature and humidity vertical gradients. Precipitation was however not corrected and will be the subject of future developments in MAR. We first ran MAR at a spatial resolution of 10 km over the ERA-Interim era (1979–2013) and afterwards, over the ERA-40 and ERA-Interim eras (1960–2014) with a simulation at 7.5 km and a simulation with the atmospheric module running at 7.5 km and SISVAT at 3.75 km. At 10 km, the topography is very smoothed: no elevation is above 1000 m whereas Spitsbergen peaks at ∼1700 m and elevations between 200 and 1000 m are mostly underestimated. This is problematic for SMB simulations because glaciers are generally found at high altitudes, where the topography is underestimated the most. At 7.5 km, the elevation biases are strongly reduced and the elevation distribution matches the actual distribution much closer than at 10 km. At 3.75 km, the biases are reduced furthermore. The SMB biases associated with the underestimation of elevation in the model (underestimation of orographic precipitation but also higher melt due to too low altitude) are therefore reduced in the 7.5 and 3.75 km topographies. The major topography improvements however come from the use of a 7.5 km resolution instead of 10 km rather than the use of the 3.75 km topography.

The first step of this work was to evaluate MAR over Svalbard by comparing its outputs to near-surface temperature and precipitation observations from weather stations and SMB measurements. The agreement between the daily observed and simulated temperature is very good at the annual time scale (R = 0.96, bias = −0.22 °C and RMSE = 2.6 °C at 7.5 km). As the melt is mainly driven by summer temperature, we also evaluated summer separately. The correlation between the observed and simulated temperature is however smaller (R = 0.82) if only summer is considered but biases and RMSE remain low (−0.4 and 1.8 °C). The cold bias present in the 10 km resolution run (−2.7 °C) is strongly reduced

in the 7.5 km resolution run, as a result of the much smaller elevation difference between the stations and their corresponding pixel in the 7.5 km topography and some minor improvements into MAR. Of the three stations with long temperature records, Ny-Ålesund and Svalbard Airport have a mean annual temperature cycle that matches the observed cycle almost perfectly with the 7.5 km topography. For precipitation, we have large biases and a poor correlation between the observed and simulated time series. The complex pattern of precipitation is not correctly represented in the 10 km grid, nor in the 7.5 km grid. Moreover, snowdrift can be important in Svalbard and is not simulated in our version of MAR. The misrepresentation of precipitation also partly comes from the fact that the resolution of the reanalysis used to force the boundaries of the domain is much larger than the MAR resolution. A solution to reduce the error would therefore be to run an intermediate MAR simulation with a lower resolution (e.g. 50 km) then force the higher resolution run with the outputs of the lower resolution run. Finally, the precipitation time series are shorter than for temperature and a lot of data are missing, making the evaluation even more difficult.

The SMB was then validated against local direct measurements or global observations deduced from satellite data and our results are in agreement with these observations. The comparison with local direct measurements showed that, on Austfonna, a resolution of 7.5 km is enough and the 3.75 km simulation does not improve the results. On Spitsbergen, the 7.5 and 3.75 km resolution simulations improved the results of the 10 km run but, even at 3.75 km, we were not able to represent the complex SMB spatial variability resulting from the very hilly topography that is not resolved at a resolution of 3.75 km and explains why large biases are still present. Higher resolution runs, e.g. 5 km MAR simulation with SMB corrected on a 2.5 km grid, are therefore necessary.

Over the ERA-Interim era (1979–2013), the simulated SMB is negative but stable and Svalbard glaciers are loosing mass through surface processes but without acceleration of the mass loss, on the contrary to the Greenland ice sheet. Over 1960–2014, the SMB is significantly decreasing but the significance of the trend is debatable. This stability of the SMB is in accordance with what has been observed on individual glaciers between the 1960s and the 1990s. Moreover, contrary to Greenland where melt records have regularly been broken since 2005, the SMB of Svalbard has been observed to remain stable in the last decade despite the warming observed in other Arctic regions (Serreze et al., 2009). This stability of the Svalbard SMB is due to a recent change in summer atmospheric circulation,

with anticyclonic conditions over Greenland and colder air masses coming from the north over Svalbard and opposing the observed Arctic warming. As a result, the Svalbard SMB was higher than average over 2006–2012. In 2013, the ERA-Interim atmospheric circulation was a south-southwesterly flow and could not oppose the Arctic warming anymore and the melt and near-surface summer temperature simulated by MAR were the highest of the last 55 years. In 2014, the atmospheric circulation was again coming from the northwest, damping the warming effect and SMB had an average value.

Then, with the perspective of making a future projection, we compared the MIROC5 global model outputs to ERA-Interim and MAR forced by MIROC5 to MAR forced by ERA-interim over 1980–2005. The significant temperature biases between MIROC5 and ERA-Interim were reduced in MAR forced by MIROC5 and no longer significant over the land. As a consequence, there was no significant difference in runoff, snowfall and SMB between MAR forced by ERA-Interim and by MIROC5 over 1980–2005. However, MIROC5 is not able to represent the recent change in the atmospheric circulation and MAR simulates a significant SMB decrease over 1980–2005, on the contrary to MAR forced by ERA-Interim. In the future, the MIROC5 temperature anomaly with respect to the historical mean closely follows the CMIP5 ensemble mean over Svalbard but becomes higher than the ensemble mean after 2060. In MAR, the surface temperature of the permanent ice area is limited to 0 °C, which is not the case in MIROC5, and the near-surface temperature increase in MAR is therefore limited compared to MIROC5. As a result, the projected MAR based near-surface temperature anomaly follows the CMIP5 ensemble mean better than MIROC5. Our choice of forcing MAR by MIROC5 is therefore representative of the CMIP5 ensemble mean.

In the future, MAR projects that the melt-albedo feedback associated with the expansion of the ablation/bare ice area will amplify the Arctic warming induced SMB decrease through an increase in net shortwave radiation absorbed by the surface, increasing the amount of energy available for the melt in summer. The net shortwave radiation is also the component of the energy balance the most sensitive to a rise in temperature and, while the solar radiation itself arriving at the surface is projected to decrease following an increase in cloudiness in summer, it will not be nearly enough to compensate the effect of the decreasing albedo on the melt. The accumulation zone is also projected to completely disappear by 2085, although it will happen much sooner in the south of the archipelago than in the north and the ice caps. MAR projects a contribution of 7.1 mm to the sea

level rise under the RCP8.5 scenario, coming from the Svalbard SMB changes over the 21st century.

In our simulations, we used a fixed ice mask and topography, which is acceptable over the present era but will be a source of error in future projections. Indeed, in the future, as the ice melts, the glaciers will thin and melt will increase furthermore, due to the rise in temperature associated with the lower altitude. By keeping the topography fixed, we therefore underestimate the increasing melt. On the other hand, under the Arctic warming, the glaciers are going to retreat and keeping a fixed ice mask will overestimate the melt, as the melt over these areas that are not supposed to be covered with permanent ice anymore will be huge in the future. We expect that those two opposing effects will partly compensate each other and that the error on the simulated SMB will be relatively small but only a simulation in which the ice mask and topography are updated could confirm this. To do so, we could couple MAR to a dynamical ice sheet model. Not only we could model the future SMB of Svalbard more realistically but it would also allow us to model the dynamics of the Svalbard glaciers and ice caps with a more accurate SMB as input, as ice sheet models are usually forced with SMB coming from empirical models.

Finally, over the present era, we forced MAR with the ERA reanalysis and it would be interesting to compare the results to MAR forced by other reanalysis, for example the NCEP reanalysis v1 from NCAR. Moreover, we only covered the last 55 years but two reanalysis covering the whole 20th century are now available: ERA-20C from ECMWF and 20CRv2c from NCAR. Knowing that the Svalbard glaciers were still close to their Little Ice Age maximum at the beginning of the 20th century (Lefauconnier and Hagen, 1990), a global view of the 20th century climate of Svalbard would be very useful.

References

Anisimov, O. A., Vaughan, D. G., Callaghan, T. V., Furgal, C., Marchant, H., Prowse, T. D., Vilhjálmsson, H., Walsh, J. E., Parry, M. L., Canziani, O. F., Palutikof, J. P., van der Linden, P. J., and Hanson, C. E.: Polar Regions (Arctic and Antarctic), Climate Change 2007: Impacts, Adaptation and Vulnerability. Contribution of Working Group II to the Fourth Assessment Report of the Intergovernmental Panel on Climate Change, Cambridge University Press, Cambridge, pp. 653–685, 2007.

Bamber, J. L., Krabill, W., Raper, V., and Dowdeswell, J. A.: Anomalous recent growth of part of a large Arctic ice cap: Austfonna, Svalbard, Geophysical Research Letters, 31, L12 402, doi: 10.1029/2004GL019667, 2004.

Bamber, J. L., Krabill, W., Raper, V., Dowdeswell, J. A., and Oerlemans, J.: Elevation changes measured on Svalbard glaciers and ice caps from airborne laser data, Annals of Glaciology, 42, 202–208, 2005.

Belleflamme, A., Fettweis, X., Lang, C., and Erpicum, M.: Current and future atmospheric circulation at 500 hPa over Greenland simulated by the CMIP3 and CMIP5 global models, Climate Dynamics, 41, 2061–2080, doi: 10.1007/s00382-012-1538-2, 2013.

Benestad, R. E., Førland, E. J., and Hanssen-Bauer, I.: Empirically downscaled temperature scenarios for Svalbard, Atmospheric Science Letters, 3, 71–93, doi: 10.1006/asle.2002.0051, 2002.

Błaszczyk, M., Jania, J. A., and O., H. J.: Tidewater glaciers of Svalbard: Recent changes and estimates of calving fluxes, Polish Polar Research, 30, 85–142, 2009.

Brun, E.: Investigation on wet-snow metamorphism in respect of liquid-water content, Annals of Glaciology, 13, 22–26, 1989.

Claremar, B., Obleitner, F., Reijmer, C., Pohjola, V., Waxegard, A., Karner, F., and Rutgersson, A.: Applying a Mesoscale Atmospheric Model to Svalbard Glaciers, Advances in Meteorology, 2012, 321 649, doi: 10.1155/2012/321649, 2012.

Day, J. J., Bamber, J. L., Valdes, P. J., and Kohler, J.: The impact of a seasonally ice free Arctic Ocean on the temperature, precipitation and surface mass balance of Svalbard, The Cryosphere, 6, 35–50, doi: 10.5194/tc-6-35-2012, 2012.

de Ridder, K. and Gallée, H.: Land surface–induced regional climate change in Southern Israel, Journal of Applied Meteorology, 37, 1470–1485, 1998.

de Woul, M. and Hock, R.: Static mass-balance sensitivity of Arctic glaciers and ice caps using a degree-day approach, Annals of Glaciology, 42, 217–224, 2005.

Dee, D. P., Uppala, S. M., Simmons, A. J., Berrisford, P., Poli, P., Kobayashi, S., Andrae, U., Balmaseda, M. A., Balsamo, G., Bauer, P., Bechtold, P., Beljaars, A. C. M., van de Berg, L., Bidlot, J., Bormann, N., Delsol, C., Dragani, R., Fuentes, M., Geer, A. J., Haimberger, L., Healy, S. B., Hersbach, H., Hólm, E. V., Isaksen, L., Kållberg, P., Köhler, M., Matricardi, M., McNally, A. P., Monge-Sanz, B. M., Morcrette, J.-J., Park, B.-K., Peubey, C., de Rosnay, P., Tavolato, C., Thépaut, J.-N., and Vitart, F.: The ERA-Interim reanalysis: configuration and performance of the data assimilation system, Quarterly Journal of the Royal Meteorological Society, 137, 553–597, doi: 10.1002/qj.828, 2011.

Dowdeswell, J. A.: Drainage-basin characteristics of Nordaustlandet ice caps, Svalbard, Journal of Glaciology, 32, 31–38, 1986.

Dowdeswell, J. A., Benham, T. J., Strozzi, T., and Hagen, J. O.: Iceberg calving flux and mass balance of the Austfonna ice cap on Nordaustlandet, Svalbard, Journal of Geophysical Research: Earth Surface, 113, F03 022, doi: 10.1029/2007JF000905, 2008.

Etzelmüller, B., Schuler, T. V., Isaksen, K., Christiansen, H. H., Farbrot, H., and Benestad, R.: Modeling the temperature evolution of Svalbard permafrost during the 20th and 21st century, The Cryosphere, 5, 67–79, doi: 10.5194/tc-5-67-2011, 2011.

Fettweis, X., Franco, B., Tedesco, M., van Angelen, J. H., Lenaerts, J. T. M., van den Broeke, M. R., and Gallée, H.: Estimating the Greenland ice sheet surface mass balance contribution to future sea level rise using the regional

atmospheric climate model MAR, The Cryosphere, 7, 469–489, doi: 10.5194/tc-7-469-2013, 2013a.

Fettweis, X., Hanna, E., Lang, C., Belleflamme, A., Erpicum, M., and Gallée, H.: Brief communication "Important role of the mid-tropospheric atmospheric circulation in the recent surface melt increase over the Greenland ice sheet", The Cryosphere, 7, 241–248, doi: 10.5194/tc-7-241-2013, 2013b.

Førland, E. J., Benestad, R. E., Flatøy, F., Hanssen-Bauer, I., Haugen, J. E., Isaksen, K., Sorteberg, A., and Ådlandsvik, B.: Climate development in North Norway and the Svalbard region during 1900–2100, Norwegian Polar Institute Report 128, Tromsø, Norway, 2009.

Førland, E. J., Benestad, R., Hanssen-Bauer, I., Haugen, J. E., and Skaugen, T. E.: Temperature and precipitation development at Svalbard 1900–2100, Advances in Meteorology, 2011, 893 790, doi: 10.1155/2011/893790, 2011.

Fowler, A. C., Murray, T., and Ng, F. S. L.: Thermally controlled glacier surging, Journal of Glaciology, 47, 527–538, 2001.

Franco, B., Fettweis, X., Lang, C., and Erpicum, M.: Impact of spatial resolution on the modelling of the Greenland ice sheet surface mass balance between 1990–2010, using the regional climate model MAR, The Cryosphere, 6, 695–711, doi: 10.5194/tc-6-695-2012, 2012.

Franco, B., Fettweis, X., and Erpicum, M.: Future projections of the Greenland ice sheet energy balance driving the surface melt, The Cryosphere, 7, 1–18, doi: 10.5194/tc-7-1-2013, 2013.

Gallée, H. and Schayes, G.: Development of a three-dimensional meso-γ primitive equation model: katabatic winds simulation in the area of Terra Nova Bay, Antarctica, Monthly Weather Review, 122, 671–685, 1994.

Gallée, H., Guyomarc'h, G., and Brun, E.: Impact of snow drift on the Antarctic ice sheet surface mass balance: possible sensitivity to snow-surface properties, Boundary-Layer Meteorology, 99, 1–19, doi: 10.1023/A:1018776422809, 2001.

Gallée, H., Trouvilliez, A., Agosta, C., Genthon, C., Favier, V., and Naaim-Bouvet, F.: Transport of snow by the wind: a comparison between observations in Adélie Land, Antarctica, and simulations made with the regional climate model MAR, Boundary-Layer Meteorology, 146, 133–147, doi: 10.1007/s10546-012-9764-z, 2013.

Gardner, A. S., Moholdt, G., Cogley, J. G., Wouters, B., Arendt, A. A., Wahr, J., Berthier, E., Hock, R., Pfeffer, W. T., Kaser, G., Ligtenberg, S. R. M., Bolch, T., Sharp, M. J., Hagen, J. O., van den Broeke, M. R., and Paul, F.: A reconciled estimate of glacier contributions to sea level rise: 2003 to 2009, Science, 340, 852–857, doi: 10.1126/science.1234532, 2013.

Giorgi, F., Francisco, R., and Pal, J.: Effects of a Subgrid-Scale Topography and Land Use Scheme on the Simulation of Surface Climate and Hydrology. Part I: Effects of Temperature and Water Vapor Disaggregation, Journal of Hydrometeorology, 4, 317–333, doi: 10.1175/1525-7541(2003)4<317:EOASTA>2.0.CO;2, 2003.

Goelzer, H., Huybrechts, P., Fürst, J. J., Nick, F. M., Andersen, M. L., Edwards, T. L., Fettweis, X., Payne, A. J., and Shannon, S.: Sensitivity of Greenland ice sheet projections to model formulations, Journal of Glaciology, 59, 733–749, doi: 10.3189/2013JoG12J182, 2013.

Hagen, J. O., Liestøl, O., Roland, E., and Jørgensen., T.: Glacier Atlas of Svalbard and Jan Mayen, Norwegian Polar Institue, Oslo, 1993.

Hagen, J. O., Kohler, J., Melvold, K., and Winther, J.-G.: Glaciers in Svalbard: mass balance, runoff and freshwater flux, Polar Research, 22, 145–159, 2003a.

Hagen, J. O., Melvold, K., Pinglot, F., and Dowdeswell, J. A.: On the Net Mass Balance of the Glaciers and Ice Caps in Svalbard, Norwegian Arctic, Arctic, Antarctic, and Alpine Research, 35, 264–270, doi: 10.1657/1523-0430(2003)035[0264:OTNMBO]2.0.CO;2, 2003b.

Hisdal, V.: Geography of Svalbard, 1 Edn., Norwegian Polar Research Institute, Oslo, Norway, 1976.

Isaksen, K., Benestad, R. E., Harris, C., and Sollid, J. L.: Recent extreme near-surface permafrost temperatures on Svalbard in relation to future climate scenarios, Geophysical Research Letters, 34, L17 502, doi: 10.1029/2007GL031002, 2007.

Jiskoot, H., Murray, T., and Boyle, P.: Controls on the distribution of surge-type glaciers in Svalbard, Journal of Glaciology, 46, 412–422, 2000.

Kamb, B., Raymond, C. F., Harrison, W. D., Engelhardt, H., Echelmeyer, K. A., Humphrey, N., Brugman, M. M., and Pfeffer, T.: Glacier surge mechanism: 1982–1983 surge of Variegated Glacier, Alaska, Science, 227, 469–479, 1985.

Kaser, G., Cogley, J. G., Dyurgerov, M. B., Meier, M. F., and Ohmura, A.: Mass balance of glaciers and ice caps: Consensus estimates for 1961–2004, Geophysical Research Letters, 33, L19 501, doi: 10.1029/2006GL027511, 2006.

Lang, C., Fettweis, X., and Erpicum, M.: Stable climate and surface mass balance in Svalbard over 1979–2013 despite the Arctic warming, The Cryosphere, 9, 83–101, doi: 10.5194/tc-9-83-2015, 2015a.

Lang, C., Fettweis, X., and Erpicum, M.: Future climate and surface mass balance of Svalbard glaciers in an RCP8.5 climate scenario: a study with the regional climate model MAR forced by MIROC5, The Cryosphere, 9, 945–956, doi: 10.5194/tc-9-945-2015, 2015b.

Lefauconnier, B. and Hagen, J. O.: Statistical Analysys and reconstruction of the Brøggerbreen mass-balance for the last 77 years, Annals of Glaciology, 14, 148–152, 1990.

Lefauconnier, B. and Hagen, J. O.: Surging and calving glaciers in eastern Svalbard, Norsk Polaarintitutt Meddelelser, 116, 130pp, 1991.

Lenaerts, J. T. M., van Angelen, J. H., van den Broeke, M. R., Gardner, A. S., Wouters, B., and van Meijgaard, E.: Irreversible mass loss of Canadian Arctic Archipelago glaciers, Geophysical Research Letters, 40, 870–874, doi: 10.1002/grl.50214, 2013.

Liestøl, O.: Glaciers of Svalbard, Norway, US Geological Survey Professional Paper, 1386, E127–E151, 1993.

Marzeion, B., Jarosch, A. H., and Hofer, M.: Past and future sea-level change from the surface mass balance of glaciers, The Cryosphere, 6, 1295–1322, doi: 10.5194/tc-6-1295-2012, 2012.

Meehl, G. A., Stocker, T. F., Collins, W. D., Friedlingstein, P., Gaye, A. T., Gregory, J. M., Kitoh, A., Knutti, R., Murphy, J. M., Noda, A., Raper, S. C. B., Watterson, I. G., Weaver, A. J., and Zhao, Z.-C.: Global climate projections, in: Climate Change 2007: The Physical Science Basis. Contribution of Working Group I to the Fourth Assessment Report of the Intergovernmental Panel on Climate Change, edited by: Solomon, S., Qin, D., Manning, M., Chen, Z., Marquis, M., Averyt, K. B., Tignor, M., and Miller, H. L., Cambridge University Press, Cambridge, UK and New York, NY, USA, 2007.

Meier, M. F., Dyurgerov, M. B., Rick, U. K., O'Neel, S., Pfeffer, W. T., Anderson, R. S., Anderson, S. P., and Glazovsky, A. F.: Glaciers dominate eustatic sea-level rise in the 21st century, Science, 317, 1064–1067, doi: 10.1126/science.1143906, 2007.

Moholdt, G., Nuth, C., Hagen, J. O., and Kohler, J.: Recent elevation changes of Svalbard glaciers derived from ICESat laser altimetry, Remote Sensing of Environment, 114, 2756–2767, doi: 10.1016/j.rse.2010.06.008, 2010.

Moss, R. H., Edmonds, J. A., Hibbard, K. A., Manning, M. R., Rose, S. K., van Vuuren, D. P., Carter, T. R., Emori, S., Kainuma, M., Kram, T., Meehl, G. A., Mitchell, J. F. B., Nakicenovic, N., Riahi, K., Smith, S. J., Stouffer, R. J., Thomson, A. M., Weyant, J. P., and Wilbanks, T. J.: The next generation of scenarios for climate change research and assessment, Nature, 463, 747–756, doi: 10.1038/nature08823, 2010.

Murray, T., Strozzi, T., Luckman, A., Jiskoot, H., and Christakos, P.: Is there a single surge mechanism? Contrasts in dynamics between glacier surges in Svalbard and other regions, Journal of Geophysical Research: Solid Earth, 108, B5, doi: 10.1029/2002JB001906, 2003.

Mémin, A., Rogister, Y., Hinderer, J., Omang, O. C., and Luck, B.: Secular gravity variation at Svalbard (Norway) from ground observations and GRACE satellite data, Geophysical Journal International, 184, 1119–1130, doi: 10.1111/j.1365-246X.2010.04922.x, 2011.

Noël, B., Fettweis, X., van de Berg, W. J., van den Broeke, M. R., and Erpicum, M.: Sensitivity of Greenland Ice Sheet surface mass balance to perturbations in sea surface temperature and sea ice cover: a study with the regional climate model MAR, The Cryosphere, 8, 1871–1883, doi: 10.5194/tc-8-1871-2014, 2014.

Nuth, C., Moholdt, G., Kohler, J., Hagen, J. O., and Kääb, A.: Svalbard glacier elevation changes and contribution to sea level rise, Journal of Geophysical Research: Earth Surface, 115, F01 008, doi: 10.1029/2008JF001223, 2010.

Nuth, C., Schuler, T. V., Kohler, J., Altena, B., and Hagen, J. O.: Estimating the long-term calving flux of Kronebreen, Svalbard, from geodetic elevation changes and mass-balance modelling, Journal of Glaciology, 58, 119–133, doi: 10.3189/2012JoG11J036, 2012.

Nuth, C., Kohler, J., König, M., von Deschwanden, A., Hagen, J. O., Kääb, A., Moholdt, G., and Pettersson, R.: Decadal changes from a multi-temporal glacier inventory of Svalbard, The Cryosphere, 7, 1603–1621, doi: 10.5194/tc-7-1603-2013, 2013.

Pinglot, J. F., Pourchet, M., Lefauconnier, B., Hagen, J. O., Isaksson, E., Vaikmäe, R., and Kamiyama, K.: Accumulation in Svalbard glaciers deduced from ice cores with nuclear tests and Chernobyl reference layers, Polar Research, 18, 315–321, 1999.

Pinglot, J. F., Hagen, J. O., Melvold, K., Eiken, T., and Vincent, C.: A mean net accumulation pattern derived from radioactive layers and radar soundings on Austfonna, Nordaustlandet, Svalbard, Journal of Glaciology, 47, 555–566, 2001.

Radić, V. and Hock, R.: Regionally differentiated contribution of mountain glaciers and ice caps to future sea-level rise, Nature Geoscience, 4, 91–94, doi: 10.1038/ngeo1052, 2011.

Radić, V., Bliss, A., Beedlow, A. C., Hock, R., Miles, E., and Cogley, J. G.: Regional and global projections of twenty-first century glacier mass changes in response to climate scenarios from global climate models, Climate Dynamics, 42, 37–58, doi: 10.1007/s00382-013-1719-7, 2014.

Rasmussen, L. A. and Kohler, J.: Mass balance of three Svalbard glaciers reconstructed back to 1948, Polar Research, 26, 168–174, doi: 10.1111/j.1751-8369.2007.00023.x, 2007.

Rignot, E., Velicogna, I., van den Broeke, M. R., Monaghan, A., and Lenaerts, J. T. M.: Acceleration of the contribution of the Greenland and Antarctic ice sheets to sea level rise, Geophysical Research Letters, 38, L05 503, doi: 10.1029/2011GL046583, 2011.

Rignot, E., Mouginot, J., Morlighem, M., Seroussi, H., and Scheuchl, B.: Widespread, rapid grounding line retreat of Pine Island, Thwaites, Smith, and Kohler glaciers, West Antarctica, from 1992 to 2011, Geophysical Research Letters, 41, 3502–3509, doi: 10.1002/2014GL060140, 2014.

Rogelj, J., Meinshausen, M., and Knutti, R.: Global warming under old and new scenarios using IPCC climate sensitivity range estimates, Nature Climate Change, 2, 248–253, doi: 10.1038/nclimate1385, 2012.

Rye, C. J., Arnold, N. S., Willis, I. C., and Kohler, J.: Modeling the surface mass balance of a high Arctic glacier using the ERA-40 reanalysis, Journal of Geophysical Research: Earth Surface, 115, F02 014, doi: 10.1029/2009JF001364, 2010.

Rye, C. J., Willis, I. C., Arnold, N. S., and Kohler, J.: On the need for automated multiobjective optimization and uncertainty estimation of glacier mass balance models, Journal of Geophysical Research: Earth Surface, 117, F02 005, doi: 10.1029/2011JF002184, 2012.

Sakamoto, T. T., Komuro, Y., Nishimura, T., Ishii, M., Tatebe, H., Shiogama, H., Hasegawa, A., Toyoda, T., Mori, M., Suzuki, T., Imada, Y., Nozawa, T., Takata, K., Mochizuki, T., Ogochi, K., Emori, S., Hasumi, H., and Kimoto, M.: MIROC4h– A New High-Resolution Atmosphere-Ocean Coupled General Circulation Model, Journal of the Meteorological Society of Japan. Ser. II, 90, 325–359, doi: 10.2151/jmsj.2012-301, 2012.

Schuler, T. V., Loe, E., Taurisano, A., Eiken, T., Hagen, J. O., and Kohler, J.: Calibrating a surface mass-balance model for Austfonna ice cap, Svalbard, Annals of Glaciology, 46, 241–248, doi: doi:10.3189/172756407782871783, 2007.

Serreze, M. C., Barrett, A. P., Stroeve, J. C., Kindig, D. N., and Holland, M. M.: The emergence of surface-based Arctic amplification, The Cryosphere, 3, 11–19, doi: 10.5194/tc-3-11-2009, 2009.

Shepherd, A., Ivins, E. R., A, G., Barletta, V. R., Bentley, M. J., Bettadpur, S., Briggs, K. H., Bromwich, D. H., Forsberg, R., Galin, N., Horwath, M., Jacobs, S., Joughin, I., King, M. A., Lenaerts, J. T. M., Li, J., Ligtenberg, S. R. M., Luckman, A., Luthcke, S. B., McMillan, M., Meister, R., Milne, G., Mouginot, J., Muir, A., Nicolas, J. P., Paden, J., Payne, A. J., Pritchard, H., Rignot, E., Rott, H., Sørensen, L. S., Scambos, T. A., Scheuchl, B., Schrama, E. J. O., Smith, B., Sundal, A. V., van Angelen, J. H., van de Berg, W. J., van den Broeke, M. R., Vaughan, D. G., Velicogna, I., Wahr, J., Whitehouse, P. L., Wingham, D. J., Y. D., Young, D., and Zwally, H. J.: A reconciled estimate of of ice-sheet mass balance, Science, 338, 1183–1189, doi: 10.1126/science.1228102, 2012.

Snedecor, G. W. and Cochran, W. G.: Statistical methods, The Iowa State University Press, Ames, USA, 1971.

van Angelen, J. H., Lenaerts, J. T. M., van den Broeke, M. R., Fettweis, X., and van Meijgaard, E.: Rapid loss of firn pore space accelerates 21st century Greenland mass loss, Geophysical Research Letters, 40, 1–5, doi: 10.1002/grl.50490, 2013.

van Pelt, W. J. J., Oerlemans, J., Reijmer, C. H., Pohjola, V. A., Pettersson, R., and van Angelen, J. H.: Simulating melt, runoff and refreezing on Nordenskiöldbreen, Svalbard, using a coupled snow and energy balance model, The Cryosphere, 6, 641–659, doi: 10.5194/tc-6-641-2012, 2012.

Watanabe, M., Suzuki, T., O'ishi, R., Komuro, Y., Watanabe, S., Emori, S., Takemura, T., Chikira, M., Ogura, T., Sekiguchi, M., Takata, K., Yamazaki, D., Yokohata, T., Nozawa, T., Hasumi, H., Tatebe, H., and Kimoto, M.: Improved climate simulation by MIROC5: mean states, variability, and climate sensitivity, Journal of Climate, 23, 6312–6335, 2010.

Wilson, A. B., Bromwich, D. H., and Hines, K. M.: Evaluation of Polar WRF forecasts on the Arctic System Reanalysis domain: Surface and upper air analysis, Journal of Geophysical Research, 116, D11 112, doi: 10.1029/2010JD015013, 2011.

Winther, J.-G., Bruland, O., Sand, K., Killingtveit, Å., and Marechal, D.: Snow accumulation distribution on Spitsbergen, Svalbard, in 1997, Polar Research, 17, 155–164, 1998.

Wouters, B., Chambers, D., and Schrama, E. J. O.: GRACE observes small-scale mass loss in Greenland, Geophysical Research Letters, 35, L20 501, doi: 10.1029/2008GL034816, 2008.

Zuo, Z. and Oerlemans, J.: Modelling albedo and specific balance of the Greenland ice sheet: calculations for the Søndre Strømfjord transect, Journal of Glaciology, 42, 305–317, 1996.